Aerodynamic Design and Wind Tunnel Tests of Novel Blade Shapes for the Savonius Wind Rotor

A Thesis Submitted in Partial Fulfillment of the Requirements
for the Award of the Degree of

Doctor of Philosophy

by

Man Mohan

Regn No. 186103021

Department of Mechanical Engineering
Indian Institute of Technology Guwahati
Guwahati -781039, Assam, India
December, 2024

Declaration

I hereby certify that the work compiled in this dissertation entitled '**Aerodynamic Design and Wind Tunnel Tests of Novel Blade Shapes for Savonius Wind Rotor**' is the outcome of my research work under the guidance of Professor Ujjwal K. Saha in the Department of Mechanical Engineering, Indian Institute of Technology Guwahati, India. The present work has not earlier been submitted for the award of any degree, diploma, associateship, fellowship or its equivalent to any University or Institution.

Date: December 30, 2024

(Man Mohan)
Registration No. 186103021
Department of Mechanical Engineering
Indian Institute of Technology Guwahati

Department of Mechanical Engineering
Indian Institute of Technology Guwahati
Guwahati-781039, India

Certificate

It is certified that the work contained in the thesis entitled '**Aerodynamic Design and Wind Tunnel Tests of Novel Blade Shapes for Savonius Wind Rotor**' submitted by Man Mohan to the Indian Institute of Technology Guwahati for the award of the Doctor of Philosophy has been conducted under my supervision in the Department of Mechanical Engineering, Indian Institute of Technology Guwahati. This work has not been submitted elsewhere for the award of any degree.

Date: December 30, 2024

(Ujjwal K. Saha)
Professor
Department of Mechanical Engineering
Indian Institute of Technology Guwahati
Guwahati-781039, India

Acknowledgement

I extend my deepest gratitude to Prof. U. K. Saha, whose invaluable guidance has been instrumental in bringing this project to fruition. His unwavering support, encouragement, and insightful direction have served as the driving force behind my endeavors. His dedication to his students and profound understanding of the subject matter place him in a league of exceptional mentors.

I am also indebted to my doctoral committee members, Dr. Amaresh Dalal, Dr. Dipankar N. Basu, and Dr. Mihir K. Purkait, for their invaluable suggestions and guidance throughout my research. I extend my sincere appreciation to Prof. K. S. R. K. Murthy (HOD, Department of Mechanical Engineering), for extending the research facilities. Thanks, are also due to Dr. Deepak Sharma for his technical advice. The financial support from MHRD, New Delhi is gratefully extended.

I am grateful to the faculty members, staff, and research scholars of IIT Guwahati for their wholehearted cooperation and support. Special thanks to the senior technicians, Mr. Manoj K. Baishya, for his assistance in the fabrication of wind turbine blades.

I also express my gratitude to my friend, Mr. Divyesh K. Kansagara and colleagues for their valuable support in early phase of my research. Acknowledgment would be incomplete without recognizing the contributions of authors whose works have laid the foundation for my research.

Finally, I express profound gratitude to my beloved parents, wife, siblings, and extended family for their unwavering encouragement and blessings throughout my journey.

Man Mohan

Abstract

Wind turbines are increasingly used worldwide to generate electricity without contributing to global warming. The Savonius wind rotor is widely known for small-scale power generation devices. However, the Savonius rotor, a simple type of vertical-axis wind turbine, suffers from low efficiency due to a high negative torque from the returning blade. To address this issue, extensive researches have been done on enhancing various design parameters, geometric parameters, implementing augmentation technique and other aspects. However, there is always scope for further investigation to contribute better. In view of this, the present study aims at generating blade profile through optimization techniques (OTs). The optimal blade profile is developed considering the power coefficient as an output function using the optimization techniques, viz., simplex search method (SSM), non-dominated sorting genetic algorithm-II (NSGA-II). Moreover, a novel parabolic blade profile is developed analytically considering the sectional cut angle (θ) of the parabola as a design parameter.

The flow physics of both the developed blade profiles are then studied using ANSYS Fluent software with shear-stress transport (SST) k-ω turbulence model. The solver setup employs the finite volume method to simulate the transient 2D flow around the blade profile. A direct comparison is made between the developed blade profiles and the conventional semicircular profile over a range of tip speed ratios (*TSR*s). The effects of *TSR* and Reynolds numbers (*Re*) on the performance are also investigated. The blade profile developed through OTs has showcased maximum performance coefficient (C_{Pmax}) of 0.283 at a *TSR* of 0.8. While the parabolic blade profile generated at θ = 32.5° has showcased the highest C_{pmax} amongst all the blade profiles generated at various θ values. The C_{Pmax} obtained from the parabolic profile is 0.319 against the semicircular counterpart with a C_{Pmax} of 0.266. Thereby it can be seen that the parabolic profile has shown an improved C_{Pmax} by 20% over the semicircular counterpart. The lift and drag analysis of the parabolic profile reveals an improvement of maximum drag coefficient (C_{Dmax}) by 18.18% over its semicircular counterpart. The best performance of the parabolic profile is obtained at *TSR* of 0.8 and at *Re* of 0.97×10^5. Moreover, the parabolic profile has showcased the better performance against the blade profile designed through OTs by 13%. Finally, the wind tunnel tests are performed to check the practical feasibility of the parabolic bladed rotor where it shows C_{Pmax} of 0.165 against C_{Pmax} of 0.138 for the semicircular-bladed rotor.

Contents

3 Creation of a Novel Spline Profile by Optimization and Computational Study 29-50

4 Creation of a Parabolic Blade Profile and Computational Study 51-63

Nomenclature

English Symbols

A	Swept area	[m^2]
AR	Aspect ratio	--
C_D	Drag coefficient	--
C_L	Lift coefficient	--
C_P	Power coefficient	--
C_T	Torque coefficient	--
D	Diameter of the rotor	[mm]
e	Overlap distance	[mm]
F_L	Lift force	[N]
F_D	Drag force	[N]
H	Rotor height	[mm]
L	Chord length of the blade profile	[mm]
N	Rotational speed of a rotor	[rpm]
OR	Overlap ratio	--
$P_{available}$	Available wind power	W
P_{rotor}	Rotor shaft power	W
SG	Separation gap	[mm]
TSR	Tip speed ratio	--
t	Rotor thickness	[mm]
u	Rotor speed	[m/s]
V	Free stream wind speed	[m/s]

Greek symbols

ρ	Density of air	[kg/m^3]
α	Angle of attack	[degree]
k	Turbulent kinetic energy	[m^2/s^2]
ε	Turbulence dissipation rate	[m^2/s^3]
ω	Rotational speed of rotor	[rad/s]

Abbreviations

ANN	Artificial Neural Network
CFD	Computational Fluid Dynamics
CST	Class Shape Transfer
DCT	Discrete Cosine Transformation
DVM	Discrete Vortex Method
EA	Evolutionary Algorithm
FVM	Finite Volume Method
GA	Genetic Algorithm
HAWT	Horizontal Axis Wind Turbine
RANS	Reynolds-averaged Navier-Stokes
RPM	Revolution per Minute
SSA	Salp Swarm Algorithm
SST	Shear Stress Transport
SSM	Simplex Search Method
NSGA	Non-dominated Sorting Genetic Algorithm
OT	Optimization Technique
PSO	Particle Swarm Optimization
VAWT	Vertical Axis Wind Turbine

List of Figures

List of Tables

Chapter 1

Introduction

Chapter Outline

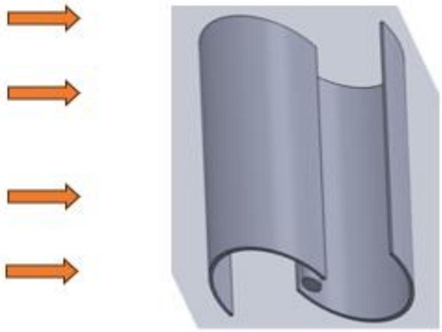

1.1 Present Energy Scenario in India

The renewable energy sources offer a sustainable alternative to finite fossil fuels like coal, oil, and natural gas, which contribute to climate change and environmental degradation. The introduction of renewable energy technologies represents a paradigm shift in the way we produce and consume energy, offering numerous benefits for society, the economy, and the environment.

The global demand for electricity is anticipated to triple by 2050, with fossil fuels projected to constitute no more than 60% of the total energy consumed, a decrease from the current 80%. Conventional fossil resources like oil, natural gas, and coal, being non-renewable, contribute significantly to atmospheric pollution (Amano, 2017; Prabhukhot and Prabhukhot, 2017). Wind energy technology emerges as a crucial player in providing environmentally friendly energy for both domestic and industrial applications (Wong et al., 2017; Damak et al., 2018). Wind energy accounts for nearly 4% of global electricity supply and has become the fastest-growing source of renewables worldwide. As of the end of 2018, approximately 597 GW of wind power was operational globally (GWEC, 2019).

The power generated is a key metric for a country's economic standing. According to the Central Electricity Authority (CEA) of India's report as of December 2018, India had an installed power generation capacity of 349,288 MW, with 74,081 MW being renewable energy-based power. Notably, 5.6 GW of wind energy was added in the 2016-2017 period, and India's projected energy demand by 2022 is estimated to be 175 GW. Wind energy is the world's fastest-growing energy technology, with a growth rate nearly 200 times that of other sources. While it currently constitutes a small percentage of the overall energy mix, its rapid growth suggests it will play a significant role in the future energy landscape.

Over the past few decades, substantial research has been conducted on harnessing wind power using turbines. Of all renewable energy sources, approximately 47% of power is derived from wind (Raimi et al., 2024). Figure 1.1 illustrates the contribution of energy from various renewable sources.

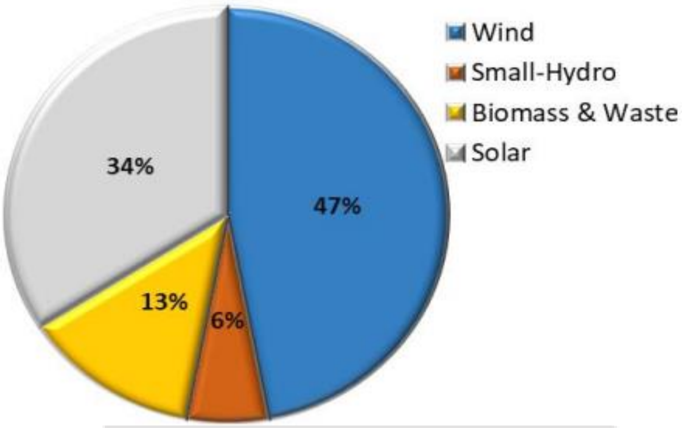

Figure 1.1: Contribution of energy from various renewable sources

1.2 Motivation

The necessity for energy has been a fundamental aspect of human civilization throughout history. Currently, the predominant means of meeting energy demands involves the combustion of fossil fuels. However, it has become evident in recent times that the utilization of non-renewable energy sources has severe environmental consequences. Fossil fuels, extensively employed for power generation and transportation, contribute significantly to elevated levels of harmful gases in the environment. These resources, formed over millions of years, are not only finite but also lead to detrimental effects such as global warming, pollution, and health issues.

Aside from the environmental impact, fossil fuel and coal reserves are limited. According to the CIA World Factbook, at the current consumption rate, it is projected that existing fossil fuel reserves could be entirely depleted within the next eighty to ninety years. Furthermore, the coal quality in India is generally subpar, with only certain regions in Assam possessing better-quality coal with 50 to 55% ash content. The high ash content in coal results in a lower calorific value, leading to increased atmospheric pollution. Despite these challenges, an immediate cessation of dependence on fossil fuels is impractical, necessitating a shift towards alternative, sustainable fuel sources that can meet energy requirements without causing pollution and are long-lasting.

1.3 Renewable Sources of Energy

Renewable sources of energy are those derived from natural processes that are continually replenished. These sources offer sustainable alternatives to finite fossil fuels and have the potential to play a significant role in addressing energy security, climate change, and environmental sustainability. Here are some of the key renewable sources of energy:

Solar Energy: Solar energy is derived from the radiation of the sun. It can be captured and converted into usable electricity through photovoltaic panels, which directly convert sunlight into electricity, or through solar thermal systems, which use mirrors or lenses to concentrate sunlight for heating water or generating steam to drive turbines.

Wind Energy: Wind energy is generated by harnessing the kinetic energy of the wind with wind turbines. These turbines convert wind energy into mechanical power, which is then converted into electricity using generators. Wind energy is abundant, widely available, and can be deployed onshore or offshore to maximize energy production.

Hydropower: Hydropower, or hydroelectric power, utilizes the energy of flowing water to generate electricity. It is one of the oldest and most widely used forms of renewable energy, with large-scale hydroelectric dams providing a significant portion of the world's electricity supply. Small-scale hydropower systems can also be deployed in rivers and streams to power remote communities or off-grid facilities.

Biomass Energy: Biomass energy is derived from organic materials such as wood, crop residues, and agricultural waste. These materials can be burned directly for heat or converted into biofuels like ethanol and biodiesel for use in transportation and heating applications. Biomass energy is considered renewable when managed sustainably, as new biomass can be grown to replace harvested crops or trees.

Geothermal Energy: Geothermal energy is produced by harnessing heat from the Earth's interior. This heat can be accessed through geothermal reservoirs, where hot water or steam is extracted from underground wells and used for heating buildings or generating electricity using geothermal power plants. Geothermal energy is reliable, available around the clock, and emits low levels of greenhouse gases compared to fossil fuels.

Tidal and Wave Energy: Tidal and wave energy are generated by the gravitational forces of the moon and sun and the kinetic energy of ocean waves. Tidal energy is captured using tidal turbines placed in tidal streams or estuaries, while wave energy is captured using wave energy converters deployed offshore. These marine energy sources have the potential to provide consistent, predictable electricity generation near coastal areas.

Each of these renewable energy sources offers unique advantages and challenges, and the optimal mix of renewables may vary depending on factors such as geographical location, resource availability, technological maturity, and policy framework. By diversifying the energy mix and transitioning to renewable sources, societies can reduce dependence on fossil fuels, mitigate climate change, and promote sustainable development.

1.4 Wind Turbines

Wind power plays a crucial role in addressing the global energy crisis (Gupta, 2015; Amano, 2017). Wind turbines are the devices for capturing wind energy and converting it into electricity. Depending on the orientation of the rotational axis, these turbines are commonly categorized as horizontal-axis wind turbines (HAWTs) and vertical-axis wind turbines (VAWTs). The HAWTs have a rotation axis aligned parallel to the incoming wind direction, whereas the VAWTs rotate crosswise to the incoming wind direction. The HAWTs are commonly used in areas with higher energy demand and larger coverage as compared to VAWTs. Unlike VAWTs, the HAWTs require a yaw mechanism to operate and are not self-starting (Ogawa, 1989; Wong et al., 2017; Alom and Saha, 2018; Talukdar et al., 2022). Additionally, there are on-shore and off-shore HAWTs designed to extract wind power from land and oceans, respectively. Although the HAWTs have seen significant advancements, they tend to be expensive and require extensive infrastructure for power transmission and distribution, making them less suitable for remote or inaccessible areas. Recently, the interest in VAWTs is growing due to its advantages, including wind direction independence, lower noise, ease of installation, maintenance, and potential for domestic energy solutions (Al-Bahadly, 2009). Among the VAWTs, the Savonius wind rotor stands out for their structural simplicity, requiring minimal initial torque, and achieving an efficiency of around 30% (Mojola, 1985; Ogawa, 1989; Wong et al., 2017; Talukdar et al., 2022;). The Savonius rotors offer cost-effective power generation compared to other VAWTs, such as H- and Φ type Darrieus rotors. The Savonius rotors, on the other hand, present an attractive solution for smaller and fluctuating energy demands. Figure 1.2 represents a typical Savonius rotor showing the torque produced by the advancing and the returning blades (front view), while the top view depicts the forces (lift and drag) acting on it along with geometric parameters such as separation gap (*SG*), overlap distance (*e*) and overlap ratio (*OR*).

1.5 Rudiments of the Savonius Wind Turbine

The Savonius rotor stands out as the most straightforward among VAWTs, named after S. J. Savonius, who introduced it in the 1920s (Savonius S.J., 1930). Savonius revamped Flettener's rotor design by dividing a cylinder along its central axis, relocating the two resulting semi-cylindrical surfaces sideways, resembling the shape of an "S" when viewed from the top (Figure 1.2). These rotors can feature two, three, or more blades and can be utilized in single or multi-staged configurations. The fundamental working principle relies on the drag force difference between the convex and concave parts of the rotor blades during rotation around a vertical shaft (Faizal et al., 2010; Rathod et al., 2023).

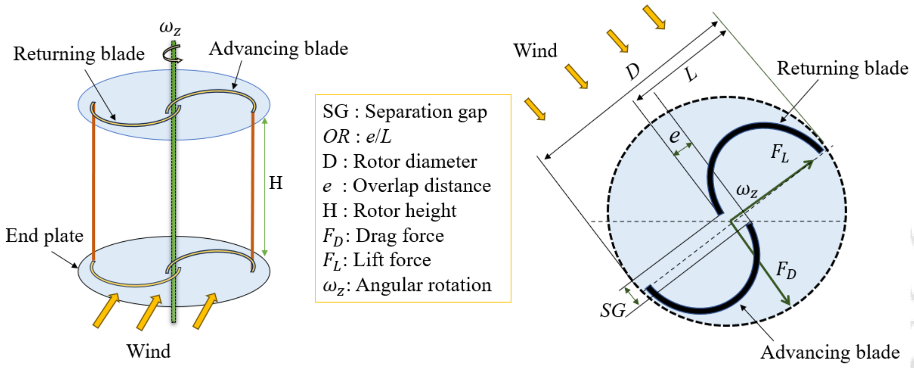

(a) Side view (b) Top view

Figure 1.2: Geometric details of a conventional Savonius wind rotor

Savonius turbines are known for their simplicity in construction, wind direction insensitivity, and self-starting capability (Ogawa et al., 1989). Throughout a complete rotational cycle, various flow patterns, including Coanda-type, dragging, overlap, stagnation, and vortex flows, are observed around the rotor. Figure 1.2 illustrates the geometric details of the conventional semicircular-bladed Savonius rotor. In comparison to HAWTs, the efficiency of VAWTs, including the Savonius rotor, is generally lower. Among VAWTs, the Darrieus rotor exhibits higher efficiency than the Savonius rotor. Due to its uncomplicated design and low construction cost, Savonius rotors find primary applications in small-scale wind power generation and water pumping. Their substantial starting torque makes them suitable for initiating other wind turbine types with inferior starting characteristics, such as the Darrieus rotor and Gyro mill (Hayashi et al., 2005). Savonius rotors with three blades demonstrate favourable torque characteristics, but they exhibit a lower maximum power coefficient compared to those with two blades (Ross and Altman, 2011). The number of rotor blades directly influences rotor performance, with studies indicating that the use of end plates on the Savonius rotor leads to performance improvements (Akwa et al., 2012). Additionally, employing twisted blades significantly enhances the power coefficient (Saha et al., 2008).

1.6 Performance Parameters

Here, the basic parameters for measuring the Savonius rotor performance are explained.

1.6.1 Torque coefficient (C_T): The ratio of the torque (*T*) produced by the turbine shaft to the torque available in wind is termed as torque coefficient (Roy and Ducoin, 2016; Fujisawa, 1992). It can be expressed by Eqn. (1.1).

$$C_T = \frac{T}{\frac{1}{2}\rho A V^2 R} \tag{1.1}$$

where T = torque [Nm], ρ = air density [kg/m^3], A = swept area [m^2], V = wind velocity [m/s], R = effective turbine radius [m].

1.6.2 Power coefficient (C_p): The ratio of turbine shaft power ($P_{turbine}$) to the available wind power ($P_{available}$) is termed as power coefficient (Roy and Ducoin, 2016; Fujisawa, 1992). It can be expressed by Eqn. (1.2). It is noted that no wind turbine can extract wind power more than the Betz limit that is 59.3% (Manwell et al., 2009).

$$C_P = \frac{P_{turbine}}{P_{available}} = \frac{T\omega}{\frac{1}{2}\rho A V^3} \tag{1.2}$$

where T = torque [Nm], ω = angular velocity (rad/s), ρ = air density [kg/m^3], A = swept area [m^2], V = wind velocity [m/s].

1.6.3 Tip speed ratio (TSR): It is the ratio of tangential speed of the rotor to the inlet wind speed. It can be expressed by Eqns. (1.3) and (1.4).

$$TSR = \frac{R\omega}{V} \tag{1.3}$$

$$C_P = C_T \times TSR \tag{1.4}$$

1.6.4 Overlap ratio (OR)

The *OR* as expressed by Eqn. (1.5) is defined as the ratio of overlap distance to the diameter of the blade (Fujisawa 1992; Akwa et al. 2012).

$$OR = \frac{e}{L} \tag{1.5}$$

where, e = overlap distance [m], L = diameter of the blade [m].

1.6.5 Aspect ratio (AR)

The *AR* of the wind turbine swept area is expressed in Eqn. (1.6).

$$AR = \frac{H}{D} \tag{1.6}$$

where, D = Diameter of the rotor [m]; and H = Height of the blades [m].

1.6.6 Drag coefficient (C_d)

The drag force (F_D) is usually defined as the force parallel to the direction of the incoming air flow. The C_d is expressed as Eqn. (1.7) (Manwell et al., 2009; Roy and Saha, 2013).

$$C_D = \frac{F_D}{\frac{1}{2}\rho A (V-u)^2} \tag{1.7}$$

where, V is the wind speed, u is rotor tip speed.

1.6.7 Lift coefficient (C_L)

The lift force (F_L) is defined as the force perpendicular to the direction of incoming airflow and is a consequence of the unequal pressure distribution between the upper and lower blade surfaces. The C_L is denoted by the Eqn. (1.8) (Manwell et al., 2009; Roy and Saha, 2013).

$$C_L = \frac{F_L}{\frac{1}{2}\rho A (V-u)^2} \tag{1.8}$$

1.7 Present Objectives and Road Map

In the past, numerous experimental and numerical investigations have been done to improve the efficiency of the Savonius wind rotor by developing various blade profiles. In recent years, the optimization and soft computing techniques have also been used to optimize the various blade design parameters. While the experimental investigations provide more accurate findings; the numerical research, on the other hand, offers the flexibility to conduct extensive studies with fewer experimental limitations and lower costs. In view of this, the present study focuses on the implementation of optimization techniques (OTs) and analytical approach to develop an efficient blade profile of the Savonius rotor.

Initially, a natural cubic spline blade profile is used to generate a new blade profile using the optimization algorithms. Subsequently, another new parabolic blade profile is developed by an analytical approach. In either case, 2D unsteady simulations are carried out to find out their performance characteristics in terms of C_T and C_P over a range of *TSR*. As the numerical simulations shows superior performance of the parabolic blade profile, the wind tunnel experiments are then conducted to validate the numerical results. In summary, the following objectives are attempted in the present investigation.

- Creation of a new blade profile from a natural cubic spline curve by OTs and study of its performance characteristics by numerical simulation.
- Creation of a new parabolic blade profile by an analytical approach and study of its performance characteristics by numerical simulation.
- Wind tunnel tests of two-bladed rotor fabricated from superior blade design.

The roadmap of the present investigation is depicted in Figure 1.3.

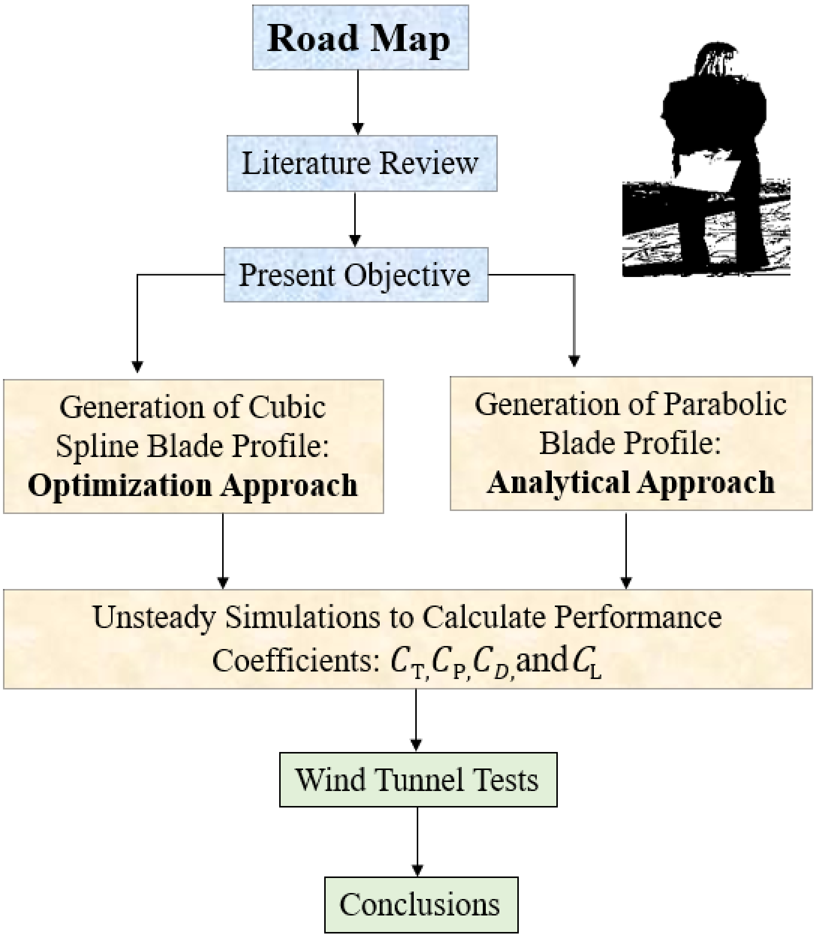

Figure 1.3: Road map of the present study

1.8 Organization of the Thesis

This report is structured to focus on enhancing the design and efficiency of the Savonius rotor. In **Chapter 1**, the motivation behind the work in the field of wind energy is presented, along with a brief introduction to the current energy landscape and the Savonius rotor. **Chapter 2** provides the literature review of the Savonius wind rotor. **Chapter 3** delves into the implementation of optimization algorithms followed by 2D unsteady investigations of different geometric parameters of the Savonius rotor. Moving forward, **Chapter 4** details the 2D computational investigations of the newly developed parabolic Savonius rotor profile. **Chapter 5** outlines the analysis of the lift and drag of the designed blade profiles. In **Chapter 6** wind tunnel tests are performed to check the practical feasibility. Finally, **Chapter 7** summarizes the conclusions drawn from the research and suggests potential future scopes for further exploration.

Chapter 2

Literature Review

Chapter Outline

2.1 Introductory Remark

Since the 1980s, numerous researchers have engaged in both experimental and numerical inquiries aimed at enhancing the design and effectiveness of Savonius rotors. However, the majority of these studies primarily focused on the conventional semicircular blade configuration. Some researchers have undertaken both experimental and numerical examinations, exploring various geometric and aerodynamic parameters to enhance the rotor's aerodynamic efficiency. While these efforts yielded notable performance enhancements, the resulting designs appeared to be more intricate and costly. Additionally, improvements in performance coefficients and static torque characteristics were documented through the implementation of various augmentation techniques. This chapter provides a comprehensive examination of the various issues documented in the available literature.

Although experimental investigations on various parameters have demonstrated some improvements, computational studies remain desirable for innovative research in analysing Savonius rotors. To date, several different computational fluid dynamics (CFD) methods, including the finite volume method (FVM), finite element method (FEM), and finite difference method (FDM). Alongside, various turbulence models such as one-equation, two-equation, and hybrid CFD turbulence models, as well as soft-computing techniques like artificial neural networks (ANN) and fuzzy logic, have been employed by numerous researchers to enhance Savonius rotor performance. This chapter aims to consolidate the optimization techniques opted to provide a comprehensive understanding of the different methods utilized and their impact on predicting Savonius rotor performance and the associated flow physics around the rotor blades.

2.2 Impact of Design Variables

Design variables such as tip speed ratio (*TSR*), overlap ratio (*OR*), aspect ratio (*AR*), number of blades (*K*), number of stages (*N*), and their effects on the performance of the rotor are discussed in the following subsections.

2.2.1 Tip speed ratio (*TSR*)

The *TSR* is a non-dimensional variable defined as the ratio of rotor tip speed to the wind speed, that affects rotor power coefficient (C_P). Numerous research work has been done to find the optimum *TSR* at which the Savonius rotor gives the optimum performance. Many researchers found the optimum result in a range of the *TSR*, while some others gave the exact value of the *TSR* for the optimum result. Experimental studies on the effect of *TSR* are shown in Table 2.1, where it is observed that there is no specific value of *TSR* for the maximum C_P. However, it can be inferred that the optimum range of *TSR* could range from 0.6 to 1.0. Moreover, Table 2.2 represents the computational findings on the *TSR*.

2.2.2 Overlap ratio (*OR*)

The *OR* is a crucial variable that plays a vital role on the Savonius rotor performance. The static torque coefficient increases in a single-stage rotor due to an increase in overlap distance (*e*). It happens due to the fact that as *e* increases, the wind flow which passes through the gap increases. As the wind blows through the gap, it will act on the concave side of the returning blade and creates an effective thrust force. This additional thrust force further reduces the negative torque produced by the returning blade thereby increasing the rotor performance. Thus, it is necessary to get the optimum value of *OR* for making an efficient design. Ushiyama and Nagai (1982, 1988) have found an increase of C_P with an increase in *OR* from 0.1 to 0.5. In addition, they reported an improved C_P at *OR* = 0.0 than *OR* = 0.1 and 0.15 for the helical blade rotor. Fujisawa et al. (1995) obtained the highest C_P at *OR* = 0.15 for the semicircular-bladed rotor. Jian et al. (2012) found the highest performance at *OR* = 0.167 for a single staged rotor as shown in Figure 2.1. Recently, Alom and Saha (2017) also found that for an elliptical-bladed rotor the optimum *OR* is 0.15. However, some researchers have reported significant improvement in C_P at 20% (*OR*) as shown in Table 2.3. It can be inferred that in most cases the optimum *OR* varies between 0.0 to 0.2, as shown in Table 2.3.

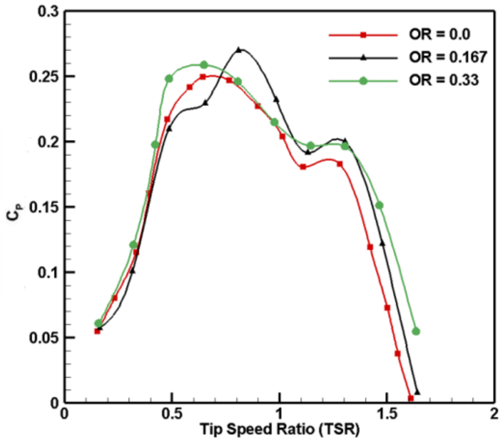

Figure 2.1: Variation of C_p with *TSR* at different *ORs* (Jian et al., 2012)

2.2.3 Aspect ratio (*AR*)

The aspect ratio (*H/D*) is one of the most important parameters of the Savonius rotor. When *AR* increases, the rotor moment-time and inertia decrease, however, the angular velocity increases. At the lower wind speed, lower *AR* is required, and vice versa. Roy and Saha (2013a) reported that the maximum C_P of the semicircular bladed rotor is at an *AR* = 0.80 as shown in Figure 2.2(a). Alexander and Holownia, (1978) executed wind tunnel experiments in the range of wind speed 6-9 m/s and reported that at lower *AR*, C_P is found to be lower for unshielded rotor without endplates, but at the same time, C_p is higher at an *AR* = 4.8, as shown in Figure 2.2(b). Alom and Saha (2018), in their review study, reported that the rotor with higher *AR* performs better at higher wind speeds, while lower *AR* models perform better at lower wind speeds. Many researchers have investigated wind tunnel studies and ended up evaluating the performance characteristics of the *AR* effect as shown in Table 2.4.

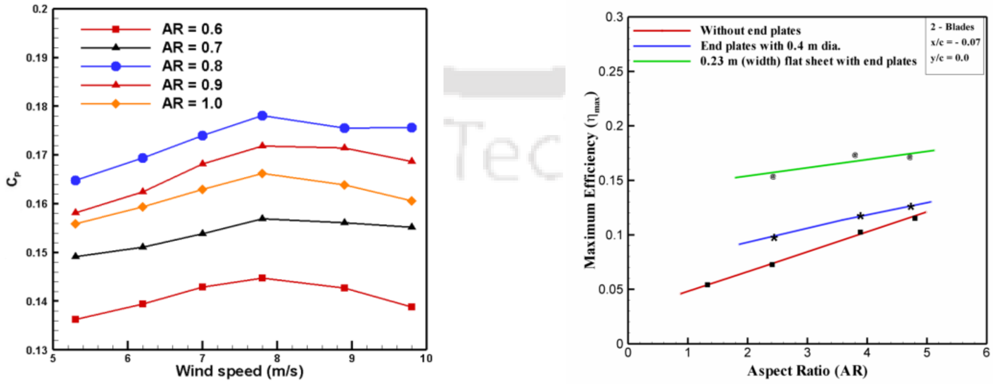

(a) Variation of C_P with wind speed (Roy and Saha, 2013a)

(b) Variation of maximum efficiency with aspect ratio (Alexander and Holownia, 1978)

Figure 2.2: Effect of *AR*s on the rotor performance

Table 2.1: Experimental study on optimum *TSR* as reported in the literature

Authors	**Study**	**System**	**Optimum *TSR***	C_{Pmax}
Alexander and Holownia (1978)	Experimental	Savonius rotor	0.52	0.25
Sivasegaram and Sivapalan (1983)	Experimental	Savonius rotor with vanes	0.45	C_P increases by 86%
Modi and Fernando (1989)	Experimental	Savonius rotor	0.79	0.32
Huda et al. (1992)	Experimental	Savonius rotor	0.68-0.71	--
Fujisawa and Gotoh (1994)	Experimental	Savonius rotor	0.67	0.17
Fujisawa et al. (1995)	Experimental	Savonius rotor	0.90	0.17
Rajkumar and Saha (2006)	Experimental	Twisted blade	0.65	0.1399
Kamoji et al. (2009)	Experimental	Helical rotor	0.7-0.9	0.175
Nasef et al. (2013)	Numerical and Experimental	Savonius rotor	0.9	0.21
Damak et al. (2013)	Experimental	Helical rotor	0.4-0.45	0.202
Jeon et al. (2015)	Experimental	Helical rotor with endplates	0.67	C_P increases by 36%
Ricci et al. (2016)	Experimental	Helical rotor	0.899	0.251
Lee et al. (2016)	Numerical and Experimental	Twisted blade	0.45	0.13

Table 2.2: Computational investigations on various Savonius rotor blade profiles

Authors	**Blade profiles**	***TSR***	**Methods**	C_{Pmax}
Ogawa (1984)	Semicircular	0.0	Theoretical	0.170
Kacprzak et al. (2013)	Bach	0.8	CFD (2D)	0.178
Song et al. (2013)	Fish-ridged	0.5	CFD (2D)	0.230
Kacprzak et al. (2013)	Elliptical	0.8	CFD (2D)	0.172
Mucolo and Molfino (2014)	Bronzinus	--	CFD (2D)	0.25
Tartuferi et al. (2015)	Airfoil shape	0.65	CFD (2D)	0.220
Alom et al. (2016)	New elliptical	0.8	CFD (2D)	0.330
Mari et al. (2017)	Spline-curved	1	CFD (2D)	0.247
Mohan and Saha (2021)	Spline-curved	0.8	CFD (2D)	0.283

Table 2.3**:** Summary of the optimum *OR* as reported in the literature

Authors	**Optimum *OR***	**Study**	C_{Pmax}
Alexander and Holownia (1978)	0.20	Wind tunnel	0.147
Mojola (1985)	0.25	Wind tunnel	0.267
Modi and Fernando (1989)	0.0	Wind tunnel	0.32
Fujisawa and Gotoh (1994)	0.15	Wind tunnel	0.17
Kamoji et al. (2009)	0.0	Wind tunnel	0.21
Kianifar et al. (2010)	0.20	Wind tunnel	0.2
Jian et al. (2012)	0.167	Wind tunnel	0.145

Table 2.4: Summary of optimum *AR* as reported in the literature

Authors	**Optimum *AR***	C_{Pmax}
Alexander and Holownia (1978)	1.2	0.147
Modi et al. (1984)	0.91	0.16
Modi and Fernando (1989)	0.77	0.32
Grinspan et al. (2004)	1.83	0.116
Saha et al. (2008)	1.58	0.32
Kamoji et al. (2009)	0.88	0.21
Zhao et al. (2009)	0.60	0.2
Dobrev and Massouh (2011)	0.91	0.208
Damak et al. (2013)	1.57	0.25
Ferrari et al. (2017)	1.1	0.202

2.2.4 Number of stages (*N*) and rotor blades (*K*)

The performance of a Savonius rotor depends on the number of rotor blades. It is evident that with the increase of *K*, wind blowing on the blades also increases at the same time and manifests itself to draw more power. Saha et al. (2008) conducted wind tunnel tests on 1-, 2- and 3-stage rotors. In each case, both 2- and 3-blade systems with semicircular and twisted blades were tested. They came up with a 2-stage rotor blade system that gives a higher C_P as compared to a 3-stage rotor with 3-bladed system using semicircular as well as twisted blades (Figure 2.3). In the legend of Figure 2.3, the first digit indicates the number of stages while the second digit indicates the number of rotor blades. The claim of a 3-bladed system to be superior to the 2-bladed system was reported earlier (Sheldahl et al., 1978). Since, then various research advancement has showcased the superiority of the 2-bladed system (D'Alessandro et al., 2010; Akwa et al., 2012).

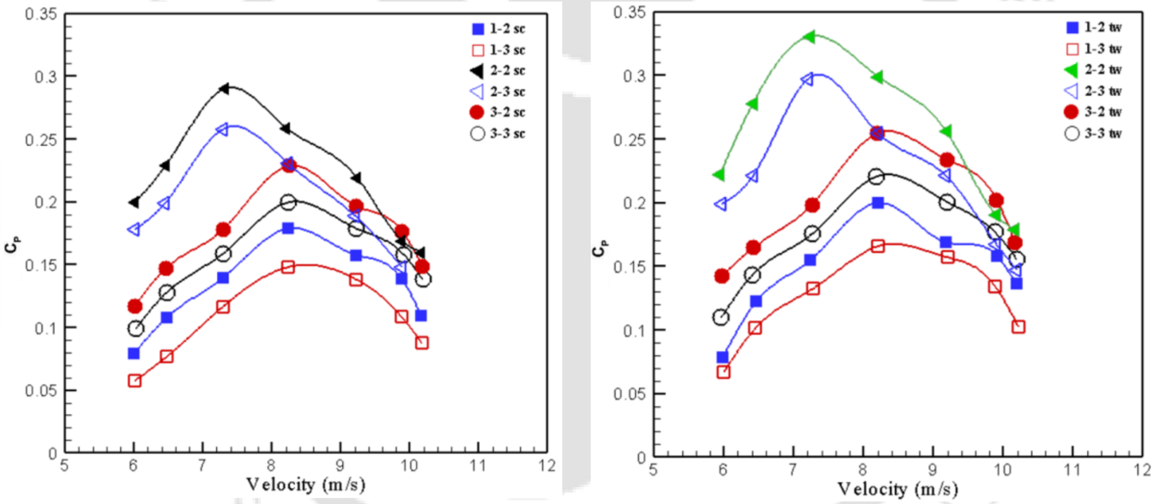

(a) Semicircular rotor (b) Twisted rotor

Figure 2.3: Variation of C_P with wind velocity for semicircular and twisted bladed at different stages of the rotor (Saha et al., 2008)

2.2.5 Reynolds number (*Re*)

The *Re* is a dimensionless variable that depicts the performance of the fluid. The increase in *Re* can increase the C_P of a Savonius rotor. Kamoji et al. (2009) obtained an increase of C_P with the increase in *Re* from 0.57×10^5 to 2.019×10^5 as shown in Figure 2.4. This is because, whenever there is a delay in flow separation across the rotor blade the *Re* increases for a specific rotor dimension. Table 2.5 summarizes the Savonius rotor studies related to *Re*.

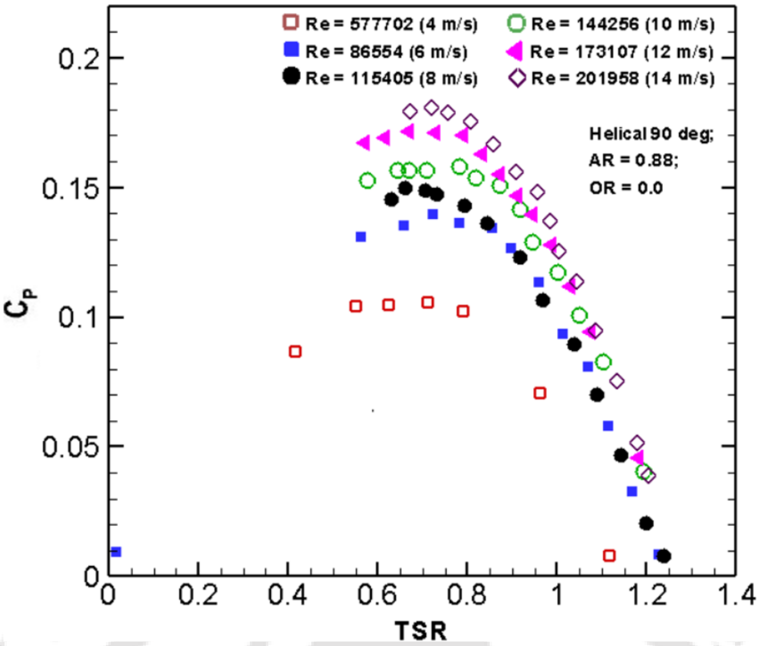

Figure 2.4: Variation of C_P with *TSR* at different *Re* (Kamoji et al., 2009)

Table 2.5: Summary of the optimum *Re* as reported in the literature

Authors	**Optimum *Re***	C_{Pmax}
Blackwell et al., (1977)	867000	0.24
Hayashi et al., (2005)	280000	0.16
Kamoji et al., (2009)	202000	0.2
Akwa et al., (2012)	867000	0.22
Damak et al., (2018)	121000	0.096

2.3 Optimization Techniques (OTs) used in Savonius Rotor

From the literature, most of the investigators have used trial-and-error methods to increase rotor performance. The OTs are a way to make good use of the process of implementing an algorithm to get a good result without using any other methods. Mohamed et al. (2011) placed an obstacle plate to shield the face of a returning blade to enhance the performance of a rotor as shown in Figure 2.5. The plate was also used to direct the incoming air properly toward the advancing blade. The automation was done by combining an open algorithm (OPAL) along with the ANSYS Fluent. Six independent variables were investigated in this optimization process that was achieved by coupling an in-house optimization library followed by an industrial flow simulation code (ANSYS-Fluent).

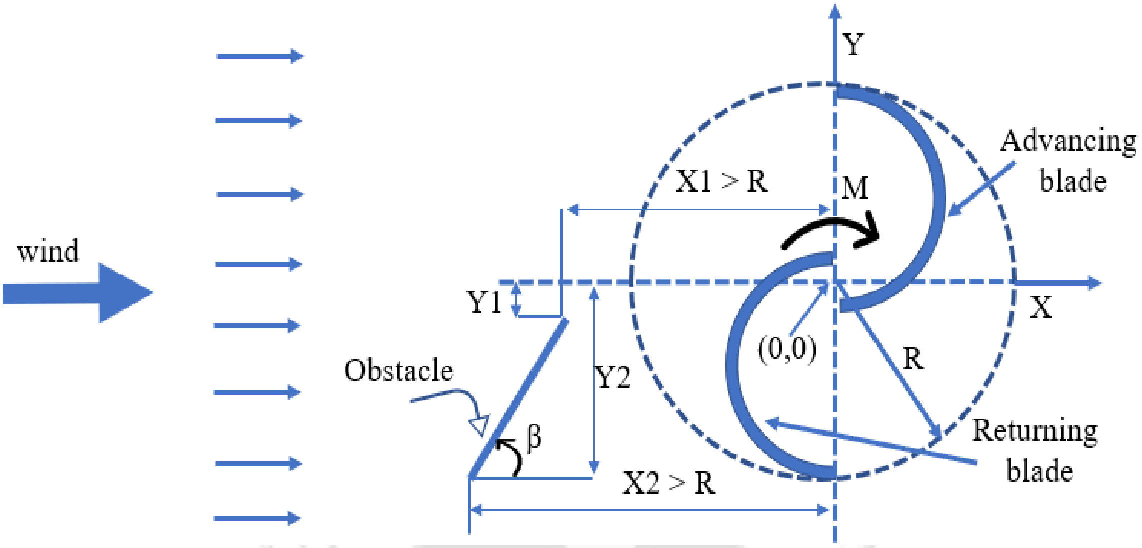

Figure 2.5: Obstacle shielding in front of the Savonius rotor (Mohamed et al., 2011)

They targeted power output as an optimization function and the results were equated with the standard semicircular rotor blade. The equivalent rise in the power output was found to be approximately 40% at the *TSR* = 0.7. The rise in performance surpasses 30% of the total working span. Eventually, the static torque was inspected and was found to be in good condition in all directions thereby showing a better self-starting ability of the rotor.

Zhou et al. (2018) investigated the potential of using a geometry evolutionary algorithm based on two-dimensional discrete cosine transformation (2D-DCT) using standardized measurements. Taking the cross-sectional area of the rotor blade into account and the 2D-DCT was used to compress and code the cross-sectional geometry into genomes, which were then converted by genetic algorithm (GA) to increase its C_P. Depending upon the numerical outcomes, the opted process enhanced the performance by 13.77% at *TSR* = 1.0 and 21.11% at *TSR* = 0.0838. The flow chart used by Zhou et al. (2018) is shown in Figure 2.6.

Ramadan et al. (2018) optimized the conventional Savonius rotor blade using the genetic algorithm, as shown in Figure 2.7. Experiments were also performed to differentiate the performance obtained from the optimum generated and the conventional rotor blade. The results obtained captured the C_P of the optimal blade at around 28% in contrast to 14%, and 10% for the 2- and 3-bladed rotor, respectively, as shown in Figure 2.8.

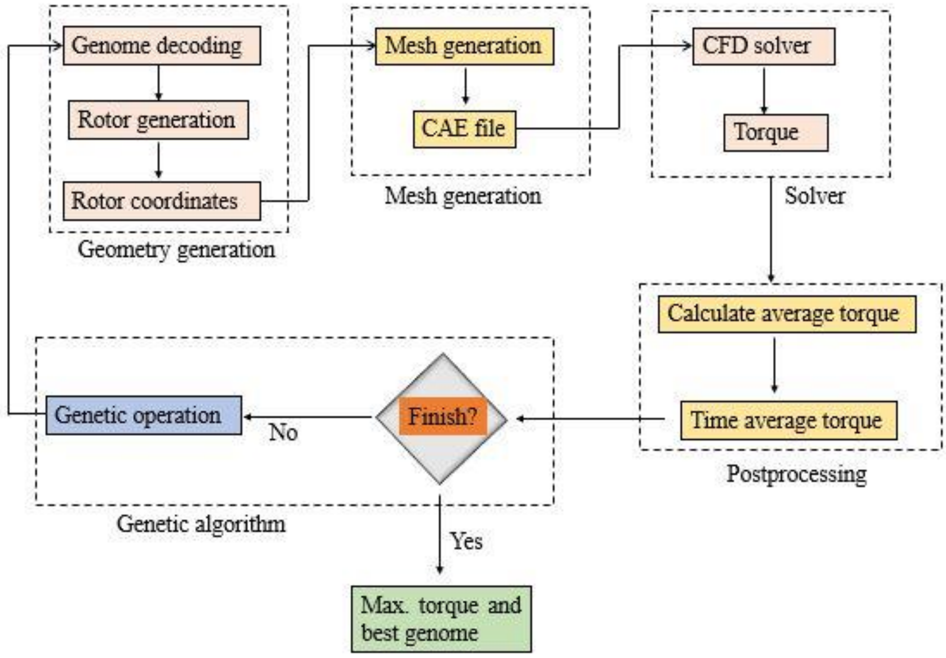

Figure 2.6: Flow chart adopted by Zhou et al., (2018)

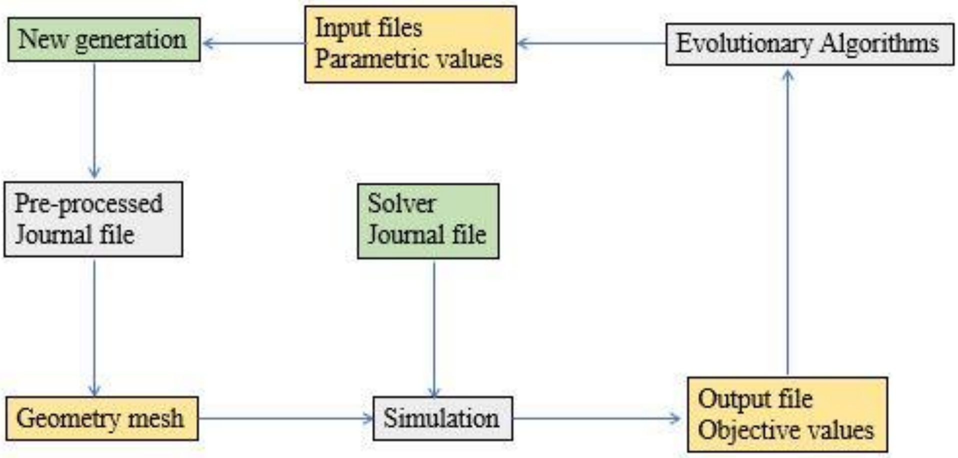

Figure 2.7: Flow chart used by Ramadan et al. (2018)

Storti et al. (2019) reported a metamodel-based OT to increase the rotor performance with deflector plates by reducing the turbine reverse moment by adopting GA integrated along with ANN and decreasing the calculation cost. The deflector geometry was investigated through the CFD model to introduce the outcome and proved the neural implant network works efficiently. This technique is used to design the deflector for an actual 8-bladed rotor, 1 kW power output, and a 2.5 m high turbine. An increment of rotor C_P was found by 30% with the use of optimized deflector (Figure 2.9). The flowchart adopted for their work is shown in Figure 2.10.

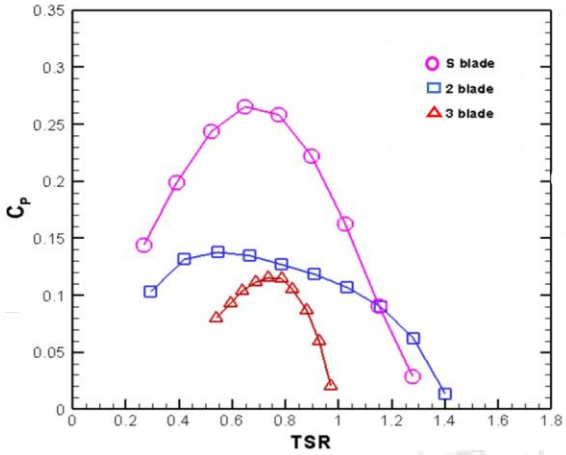

Figure 2.8: Variation of C_P with TSR of 2-, 3- and optimal blade at different *TSR* (Ramadan et al., 2018)

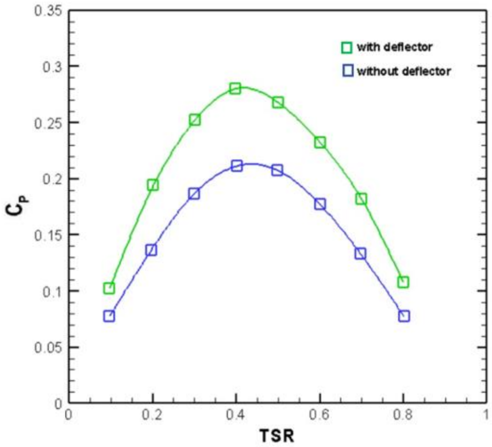

Figure 2.9: Variation of C_P with TSR without and with deflector (Storti et al. 2019)

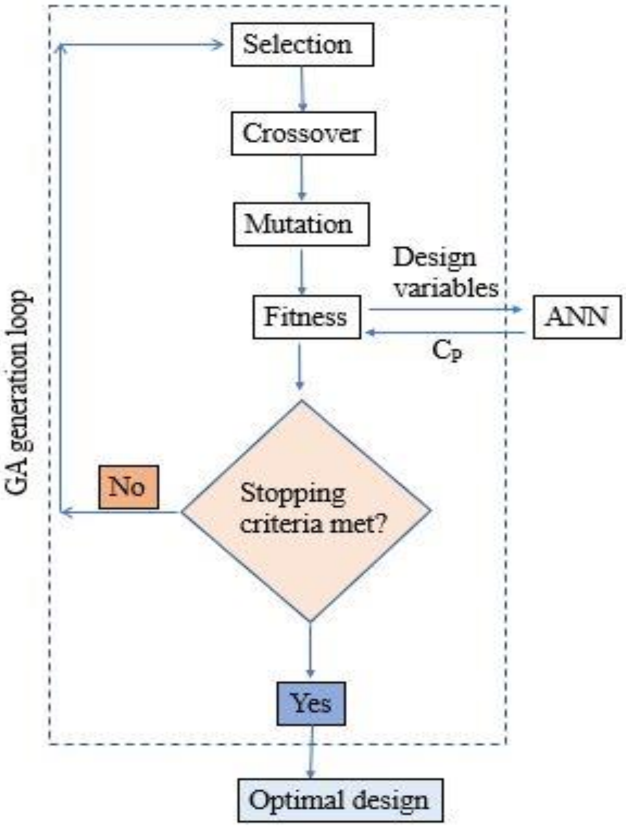

Figure 2.10: Flow chart used by Storti et al. (2019)

Roy et al. (2018) adopted the differential evolutionary (DE) algorithm as an inverse optimization method and reduced the overall swept area by 9.8% of the Savonius rotor for a given C_P. The technique used for optimization is shown in Figure 2.11. The other variables such as height (H), chord length (d), *OR* and *AR* were also predicted. The rotor torque and power characteristics are found to be sensitive to H and *AR*. Mohammadi et al. (2018) reported on the use of ANN and GA to find the relationships among all the parameters such as *OR*, N, and revolution of the rotor. The calculated C_P was a function of six independent input variables depending upon the experimental data obtained from the correlated articles (Kamoji et al. 2009). The ANN was asked to investigate the logical interaction between the dependent and independent variables and to define the cost-effectiveness based on the specific technical data. GA improved the performance function, and there were the best results for each parameter.

Masdari et al. (2019) performed the optimization study on the airfoil-type Savonius rotor. They used discrete vortex method (DVM) code to calculate C_P, while the class shape transfer (CST) was used as a performance code to generate the airfoil coordinates. Finally, the salp swarm algorithm (SSA) code for the optimization was invoked to make the best use of them. The decision variables of the problem were CST functions, whereas the objective function was to maximize the C_P. Their results of the optimum geometry showed an increase of rotor C_P by 27%. In addition, the suction area and the intensity of the side pressure of the airfoil type of rotor are found to be more than the conventional Savonius rotor with optimization (Figure 2.12). The airfoil type rotor creates a large pressure force variation on the blade surface and results in an increment of the C_P. Tian et al. (2018) investigated the modified Savonius rotor with various convex and concave sides to maximize the C_P by adopting an optimization procedure. A series of temporary comparisons of CFD was executed to obtain the C_P for each blade geometry. Subsequently, the global response model was developed under the Kriging method (Kerikous and Thevenin, 2019), which defines the relationship between the goal of optimizing C_P and other design variables.

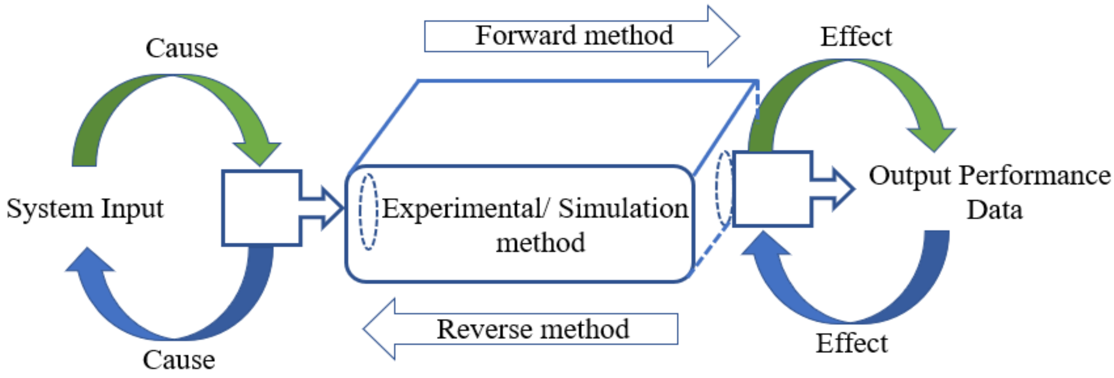

Figure 2.11: Forward and Inverse OT (Roy et al., 2018)

The particle swarm optimization (PSO) algorithm is used to determine the optimal design depending on the response surface model. The optimal C_p obtained is 0.258, which is 4.4% higher than the conventional design. Complete comparisons of torque, power, and flow structure across the optimal and conventional designs were made to showcase the blade shape's role in the rotor performance. By adjusting the Savonius blade profile, Kerikous and Thevenin, (2019) found an increase in power output of the hydraulic rotor. The dissimilarity in this study as compared to previous studies is that the concrete shape of the concave and convex sides change freely as there is no continuous blade size. Twelve geometric variables were included during operation to find the optimal solution, and the CFD simulations were executed by adopting an industrial flow simulation code operated by an OPAL-based library that was based on an evolutionary algorithm. The optimization process takes C_p as an output objective function. Thereafter, a comparison with the conventional Savonius rotor was made, and the average increase in C_p was seen at around 12% at the *TSR* of 1.1. The optimal geometric performance was compared to the conventional Savonius rotor throughout the working range as shown in Figure 2.13. The performance increment was found to be around 15% at *TSR* 1.2. The optimal design showed better performance throughout the operating range of *TSR*. Apart from this, *TSR* 0.8 turned out to be the optimal value and the design is still self-starting in nature.

Zheng et al. (2019) increased the combined power output of cluster of three Savonius rotors using GA, where four cases were studied for various amalgamation of rotational directions. The optimal cluster had a very high 37% increment of C_P over a single Savonius rotor system obtained at $TSR = 0.8$. The consequential increment in the rotor performance in an optimal cluster was due to constructive coupling in the flow field. Two main effective methods of coupling were adopted depending upon flow structures to explain the increased performance. In addition, a process was proposed to enlarge the entire cluster into a compact wind farm. He et al. (2019) used GAs along with CFD simulations, where a significant improvement of C_P by 34% was noted along with the optimal blade and optimal deflector as shown in Figure 2.14. In the rotor with an optimal deflector, its time-averaged C_P could be increased by 95% against the one without a deflector. The selected method focused on performance improvement, which is discussed depending on numerical field data through CFD simulations. The summary of the various optimization techniques adopted by several investigators is shown in Table 2.6.

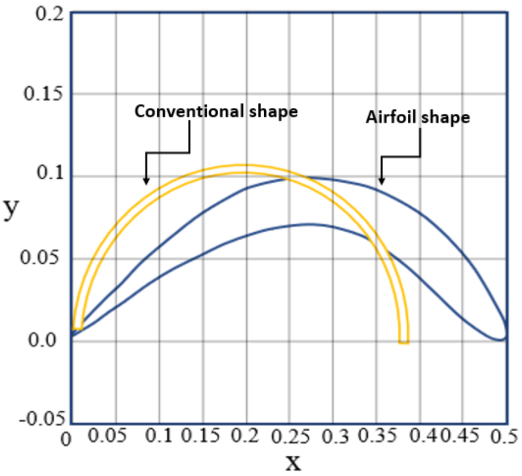

Figure 2.12: Geometry of the airfoil type and the semicircular blades (Masdari et al., 2019)

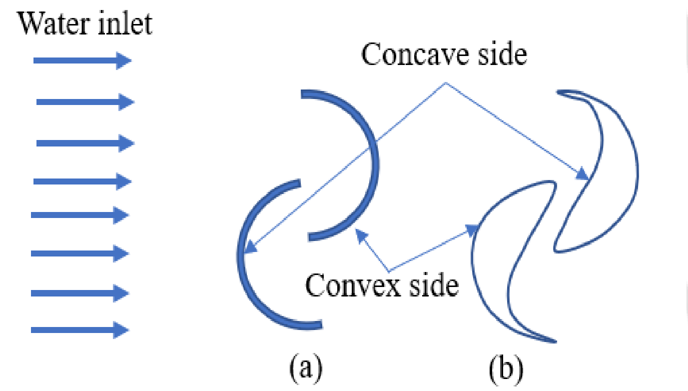

Figure 2.13: Comparison between (a) conventional blade and (b) optimal blade (Kerikous and Thevenin, 2019)

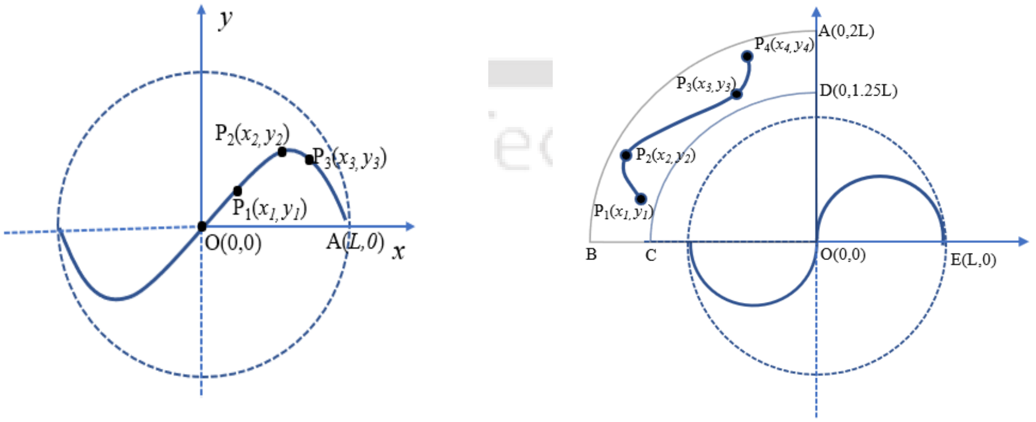

(a) Blade (b) Deflector plate

Figure 2.14: Optimization of the blade and the deflector plate (He et al., 2019)

Table 2.6: Summary of various OTs used by several investigators

Author	Blade shape	Methods	Environment/Tool	Major Findings
Mohammed et al. (2011)	Semicircular	Evolutionary Algorithms	OPAL with ANSYS Fluent	A relative increase in C_P by almost 40% at $TSR = 0.7$
Zhou et al. (2018)	Semicircular	2D discrete cosine transformation	Quantitative measurements	13.77% improvement in C_P at $TSR = 1.0$ 21.11% improvement in C_P at $TSR = 0.0838$
Ramadan et al. (2018)	Semicircular	GA	Optimization coupled with CFD	C_{Pmax} for optimal blade shape is 28% C_{Pmax} for 2- and 3- bladed semicircular rotor is 14% and 10%, respectively.
Mohammadi et al. (2018)	Semicircular	ANN and GA	MATLAB and ANSYS Fluent	C_{Pmax} for optimal blade shape is 22.2%
Roy et al. (2018)	Semicircular	Differential EA	MATLAB	Reduced the overall area by 9.8%
Chan et al. (2018)	Cubic spline	GA	Optimization coupled with CFD	Obtained C_{Pmax} = 33% more than the semicircular blade profile
Tian et al. (2018)	Different sides	PSO	CFD	Obtained performance is 4.41% higher than the conventional semicircular
He et al. (2019)	Semicircular	GA	Optimization coupled with CFD	The optimized blade is showing a 34% power coefficient than the semicircular
Alom et al. (2019)	Elliptical	Differential EA	MATLAB	Reduced the swept area by 6.25%
Alom et al. (2019)	Elliptical	MOGA	ANSYS Fluent	C_{Pmax} for elliptical profile = 35% at V = 5.91 m/s C_{Pmax} for semicircular profile = 35% at V = 5.91 m/s
Storti et al. (2019)	Semicircular	GA and ANN	Code-Saturne	Increase in efficiency by 30%
Masdari et al. (2019)	Airfoil	Salp Swarm Algorithm	CST, DVM, and SSA codes	Improvement of C_{Pmax} by 27%
Kragic et al., (2019)	Semicircular	GA	Mode Frontier and ANSYS FSI	Improvement of C_{Pmax} by 8%
Kerikous et al. (2019)	Semicircular	OPAL++ relies on an Evolutionary algorithm	CFD	Improved performance by 15% at a $TSR = 1.2$
Antar et al. (2020)	Semicircular	2D parametric optimization	CFD	Improvement of C_{Pmax} = 42.5% at a $TSR = 0.59$
Al-Shammari et al. (2020)	Semicircular	ANN	ANSYS CFX	The enhancement ratio in the power coefficient is 55%

2.4 Optimization of Rotor Blade Profile

Several researchers have performed investigations to obtain the optimum blade profiles/shape. Chan et al. (2018) optimized the shape of the Savonius rotor and obtained improvement in performance. An automated process is performed to optimize the blade shape using GA that incorporates CFD simulations into the algorithm coupling the blade geometry that is defined by the generation of the mesh along with the objective function. The flow chart adopted by Chan et al. (2018) is shown in Figure 2.15. The test is performed by a repetitive process, as shown in Figure 2.16. The optimum blade obtained shows an increment in average C_P by around 33% as compared to the conventional semicircular blade profile.

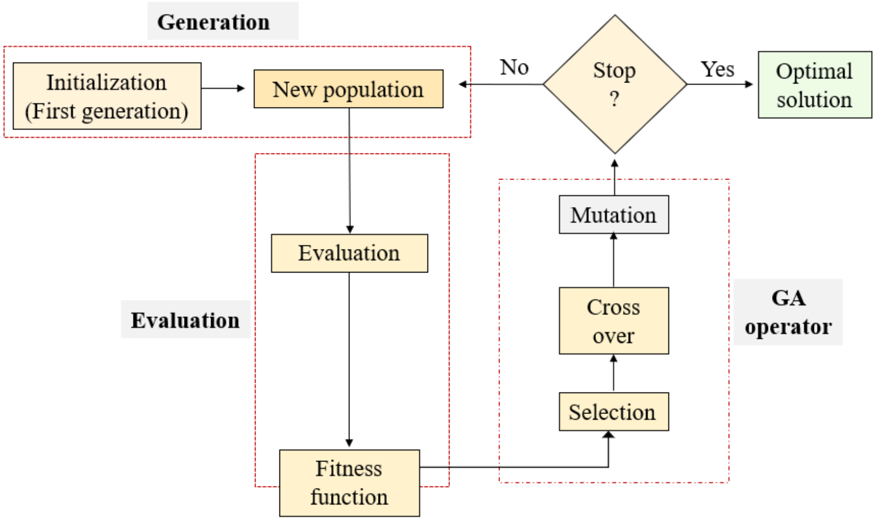

Figure 2.15: Flow chart adopted by Chan et al. (2018)

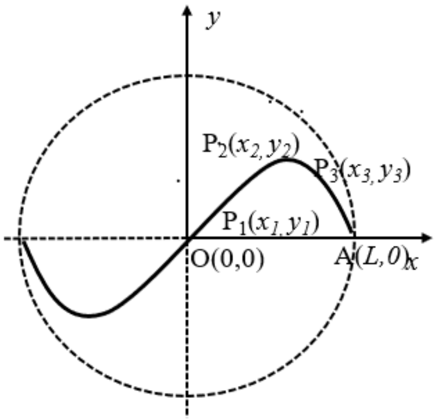

Figure 2.16: Blade skeleton with variable points (Chan et al., 2018)

Agrawal et al. (2019) investigated blade shape optimization by adopting the simplex search method (SSM) in MATLAB along with integrated computer engineering and manufacturing (ICEM) CFD for mesh generation and ANSYS Fluent simulations. The performance obtained was compared with the semicircular bladed profile in the range of TSR = 0.6-1.0 as shown in Figure 2.17. The optimized profile was produced by keeping two endpoints fixed and the third point as variable. Hence, with the use of those three points, a natural cubic spline curve was made. The geometry of the blade profile is shown in Figure 2.18. The flow chart of their study is shown in Figure 2.19. The optimized blade profile had a C_{Pmax} of 0.26, which is 13% greater than the conventional semicircular profile.

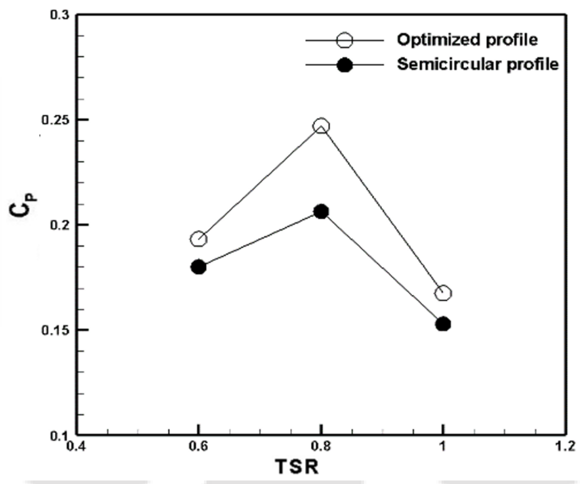

Figure 2.17: Variation of C_P with TSR of the blade (Agrawal et al., 2019)

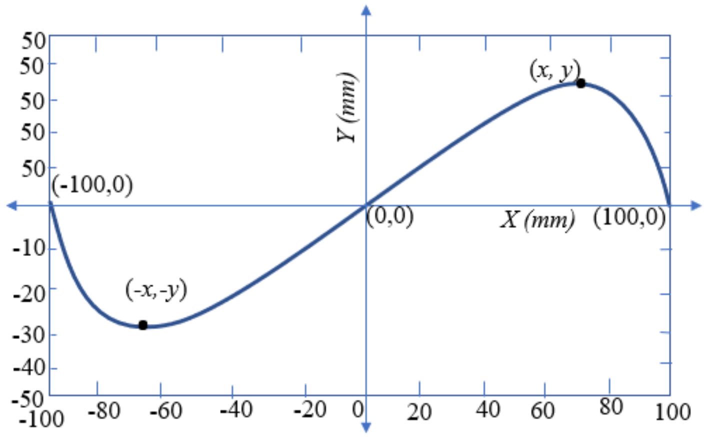

Figure 2.18: Blade skeleton with two fixed endpoints (Agrawal et al., 2019)

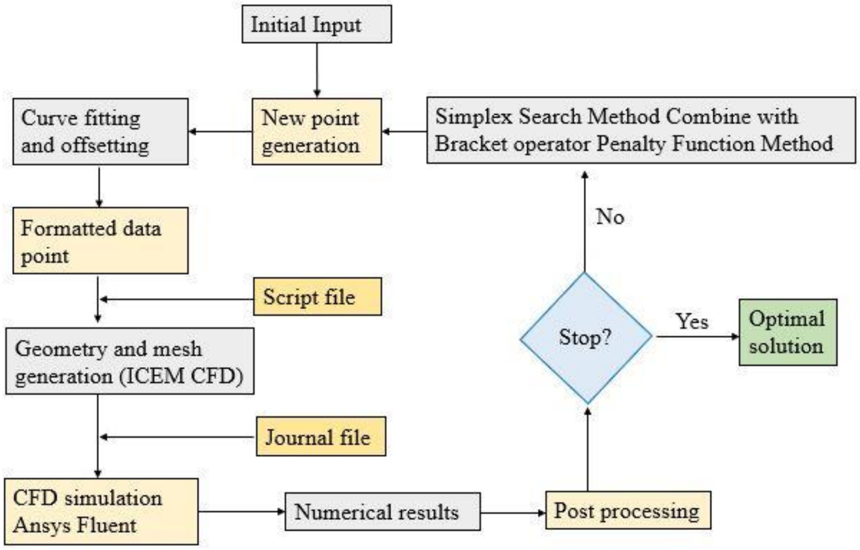

Figure 2.19: Flow chart for the SSM (Agrawal et al., 2019)

Masdari et al. (2019) optimized the airfoil-shaped Savonius rotor to maximize the C_P. To achieve the C_{Pmax}, the discrete vortex method (DVM) was used, the coordinates of the airfoil had been generated using the class shape transfer function and the coordinates were optimized using the SSA. There was an increase in C_{Pmax} by 27% against the conventional semicircular bladed rotor. Tian et al. (2018) used a particle swarm optimization (PSO) algorithm to obtain the optimal rotor blade for a Savonius rotor depending on the response surface model. The optimal C_P obtained was 0.2580, which is 4.41% more than that of conventional semicircular rotor blades. The flow chart used by Tian et al. (2018) is shown in Figure 2.20.

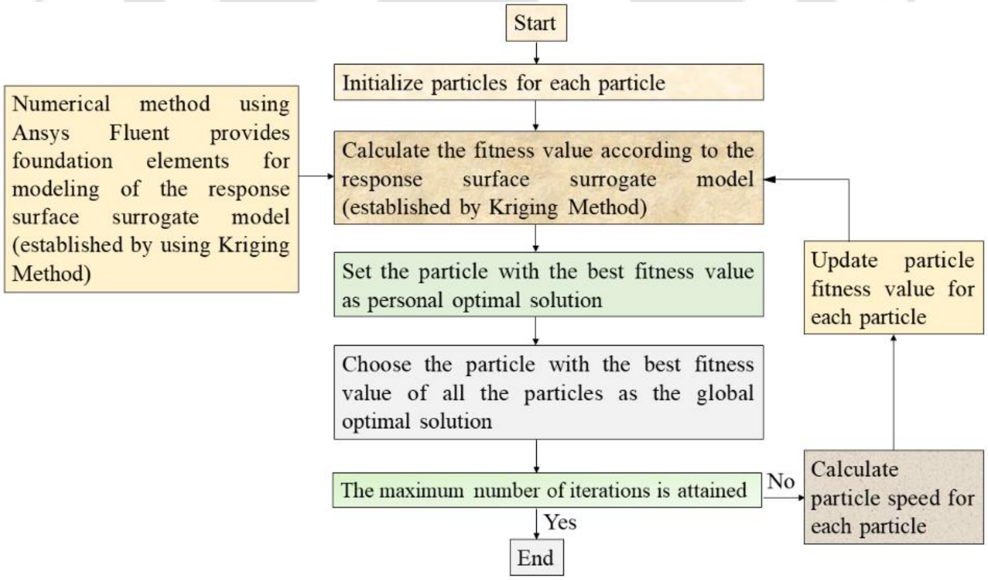

Figure 2.20: Flow chart for PSO (Tian et al., 2018)

Kragic et al. (2019) used GA to optimize the Savonius rotor blade shape. They also performed the CFD analysis along with two different fluid structural interactions (FSI) to calculate the blade design variables. The objective function was defined to calculate the optimum blade profile, blade thickness, and position of the blade support arm by maximizing the C_P and keeping the structural stress within the design limit. The analysis showed an 8% increment in C_P for the new blade shape. The flow chart adopted for their study is shown in Figure 2.21.

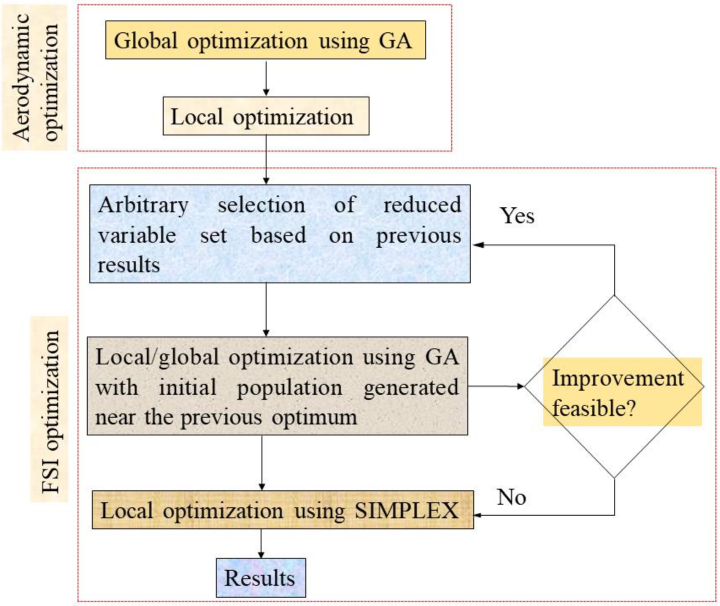

Figure 2.21: Flow chart used by Kragic et al. (2019)

There has been a host of published articles that report the use of OTs in the design and development of the Savonius rotor. It is evident that depending on the objective of the study, MOGA, ANN, and other techniques could be used. Some of the advantages of using MOGA is that multiple objective functions i.e. *TSR*, *OR*, *AR*, and C_P could be obtained. The drawback of using MOGA is that it requires many iterations to solve the problem which leads to large computational effort (Chiandussi et al., 2012). However, the GA can improve the performance function, and there can be best results for each parameter. In comparison to conventional techniques, the major advantage of GA lies with its robustness due to its qualities, viz., direct use of coding, search from a population, blindness to auxiliary information, and randomized operators (Goldberg, 1988). For the multimodal problem, the global maxima or minima can be attained by the GA very easily and efficiently. In view of the above, several investigators have used GA in the study of Savonius rotor (Ferdoues et al., 2017; Chan et al., 2018; Neto et al., 2018; Mohammadi et al., 2018).

ANN, on the other hand, is developed from biological systems (particularly the human brain). It can have some characteristics such as mapping, function approximation or regression analysis, high-speed data processing, generalization, robustness and control assignments. According to these characteristics, it can measure a set of input and output variables belonging to a specific problem (Mohammadi et al., 2018). The advantage lies with its distributed memory with parallel processing capability (Rathod et al., 2022). Its unknown duration of the network is the major drawback. Further, the function estimation given by ANN is not in the form of traditional mathematical expressions. This can be made possible by the use of latest technique viz., "genetic expression programming". Thus, depending upon objectives of the study, the specific OT can be used.

2.5 Summary

The Savonius rotor is a potential candidate for cities and isolated semi-urban areas. Therefore, a feasibility study of the Savonius rotor for its application to residential power generation in built-up and urban areas needs to be properly investigated. Having made a thorough literature review, it can be concluded that the Savonius rotor is the simplest among all the turbines. Various researchers have conducted experiments and numerical simulations to enhance the Savonius rotor efficiency. Though experimental studies are much more accurate compared to numerical studies, it has got certain limitations such as a lack of underlying theories, a proliferation of measuring instruments, inappropriate design, and diversity of experimental tasks. Besides, numerical studies have given such liberty to counter the experimental studies' drawbacks. However, the OTs provide a much more precise way of performing the design aspects such as the parametric studies on *TSR*, *OR*, *AR*, N, K, end plates, and the shape of the blades. Different shapes of the blade such as semicircular, elliptical, twisted, helical, and others have been used for performance improvement. Various augmentation techniques viz., V-shaped wedge deflector, convergent nozzle, curtain, and others have been used to improve the rotor performance. However, there are few studies that report on the use of advanced optimization algorithms and SCTs. Most of the studies have employed trial and error methods. From numerical studies, it is observed that optimization algorithms are mostly used for shape optimization to find the best profile and different optimum parameters. Based on the state-of-the-art information, the following recommendations may be made for future studies.

- The number of profiles that will be generated by different optimization techniques will increase performance by many folds, and possibly a better solution can be obtained.
- Different algorithms could also be employed to find out which algorithm converges faster and gives out better results.
- Optimization of various geometric parameters using the OTs/coupling of the OT and CFD codes.
- Out of the various optimization techniques, the ANN, GA, MOGA, and SSM are recommended to obtain the optimal Savonius rotor blade shape.
- Rotor *K* and *N* may be optimized by coupling the OTs in MATLAB and numerical simulations in ANSYS Fluent.
- *TSR* and *Re* need to be studied using OTs (GA, MOGA, and SSM) to obtain their optimal values.

The literature review discussed and presented in this chapter will help the researcher/developers in choosing and optimizing the various geometric and aerodynamic parameters of the vertical axis wind rotor using appropriate OTs. The use of OTs in the Savonius rotor blade design has been limited and requires further research. Figure 2.22 shows the flow chart for carrying out further study of Savonius rotor using the OTs.

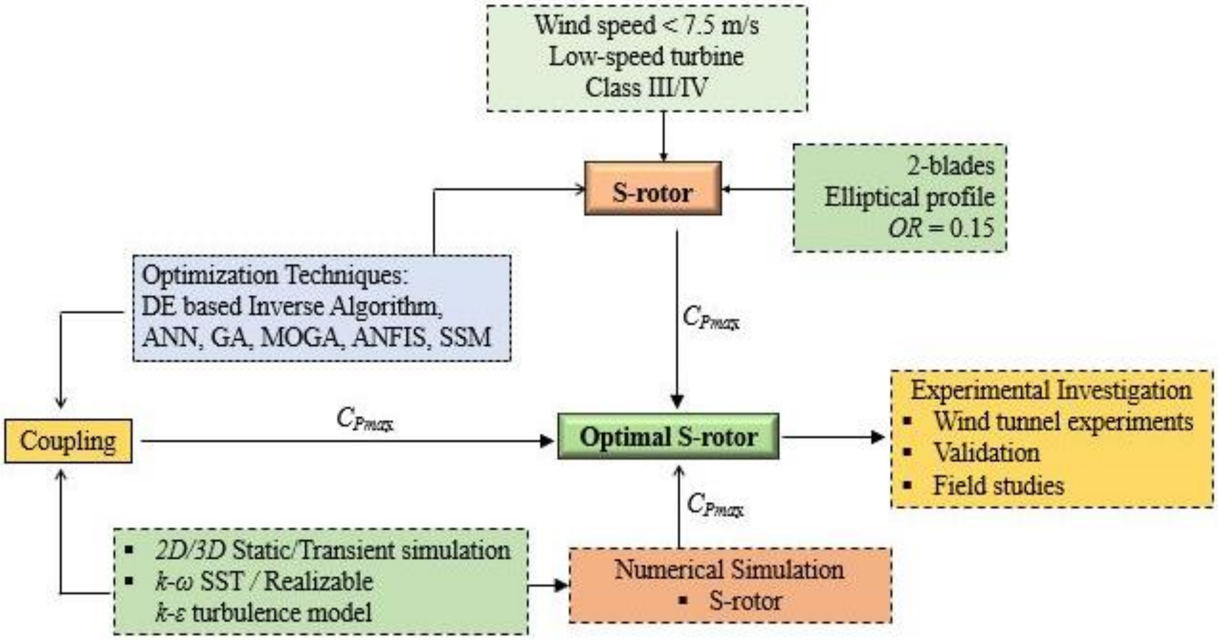

Figure 2.22: The proposed flow chart

Chapter 3

Creation of a Novel Spline Profile by Optimization and Computational Study

Chapter Outline

3.1 Introductory Remark

Optimization is defined as doing the most with the least. The most could be maximizing the profit or efficiency. This chapter aims to maximize the C_P by optimizing the Savonius rotor blade profile considering a natural cubic spline curve. This can be executed by optimizing various parameters, viz. *OR*, *TSR*, and inlet velocity (*V*) using optimization algorithms. The optimization is achieved using two different algorithms. The design validation of the rotor is performed using CFD simulations, and the C_P obtained is compared with conventional semicircular blade profile. The process followed in the whole analysis is shown in Figure 3.1.

3.2 Overview of Optimization Algorithms

Optimization algorithms are iterative procedures that compare different solutions until a satisfactory solution is achieved. Ogawa (1984) presented the first model using optimization algorithm on the Savonius wind rotor with discrete vortex method, however, the results obtained did not agree with the experimental data quantitatively. Nevertheless, the idea of implementing the optimization algorithms opened new vistas of research, and this has led to many advancements (Akwa et al., 2012; Mari et al., 2017; Chan et al., 2018; Alom et al., 2019). The optimization algorithms i.e., simplex search method (SSM), non-dominated sorting genetic algorithm II (NSGA-II), soft computing techniques, such as artificial neural networks (ANN), fuzzy logic, and adaptive neuro-fuzzy interface are used to enhance the Savonius rotor performance (Rathod et al., 2022).

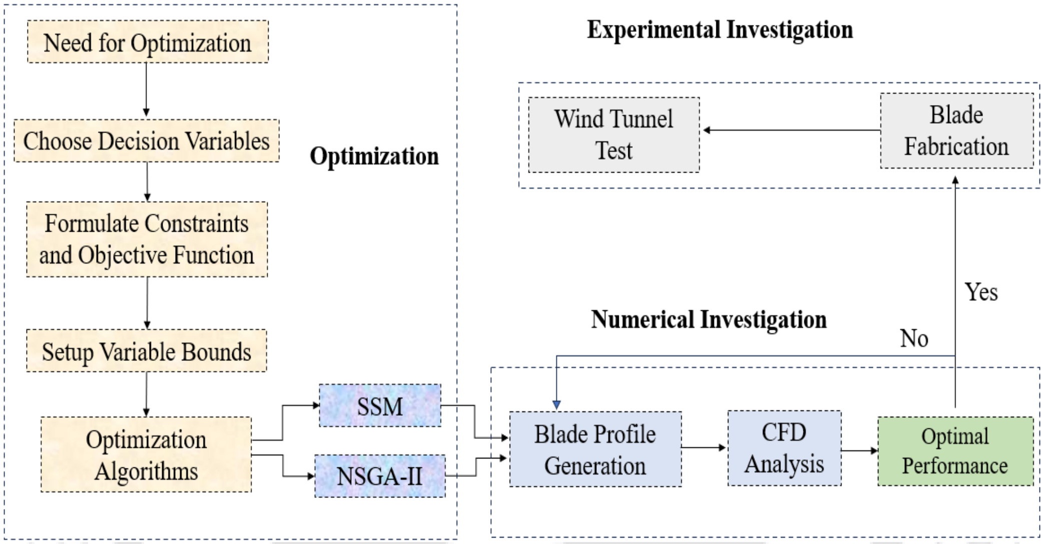

Figure 3.1: Process to get the rotor blade

In the process of optimizing a design, the primary goal can involve minimizing the production costs or maximizing the production efficiency. As the optimization process relies on software tools such as ANSYS Fluent for further calculations, the objective function calculations cannot be determined directly (Mari et al., 2017; Chan et al., 2018). This happens by coupling of the software with an automated procedure to achieve the objectives. Thus, it is important to select the algorithms to achieve the objective functions accordingly (Ravindran et al., 2006). The algorithms such as SSM and NSGA-II can be invoked in the optimization process.

3.2.1 *Simplex search method*

This method begins by creating a hypercube or simplex in the N-dimensional variable space, consisting of (N+1) points with a non-zero volume. Figure 3.2 illustrates the process of generating new points using the SSM (Agrawal et al., 2019). The objective function is evaluated at these points. Depending on the objective function, these points are segregated as the worst point (x_h), the best point (x_b), and next to the worst point (x_g). In the context of maximizing the objective function, x_h represents the point with the lowest value, while x_b corresponds to the point with the highest function value among all N points. Since the method aims to move away from the worst case, x_c is calculated as the centroid of all points to determine the worst point, and x_r is defined as 2 $x_c - x_h$.

The objective function is then evaluated at this specified point x_r. If the objective function at x_r is better than x_b, a new point is generated by extending x as $x = (1 + \gamma)\ x_c - \beta\ x_h$, where γ is a constant greater than one. In case x_r is worse than x_h, and conversely, if x_r is better than x_h but worse than x_g, the new point is then obtained by contraction as $x = (1 - \beta)\ x_c + \beta\ x_h$, where β is a constant ranging between 0 and 1 (Figure 3.3). When x_r falls within either of these cases, the new point is added to the SSM by replacing x_h. This process continues until a predetermined number of iterations are reached or the difference between the new point and the best point becomes smaller than a specified threshold value (ε). Although this approach initially functions as an unconstrained optimization procedure, there are certain limitations regarding flexible parameters. To confine the search within a specified region, the SSM is combined with the bracket operator penalty method.

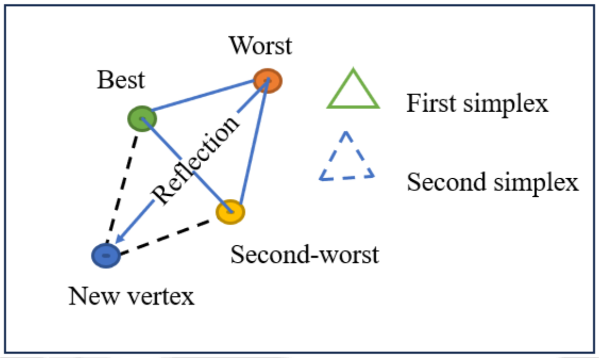

Figure 3.2: Generation of points in SSM

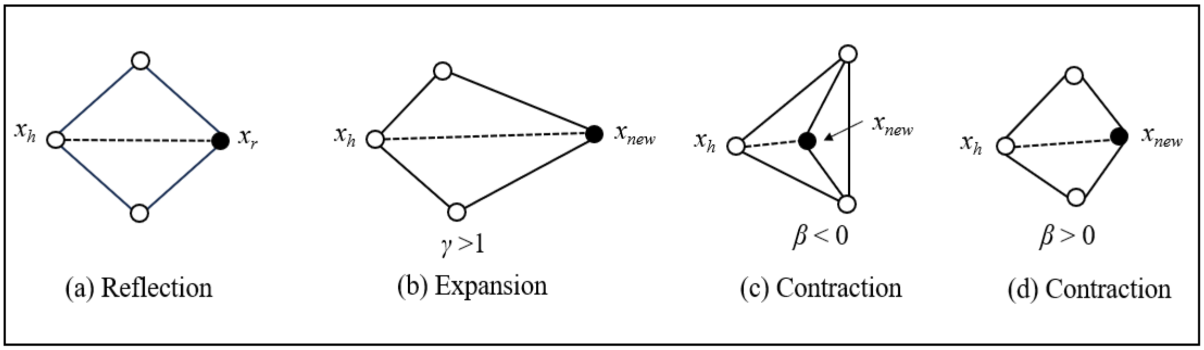

(a) Reflection (b) Expansion (c) Contraction (d) Contraction

Figure 3.3: Illustration of SSM

3.2.2 *Non-dominated sorting genetic algorithm-II*

The NSGA-II is a search algorithm commonly employed to address multi-objective optimization problems. It is done by identifying solutions in terms of non-dominated or lie on the pareto front. This algorithm incorporates various techniques such as non-dominated sorting, elitism, and a crowding distance mechanism (Chan et al., 2018). These mechanisms work together to ensure quick convergence and preserve diversity in the generated solutions. NSGA-II method is initiated by randomly generating an initial population of size N. The objective function is evaluated for this initial generation, and subsequently the population is sorted using a non-dominated sorting approach. In non-dominated sorting, individuals are divided into different fronts (F1, F2, F3, and so on) based on their non-domination levels as shown in Figure 3.4. A lower non-domination level indicates a higher quality solution. Next, a binary tournament selection is employed to generate a population of parents from the current population. Two different solutions are randomly selected, and the one with a better non-domination rank is chosen. If the solutions have the same non-domination rank, their selection is based on the crowding distance, which measures the density of solutions in the neighborhoods as illustrated in Figure 3.5. Genetic operators such as crossover and mutation are then applied to create an offspring population of size N.

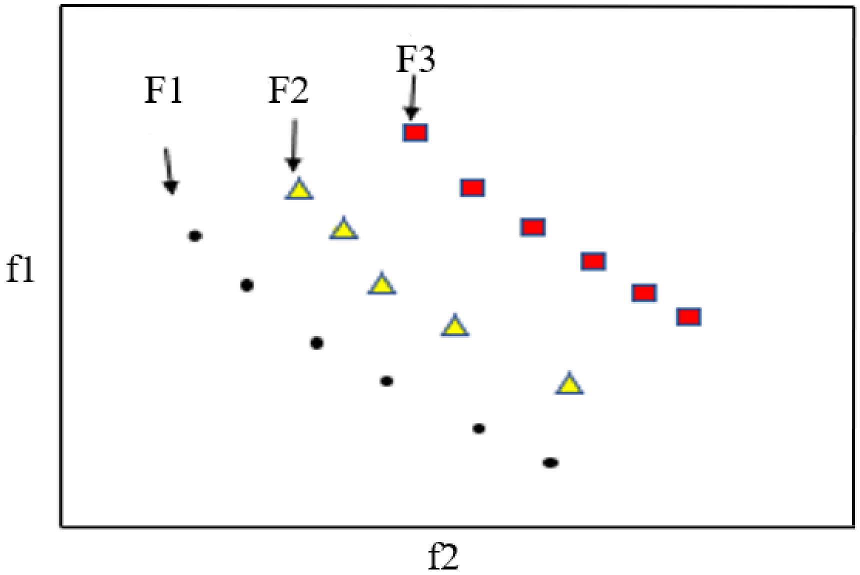

Figure 3.4: Non-dominated sorting

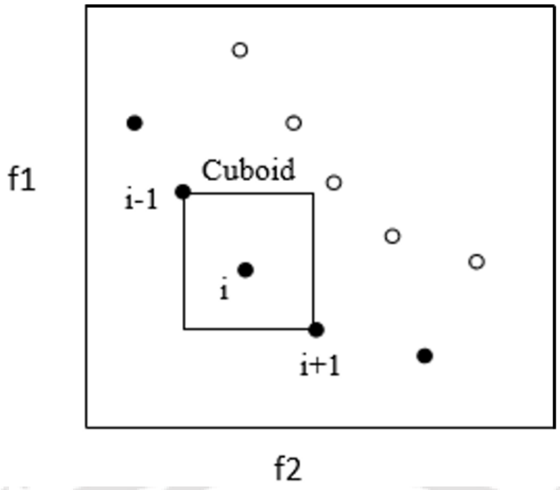

Figure 3.5: Crowding distance calculation (Chan et al., 2018)

After evaluating the objective function for the offspring population, it is sorted using the non-dominated sorting approach. The next generation is created by copying the best solutions (elitism) (Deb et al., 2002; Alom et al., 2019) or the first N individuals from the mixed population of parents and offspring. The solutions that are not copied are discarded. The selection criterion is based on the non-domination rank first, followed by the crowding distance. If the size of the first non-dominated front (F1) is smaller than N, all members of F1 are included in the new population. The rest of the slots are filled with solutions from subsequent non-dominated fronts (F2, F3, and so on) until the available slots are exhausted. The crowding distance is then calculated for each potential solution from the last rank. This process continues until a user-defined number of generations are reached, where the algorithm terminates (Mari et al., 2017). If the maximum number of generations is not attained, the process of generating offspring population continues as depicted in Figure 3.6.

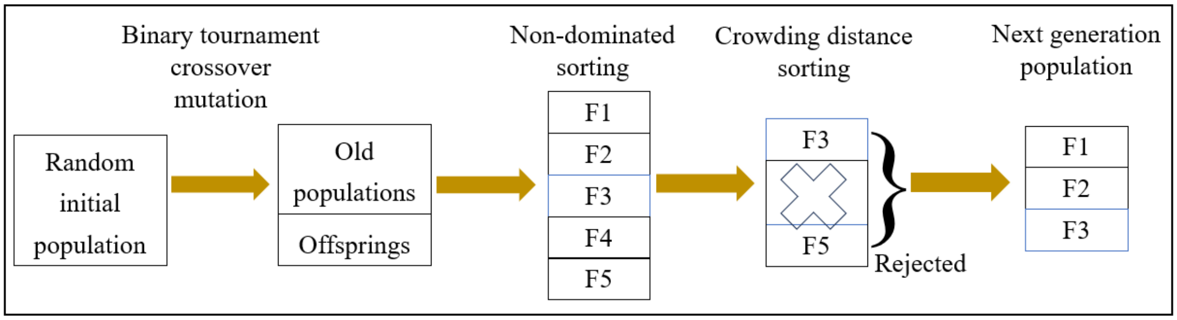

Figure 3.6: Procedure for creating generation of points in NSGA-II (Chan et al., 2018)

3.3 Optimization Problem Formulation

Due to the variability in the design objectives and the parameters across different engineering problems, it is impractical to apply a single formulation procedure universally. Usually, various techniques are employed for different design problems. The aim of the formulation process is to develop a mathematical model representing the optimal design that can subsequently be solved using an optimization algorithm. The formulations for SSM and NSGA-II are described in sub-subsections 3.3.1 and 3.3.2.

3.3.1 *SSM formulation*

The optimization problem formulation to generate a Savonius rotor blade profile (Chan et al., 2018), is given as equation 3.1.

Maximize

$$C_T\,(x, y, OR)$$

Subjected to

$$\begin{gathered} 0 < x < L. \\ 0 < y < 0.75L. \\ 0.04 < OR < 0.2 \end{gathered} \tag{3.1}$$

In eqn. (3.1), the C_T represents the time averaged torque coefficient and can be expressed as

$$C_T = \frac{T}{\frac{1}{2}\rho A L V^2} \tag{3.2}$$

where T is the torque (N.m) produced by the blade profile, L is the blade chord length (m), ρ is the air density (kg/m^3), A is the swept area (m^2), and V is the inlet air velocity (m/s).

Further, x and y in eqn. (3.1) are coordinates of the intermediate point. The two end points of the blade profile are kept fixed. Hence, the coordinates of one of the intermediate point x and y, and OR are taken as the design variable to generate the blade profile using a natural cubic spline curve.

3.3.2 *NSGA II formulation*

The optimization formulation of a Savonius rotor profile adopted by NSGA-II (Chan et al., 2018)

Maximize

$$C_P\,(x_1, x_2, x_3, y_1, y_2, y_3)$$

Minimize Inlet velocity (V)

$$\text{Subjected to} \quad \begin{array}{c} 0.05 < x_1/L < 0.3; \\ 0.3 < x_2/L < 0.7; \\ 0.7 < x_3/L < 0.95; \\ 0.1 < y_1/L < 0.6; \\ 0.1 < y_2/L < 0.75; \\ 0.1 < y_3/L < 0.6; \\ 0.6 < TSR < 1.2 \\ 5 < V < 10 \end{array} \tag{3.3}$$

The C_P in eqn. (3.3) can be expressed as eq. (3.4)

$$C_P = C_T \times TSR \tag{3.4}$$

The optimization problem aims to obtain an efficient (optimum) Savonius rotor using design variables that is the coordinate of three points (x_1, y_1), (x_2, y_2), and (x_3, y_3) along with TSR and V. The time-averaged C_P is the objective to be maximized. To get the blade profile, a natural cubic spline curve is used with three intermediate variable points, while the separation gap (SG) and OR are neglected ($SG = OR = 0$).

3.4 Process Flow Chart

A MATLAB code is deployed as a workflow platform to execute the codes sequentially using design variables. The process flow chart is depicted in Figure 3.7 where the process followed in both the optimization algorithm remains same. The SSM requires four initial random points with different spacing within the search space. Those points are defined by conclusions (-e/2, 0) and (L-e/2, 0) to describe a single blade profile. Now, using these three points of a natural cubic spline curve the blade skeleton is generated as shown in Figure 3.8. Assigning a thickness 't' by determining the inner and outer points of the blade profile, the geometry of turbine blade is created. The points on the blade surface are extracted and saved in a specific format within a .txt file. This process is repeated for other three variable points to generate the geometry of the remaining blade profiles.

The generated data points representing different geometries of the blade are imported into ANSYS ICEM CFD software to create the corresponding geometries. Once the geometry is imported, it is meshed further and is saved in a format compatible with ANSYS Fluent for simulations (ANSYS Inc, 2009; ANSYS Inc, 2015). The entire process is saved as a script file to facilitate geometry generation and meshing in subsequent iterations. The ANSYS Fluent is launched, and the simulations are performed with predefined solution setups. The results are saved as text files for subsequent iterations. The entire process in ANSYS Fluent is saved as a journal file (ANSYS Inc, 2009; ANSYS Inc, 2015). The MATLAB code reads the text file containing the simulation results and the time-averaged $C_{T.}$ The SSM is united with bracket operator penalty method to create new points and improve the optimization function until terminus. Once the final optimal blade shape is obtained, a direct comparison is made with the existing semicircular blade profile at various *TSRs*.

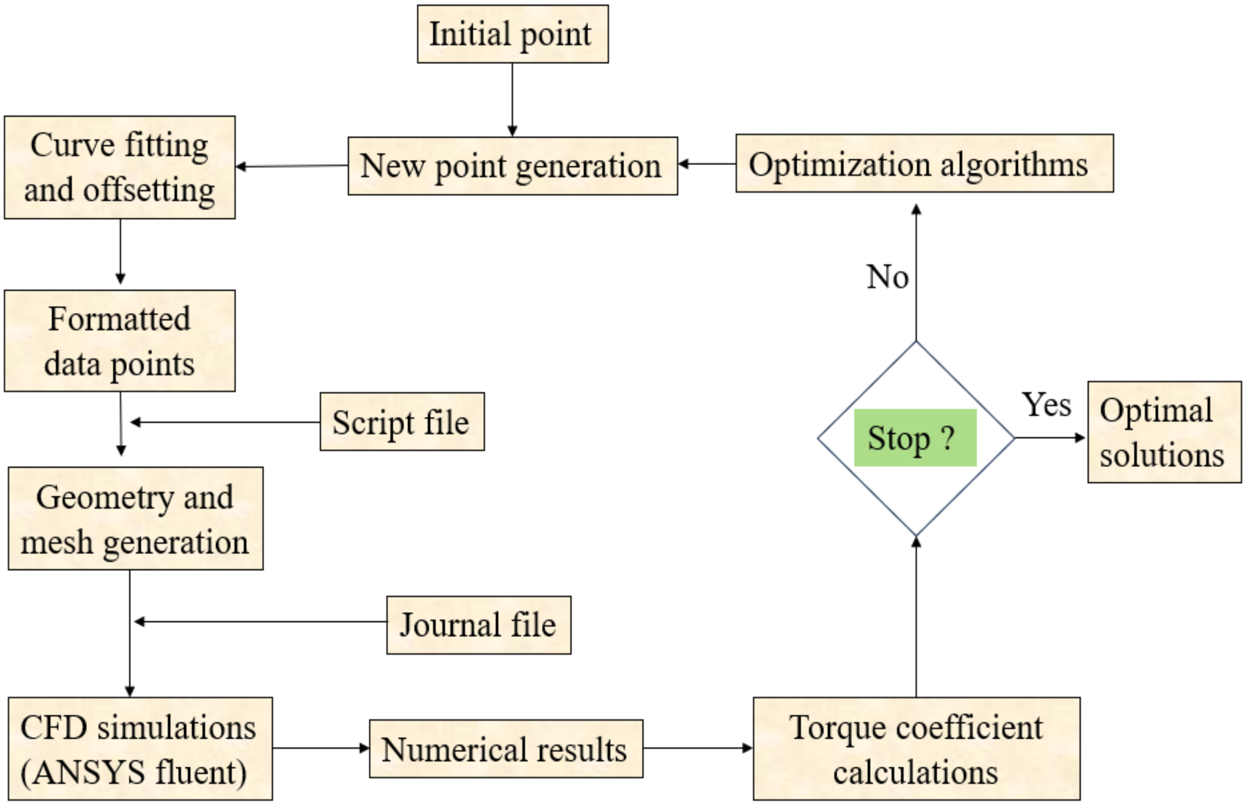

Figure 3.7: Process flow chart to obtain the blade profile.

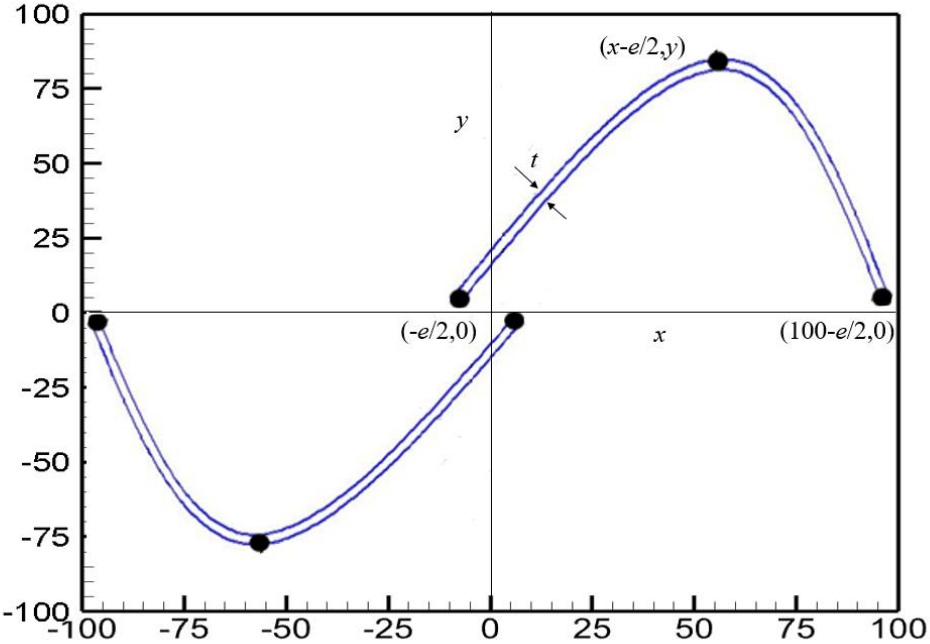

Figure 3.8: Blade skeleton generated by SSM

In NSGA-II approach, the blade profile is defined using fixed endpoints (0,0) and (L,0) along with three intermediate points (x_1, y_1), (x_2, y_2), and (x_3, y_3). An offset 't' is applied to the inner and outer surface points to create the blade geometry as illustrated in Figure 3.9. The resulting points on the blade surface are extracted and saved in a specific format of .txt file. Furthermore, three additional blade geometries are generated using the initially chosen variable points. Once the formatted data points of various blade geometries are stored, the ANSYS ICEM CFD software is employed to import the data points to generate the corresponding geometries. The meshing is done after importing the blade geometry and then meshed file is saved as a format compatible with ANSYS Fluent which further allows simulations. The entire process is automated and is then saved as a script file to streamline the geometry and meshing steps. Subsequently, the ANSYS Fluent is launched, and the simulation setup is defined. The simulation results are saved in text files, and all the operations performed in ANSYS Fluent are recorded in a journal file enabling automation for future iterations. The MATLAB code reads the text file containing the simulation results and calculates the time-averaged C_T. The optimization algorithm is then executed to generate new blade profiles. This iterative process continues until the termination conditions are met.

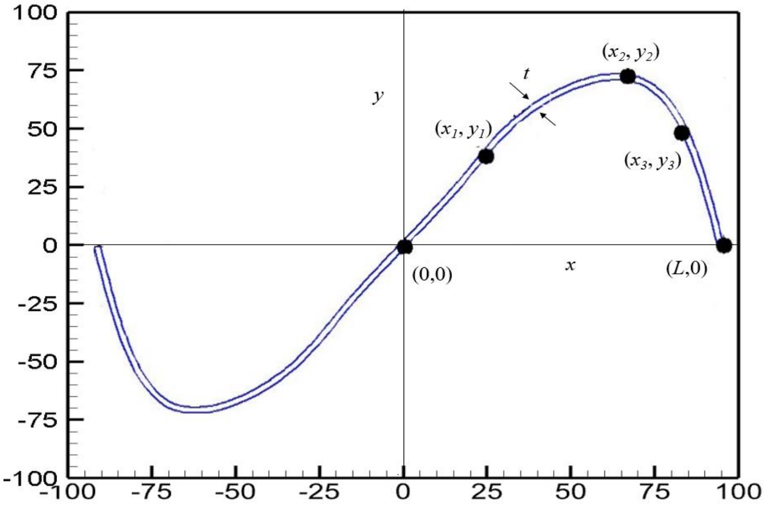

Figure 3.9: Blade skeleton generated by NSGA II

3.5 Blade Geometry

The chord length (L) of a single blade is measured as 100 mm, while the thickness (t) is 2mm as shown in Figure 3.8 and 3.9. The rotor blade rotates around the center point (0, 0), having a diameter (D) equal to $2L$ and undergoing periodic angular velocity (ω_z). The blades are separated by a gap known as overlap distance (e) (Figure 3.8). On the x-axis, we set the inlet wind speed, V = 7.30m/s (Chan et al., 2018). The corresponding angular velocity is represented on the y-axis as ω_z = 58.4 rad/s. Table 3.1 presents the geometric details and operational characteristics of the rotor.

Table 3.1 Geometric details and operational characteristics

Chord length (L)	Blade thickness (t)	Inlet wind speed (V)	Angular velocity (ω_z)
100 mm	2 mm	7.3 m/s	58.4 rad/s

3.6 Computational Methodology

The computational domain and its boundary conditions, meshing, turbulence model, solver setup, numerical model validation, grid and time independence tests are discussed in this section.

3.6.1 *Computational domain and boundary conditions*

The domain in this analysis is divided into two distinct sections. The first section corresponds to the surface where the rotor blades rotate (rotational zone), while the second section represents the stationary surface without the rotor blades (non-rotational zone), as shown in Figure 3.10. The rotating surface is specifically designed to accommodate the turbine blades and is centred at the origin. The rotational zone spans a length of 2*D*, while the non-rotational surface surrounding the rotating zone has a rectangular shape. The upper and lower edges are located at 7.5D from the origin and referred as the 'Symmetry' at the boundary. The vertical left edge is known as the 'Inlet,' positioned 7.5D from the origin, while the right edge is referred to the 'Outlet,' located at 15D from the origin. The inlet boundary condition specifies an input velocity of *V*= 7.30 m/s (Chan et al., 2018) with a maximum turbulence intensity of 1%. The pressure outlet serves as the output boundary condition and has the identical turbulence intensity. The blade surface is treated as a 'wall' with rotational motion and non-slip conditions. An interface '*Int*' is defined amid the rotational and non-rotational sections. The outer zone of the turbine is selected to ensure that the boundary remains unaffected.

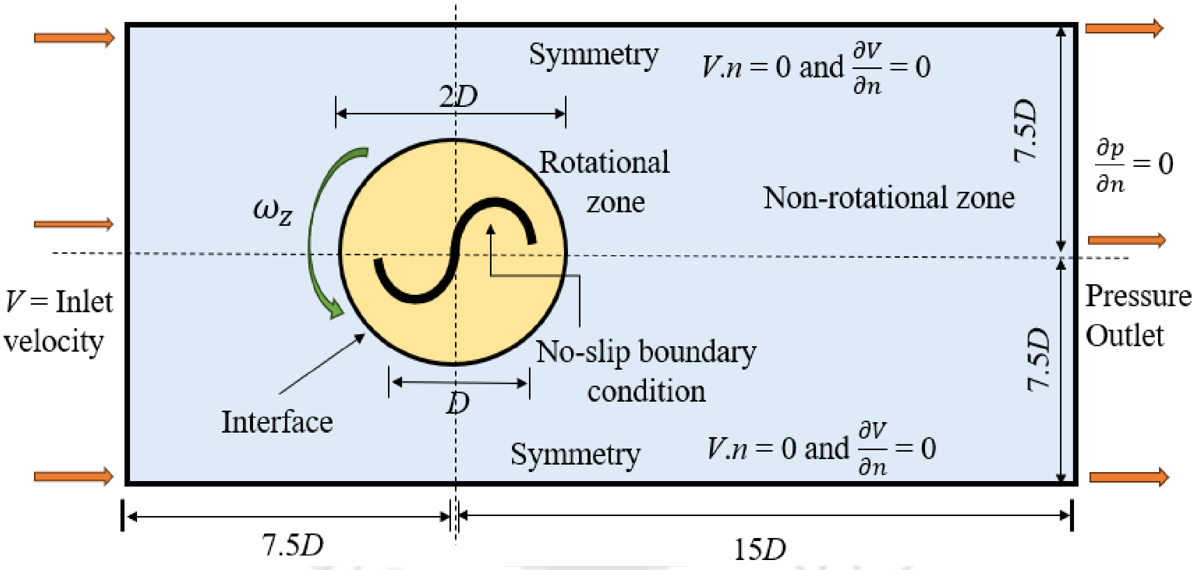

Figure 3.10: Computational domain and boundary conditions

3.6.2 *Meshing*

The FVM based ANSYS Fluent solver is used. The computational domain is divided into small control volumes and discretized to solve the Reynolds-averaged Navier-Stokes (*RANS*) equations. Due to the subsonic flow, equal accuracy can be expected in both structured and non-structured meshes. However, the unstructured mesh can be easily made in the case of complex geometry (Chan et al., 2018; Agrawal et al., 2019). In addition, due to faster generation of the grids, the unstructured mesh with all tri-elements is used to discretize the computational domain. The sliding mesh is chosen at the interface amid rotational and non-rotational zones with a rotational speed of ω_z = 58.4 rad/s and *TSR* = 0.8. The meshing of the rotational and non-rotational zones is shown in Figures 3.11 and 3.12, respectively.

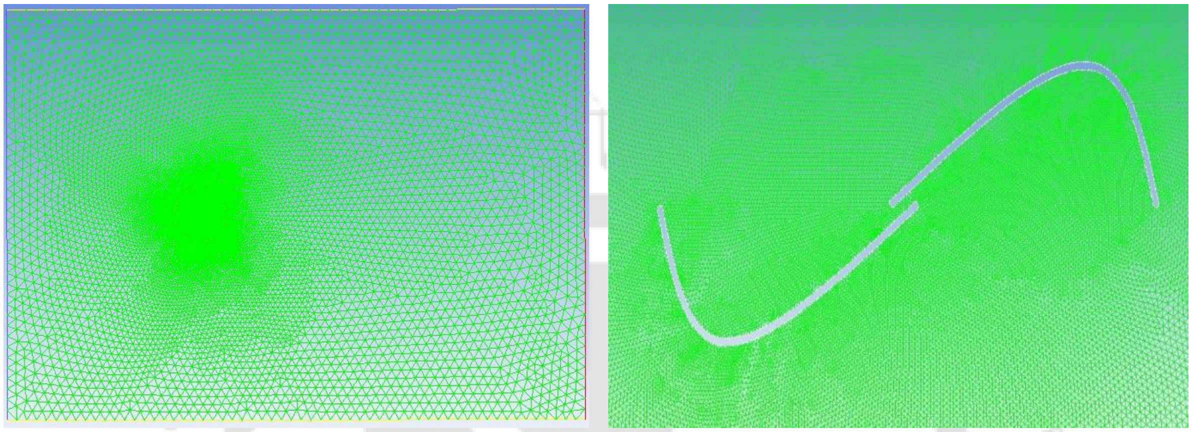
(a) (b)

Figure 3.11: Meshing of the computational domain for SSM (a) complete domain and (b) near the blade

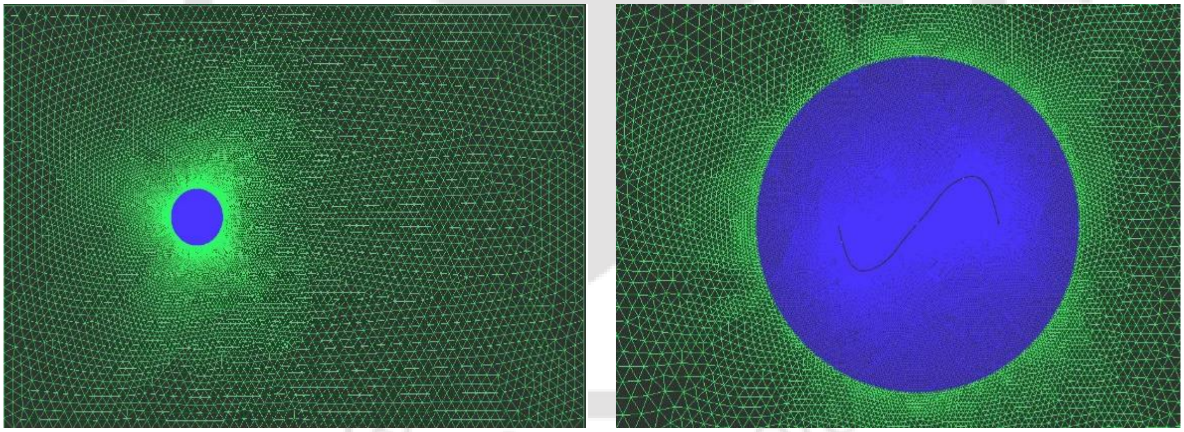
(a) (b)

Figure 3.12: Meshing of the computational domain for NSGA-II (a) complete domain, and (b) rotational domain

3.6.3 *Turbulence model*

Because of flow separation and wake generation, the flow pattern around the rotor is complex and time dependent. Such intricate unstable flow dynamics are challenging to describe. The current study uses ANSYS Fluent, a solver based on finite volume method, to perform 2D unsteady simulations. Assuming the flow to be incompressible, turbulent and invoking the Reynolds decomposition, the Navier-Stokes equations transform into eqns. (3.5-3.10):

Continuity equation

$$\frac{\partial \bar{u}}{\partial x} + \frac{\partial \bar{v}}{\partial y} = 0 \tag{3.5}$$

Momentum equations

$$\rho\left(\frac{\partial \bar{u}}{\partial t} + \bar{u}\frac{\partial \bar{u}}{\partial x} + \bar{v}\frac{\partial \bar{u}}{\partial y}\right) = -\frac{\partial \bar{p}}{\partial x} + \mu \nabla^2 \bar{u} - \rho\left(\frac{\partial \overline{u'u'}}{\partial x} + \frac{\partial \overline{u'v'}}{\partial y}\right) \tag{3.6}$$

$$\rho\left(\frac{\partial \bar{v}}{\partial t} + \bar{u}\frac{\partial \bar{v}}{\partial x} + \bar{v}\frac{\partial \bar{v}}{\partial y}\right) = -\frac{\partial \bar{p}}{\partial y} + \mu \nabla^2 \bar{v} - \rho\left(\frac{\partial \overline{u'v'}}{\partial x} + \frac{\partial \overline{v'v'}}{\partial y}\right) \tag{3.7}$$

Considering that the flow around the rotor is fully turbulent and thereby invoke the Reynolds decomposition, the aforementioned equations become

$$\frac{\partial \bar{u}}{\partial x} + \frac{\partial \bar{v}}{\partial y} = 0 \tag{3.8}$$

$$\rho\left(\frac{\partial \bar{u}}{\partial t} + \bar{u}\frac{\partial \bar{u}}{\partial x} + \bar{v}\frac{\partial \bar{u}}{\partial y}\right) = \rho g - \frac{\partial \bar{p}}{\partial x} + \mu \Delta \bar{u} - \rho\left(\frac{\partial \overline{u'u'}}{\partial x} + \frac{\partial \overline{u'v'}}{\partial y}\right) \tag{3.9}$$

$$\rho\left(\frac{\partial \bar{v}}{\partial t} + \bar{u}\frac{\partial \bar{v}}{\partial x} + \bar{v}\frac{\partial \bar{v}}{\partial y}\right) = \rho g - \frac{\partial \bar{p}}{\partial y} + \mu \Delta \bar{v} - \rho\left(\frac{\partial \overline{u'v'}}{\partial x} + \frac{\partial \overline{v'v'}}{\partial y}\right) \tag{3.10}$$

To calculate the turbulent viscosity terms in the *RANS* equations, the shear stress transport (SST) *k-ω* turbulence model is employed. The SST *k-ω* turbulence model combines the strengths of the *k-ε* model for free stream flows, and the *k-ω* model for boundary layer flows, ensuring accurate prediction of flow separation with adverse pressure gradients. The transport equations for turbulent kinetic energy '*k*' and specific dissipation rate '*ω*' are used to obtain their values in eqns.3.11 and 3.12:

$$\rho\left(\frac{\partial (k)}{\partial t} + \frac{\partial (k u_i)}{\partial x_i}\right) = \frac{\partial}{\partial x_j}\left(\Gamma_k \frac{\partial k}{\partial x_j}\right) + \tilde{G}_k - Y_k + S_k \tag{3.11}$$

$$\rho\left(\frac{\partial(\omega)}{\partial t}+\frac{\partial(\omega u_{i)}}{\partial x_i}\right)=\frac{\partial}{\partial x_j}\left(\Gamma_\omega\frac{\partial\omega}{\partial x_j}\right)+\tilde{G}_\omega-Y_\omega+S_\omega \tag{3.12}$$

In these equations, $\tilde{G}_k$ denotes the generation of turbulence kinetic energy due to mean velocity gradients. $\tilde{G}_\omega$ denotes the generation of ω. Γ_k and Γ_ω indicate the effective diffusivity of k and ω, respectively. S_ω denotes the dissipation of k due to turbulence that is user-defined source terms. The effective diffusivities for the k-ω model are determined by eqns. 3.13 and 3.14:

$$\Gamma_k=\mu+\frac{\mu_t}{\sigma_k} \tag{3.13}$$

$$\Gamma_\omega=\mu+\frac{\mu_t}{\sigma_\omega} \tag{3.14}$$

where, σ_k and σ_ω are the turbulent Prandtl numbers for k and ω respectively. μ_t is the turbulent viscosity.

3.6.4 *Solver setup*

The turbulence kinetic energy and specific dissipation rate are discretized using a second-order upwind scheme. The pressure is discretized using a second-order scheme and the gradient is calculated using the least-squares cell-based scheme. The pressure-velocity coupling is implemented using the Semi-Implicit Method for Pressure Linked Equations (SIMPLE) scheme.

3.6.5 *Grid and time independence tests*

To assess the grid independence, the profile generated using one of the optimal points (Chan et al., 2018), specifically (60.84, 35.65) at *OR* = 0.10, is utilized. Three different mesh elements are tested as shown in Table 3.2. It is seen that the C_T improves by 1.5% from mesh 1 to 2, and the additional time required does not exceed 2 hours. From mesh 2 to 3, the C_T increases by 0.21%, while the simulation time increases by 2.5 hours. Mesh 2 is therefore chosen for this study to reduce computational effort. For the time independence test, multiple points with different *ORs* are evaluated for up to 15 rotations of the rotor. The total time required for all rotor rotations is approximately 45 minutes. Figure 3.13 illustrates the relationship between the change in C_T and the number of rotor rotations. It is observed that after 13 rotor rotations, the change in C_T becomes less than 0.001. Hence, the C_T is calculated depending on the sum of 13 rotor rotations. The time-averaged C_T for all three blade profiles takes approximately 10 hours to compute.

Table 3.2: Grid independence test

Mesh	No. of grids	C_T	Time (in hr.)
1	55000	0.2354	4.25
2	100000	0.2392	6
3	165000	0.2397	8.5

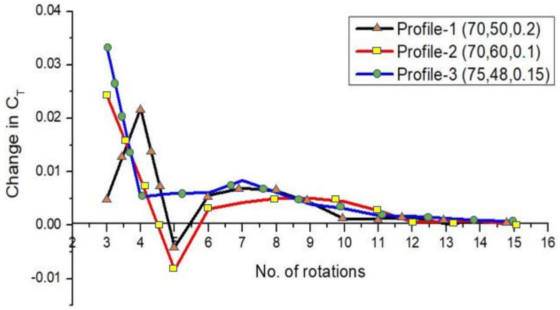

Figure 3.13: Variation of C_T with respect to no. of rotations at different *OR*

3.6.6 Computational model validation

The experimental data obtained by Blackwell et al. (Blackwell et al., 1977) are widely recognized as benchmark data in various numerical studies (Ogawa., 1984; Agrawal et al., 2019). A direct comparison between the present simulation and the experimental data is made in the range of *TSR* from 0.6 to 1 (Figure 3.14). The test model is selected to match the *AR (=1)* of numerical model. To replicate the experimental conditions, the *Re* in the numerical model is adjusted to 4.32 x 10^5. The numerical results are found to be consistent with the experimental data with a maximum percentage deviation of 1.12%.

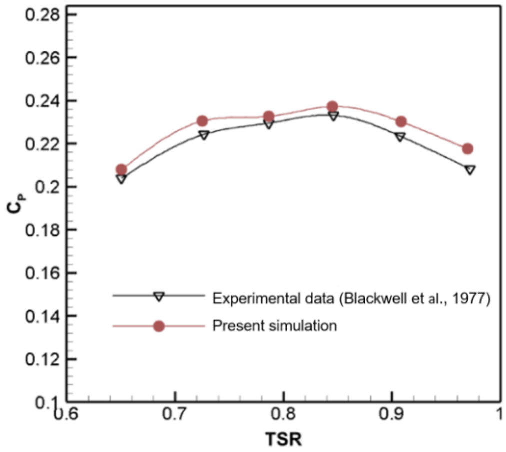

Figure 3.14: Variation of C_P with *TSR*

3.7 Discussion of Computational Results

This section deals with the results obtained from optimizing the *OR* of the blade profile and analyzing the effect of *TSR* on the rotor's performance. The SSM is employed, with commonly used parameters γ, β, and ϵ set to 0.5, 2, and 10^{-4}, respectively. Apart from this, NSGA II application is also seen to have a multiobjective function optimization. The computational analysis is performed on a system with a 3.7 GHz Intel Xeon processor, 16 GB RAM, and Windows 10 Pro operating system (64-bit).

3.7.1 Results of SSM

To ensure a robust solution using the SSM, the process is repeated thrice with different input values. This is necessary because it does not always guarantee the global maximum solution. Table 3.3 presents the results obtained from the three test runs. The test run 3 demonstrates superior C_P among them, and the process is terminated after 25 iterations. The decision variable values for the optimum profile are determined to be (79.63, 33.6301, 7.7), as depicted in Figure 3.15. Consequently, the C_P achieved at this optimal point is the highest for this profile, as shown in Figure 3.16, and reaches a plateau after 25 iterations.

Table 3.3: Results at various input decision variable and the optimum decision variable

Particulars	Test Run-1	Test Run-2	Test Run-3
Input-1	(75,54,0.20)	(70,50,0.10)	(75,48,0.12)
Input-2	(50,58,0.28)	(72,49,0.11)	(70,60,0.15)
Input-3	(60,65,0.10)	(74,48,0.12)	(75,57,0.16)
Input-4	(50,60,0.15)	(60,65,0.25)	(80,65,0.21)
Optimum Profile	(51.07,68.52,9.2)	(74.56,45.7,11.2)	(79.63,33.63,7.7)
C_P	0.263	0.268	0.283

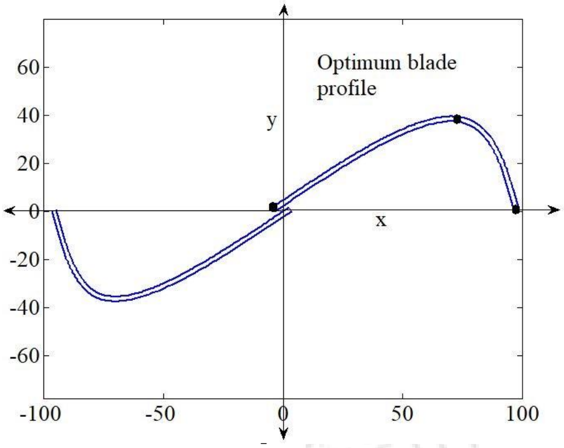

Figure 3.15: Optimized blade profile using SSM

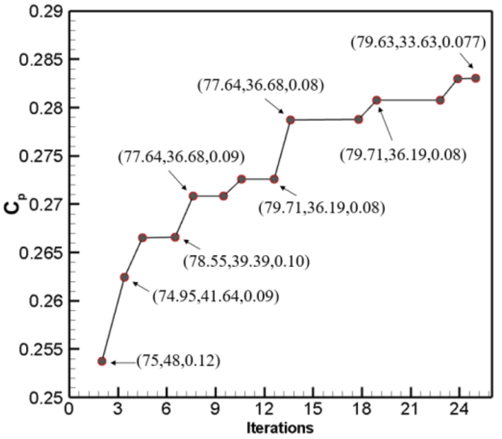

Figure 3.16: C_P with respect to number of iterations

3.7.1.1 Effect of *TSR* and *OR*

Figure 3.17 shows the effect of *TSR* over a range of 0.6-1. A direct comparison in terms of C_P with respect to *TSR* for the optimum spline blade profile and the semicircular counterpart is done. It is noted that the optimum profile performs better throughout the given *TSR* with a C_{Pmax} of 0.283 at *TSR* = 0.8. The *OR* has a significant effect on the rotor performance. However, to ensure the degree of overlap can be used as a design variation, simulations are performed where three different blade geometry were selected. The time averaged C_T values are calculated for these geometric blades within a range of *OR* = 0.05-0.2. It is observed that with an increase of *OR*, the C_T increases and over the time, it decreases as shown in Figure 3.18. However, the maximum *OR* for the maximum C_T is different for all the geometries. Thus, it can be argued that the peak of *OR* for a maximum C_T is different for different blade profiles. Therefore, it can be inferred that the *OR* can be used as a design variable for the Savonius rotor.

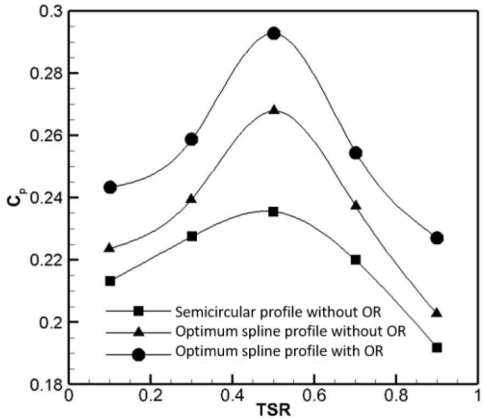

Figure 3.17: Variation of C_P with *TSR*

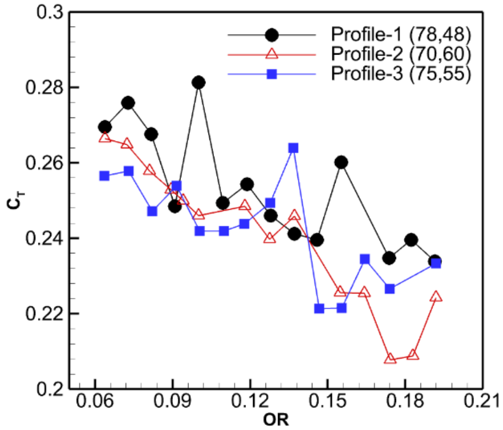

Figure 3.18: Variation of C_T with *OR*

3.7.1.2 Velocity magnitude contours

Figures 3.19 and 3.20 show the velocity contours of the optimal profile and semicircular at *TSR* = 0.8 at α = 0° and 90°. On the concave side of the advancing blade, velocity of the optimal spline blade profile lies between 3 to 6 m/s; while for the semicircular profile, it lies between 1 to 4 m/s at an α = 0° and α = 90°, speed of the semicircular profile is much lower than the optimal profile and covers most of the area. Apart from this, on the convex side of the advancing blade, the velocity magnitude of optimal profile is between 8 to 17 m/s.

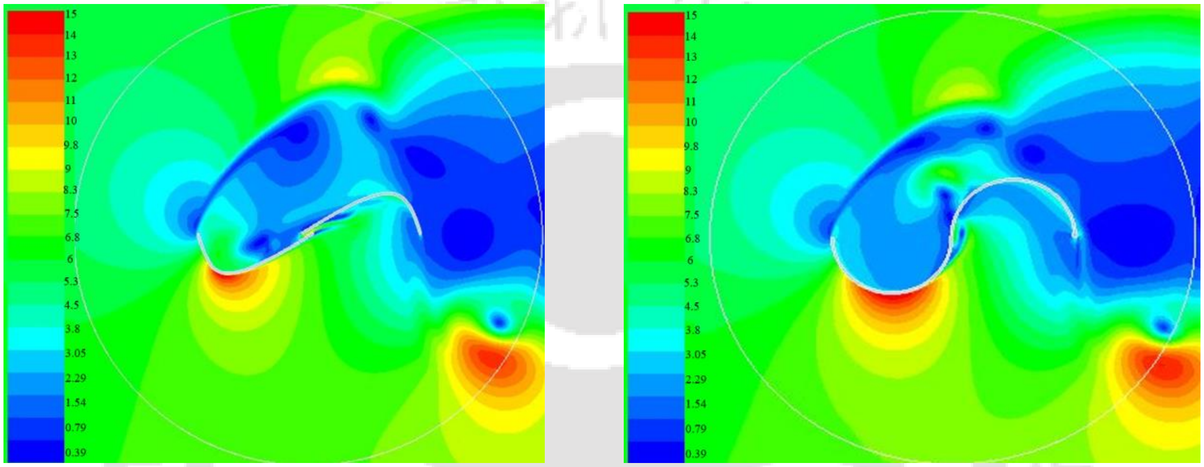

(a) (b)

Figure 3.19: Velocity magnitude of (a) optimum spline and (b) semicircular profiles at $\alpha = 0°$

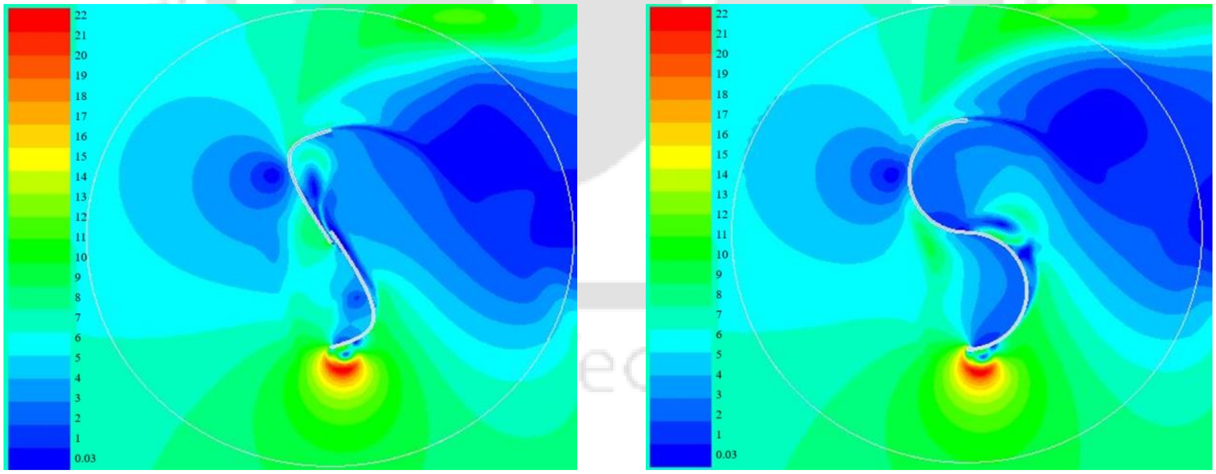

(a) (b)

Figure 3.20: Velocity magnitude of (a) optimum spline and (b) semicircular profiles at $\alpha = 90°$

While for semicircular profile, it lies between 7 to 15 m/s at α = 0° and covers a much larger area of the blade than the new optimal blade at an α = 0° and 90°. Therefore, the advancing blade of the new profile encounters less negative drag. Now, with the returning blade, the magnitude of the velocity on the concave side of the optimized profile is greater than that of the semicircular profile. The velocity magnitude on the convex side is very low as that of semicircular profile, it also ensures that the negative drag on the returning blade is less on the optimized profile. Since the Savonius turbine is a drag-based machine, a less amount of negative drag helps to obtain a higher C_T value, which also improves turbine performance.

3.7.1.3 Total pressure contours

The total pressure contour of optimum and semicircular profiles at *TSR* = 0.8 at $\alpha = 0^{o}$ and 90^{o} are shown in Figures 3.21 and 3.22. Near the advancing blade, the total pressure of the optimum spline and the semicircular profiles lie in the range of 0 - 40 N/m^2 on the concave side, whereas it lies in the range of 40 - 60 N/m^2 on the convex side.

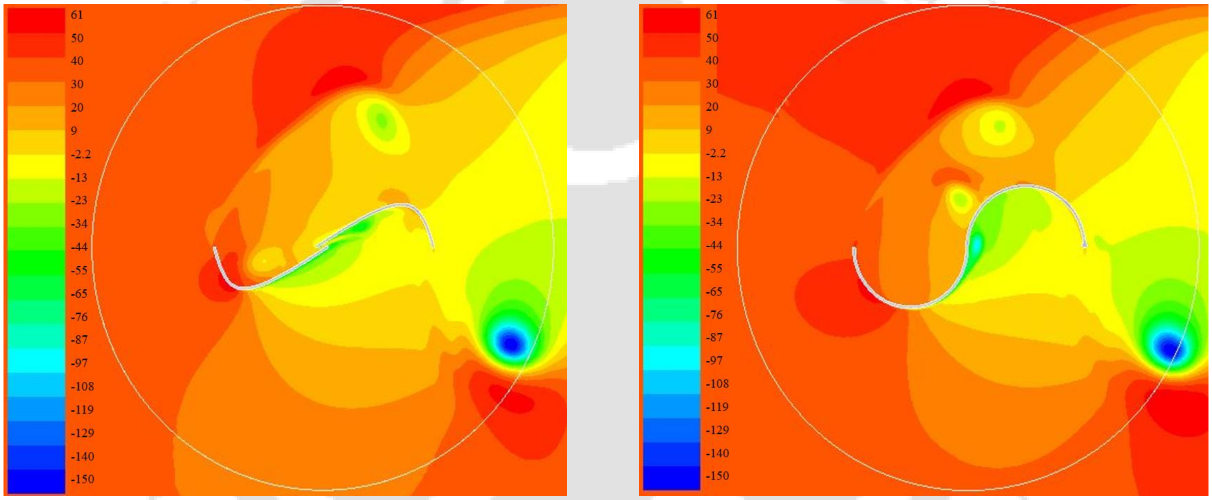

(a) (b)

Figure 3.21: Total pressure contours of (a) optimum spline and (b) semicircular profiles at $\alpha = 0^{\circ}$

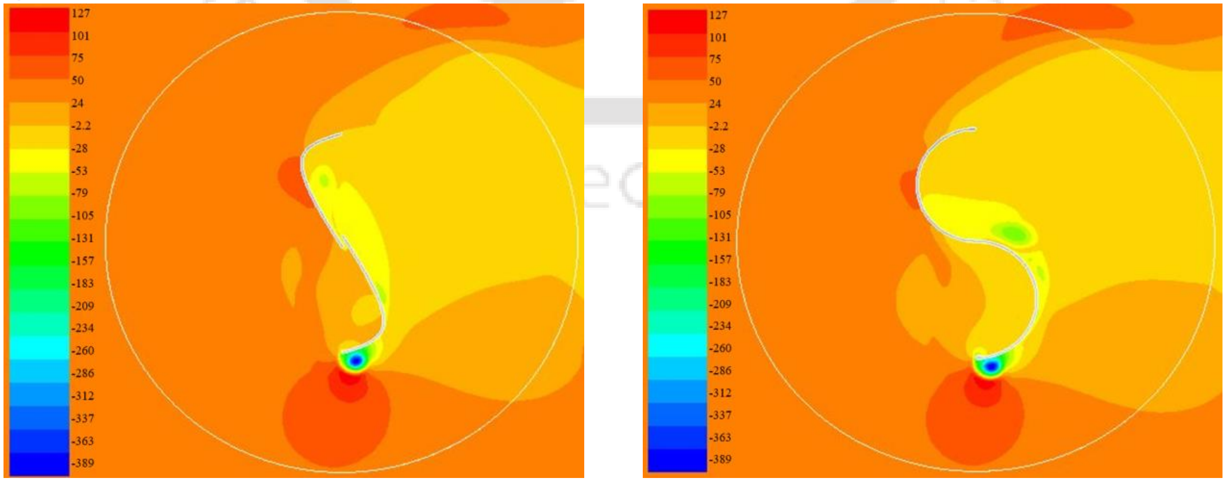

(a) (b)

Figure 3.22: Total pressure contours of (a) optimum spline and (b) semicircular profiles at $\alpha = 90^{\circ}$

In addition, on the returning blade, the pressure on the convex side is greater than the concave side for both the profiles. This is not a favourable condition; however, this pressure difference is low in case of the optimum profile as compared to the semicircular one. This improves the performance of the Savonius rotor blade profile.

3.7.1.4 Turbulent intensity contours

Figures 3.23 and 3.24 show the turbulence of optimum spline and semicircular profiles at TSR = 0.8 at α = 0º and 90º.

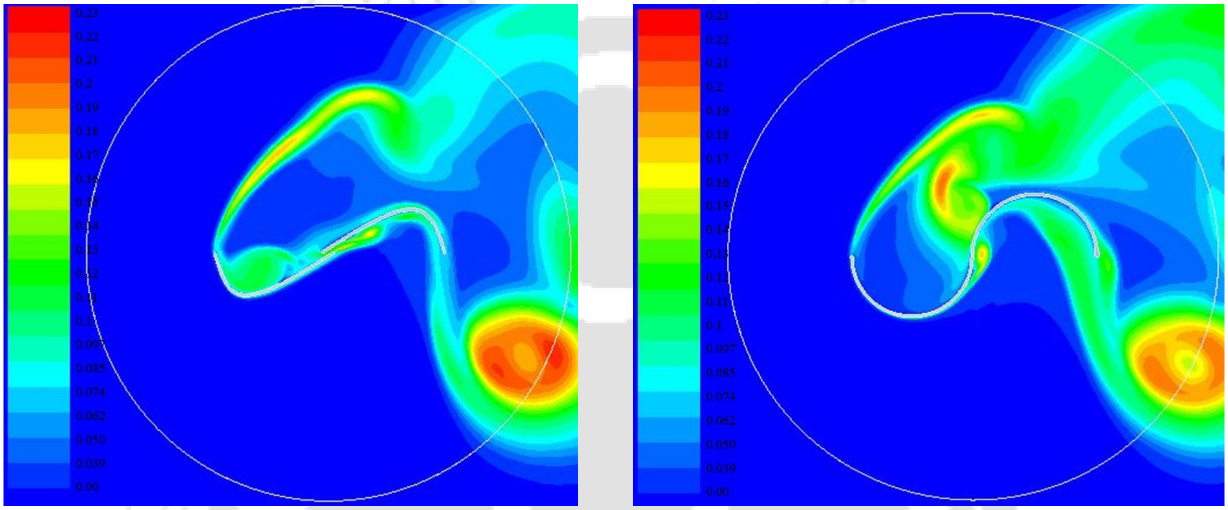

(a) (b)

Figure 3.23: Turbulent intensity contours of (a) optimum spline and (b) semicircular profiles at α = 0º

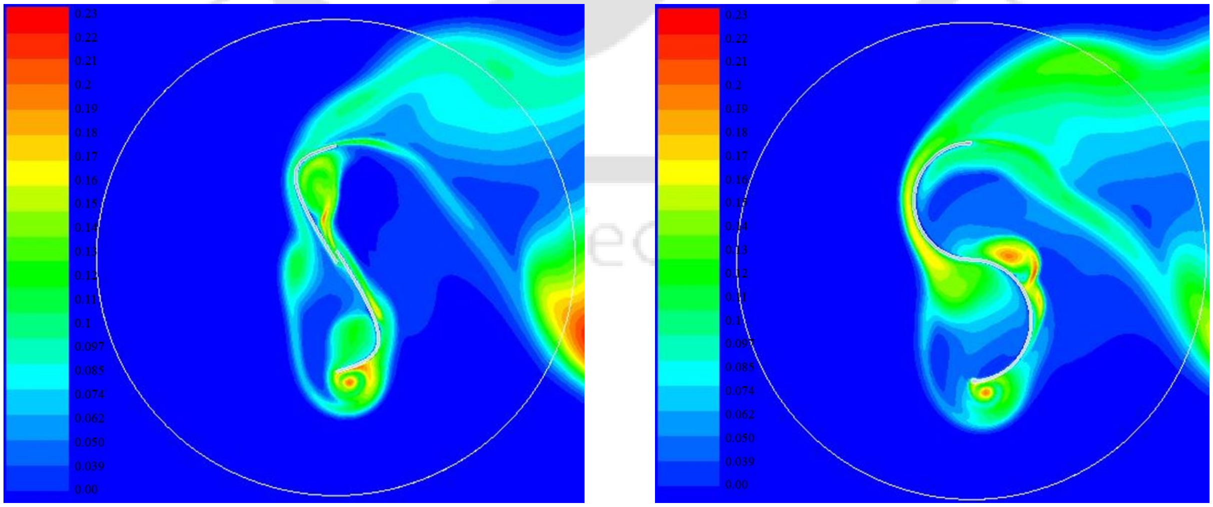

(a) (b)

Figure 3.24: Turbulent intensity contours of (a) optimum spline and (b) semicircular profiles at α = 90º

The magnitude of the turbulence varies from 0 to 0.16 in the optimum spline profile, while in the semicircular profile, this variation lies between 0 and 0.22. It can also be seen that in the semicircular profile, the magnitude of turbulence is found to be higher at the down-stream side and this leads to the formation of vortices and reduces the rotor performance.

3.7.2 Results of NSGA-II

To obtain an optimal solution using NSGA-II, both *OR* and *SG* are negleted and the maximum population generation is set to fifteen. Here x_1, y_1, x_2, y_2, x_3, y_3, *TSR* and *V* are used as design variables and objectives are set to maximize C_P and to minimize *V*. The process is terminated after 30 iterations. Table 3.4 presents the outcome, it can been seen that C_{Pmax} = 0.286 is obtained at V = 9.88 m/s and the lowest C_P = 0.233 is obtained at V = 5.24 m/s. It can been observed that the value of *TSR* is around 0.8 in all the pareto-solutions. Therefore, a constant value of *TSR* is used for further research. Pareto-front solution is shown in Figure 3.25. The C_{Pmax} obtained from NSGA-II is 0.286.

Table 3.4: Results for the optimal solutions of NSGA-II

X_1	X_2	X_3	Y_1	Y_2	Y_3	TSR	*V*	C_p
29.26	31.27	86.99	22.71	13.51	14.19	0.88	9.88	0.286
19.08	43.88	82.67	40.08	49.88	47.18	0.98	9.49	0.274
19.05	47.20	77.94	42.76	42.29	46.03	0.88	9.22	0.265
29.12	57.14	70.86	15.95	26.73	55.85	0.80	8.81	0.251
7.70	50.05	90.88	24.08	42.74	30.17	0.78	8.44	0.248
18.72	43.46	74.97	32.63	65.44	52.15	0.95	8.17	0.246
21.66	63.20	70.57	49.71	55.39	40.59	0.84	7.89	0.245
27.83	67.35	89.88	44.95	45.73	36.42	0.86	7.56	0.245
9.82	68.57	85.85	15.04	55.20	38.4	0.88	7.52	0.242
15.67	43.54	74.83	31.07	14.27	41.34	0.81	7.00	0.239
16.46	46.56	84.63	42.40	63.96	43.63	0.80	6.50	0.238
27.83	61.70	71.15	45.40	55.43	39.32	0.88	5.94	0.234
27.77	53.52	94.44	13.06	60.18	21.05	0.83	5.76	0.234
5.95	46.69	84.63	42.76	68.45	43.63	0.80	5.62	0.234
11.52	44.62	79.54	26.76	64.05	53.00	0.83	5.24	0.233

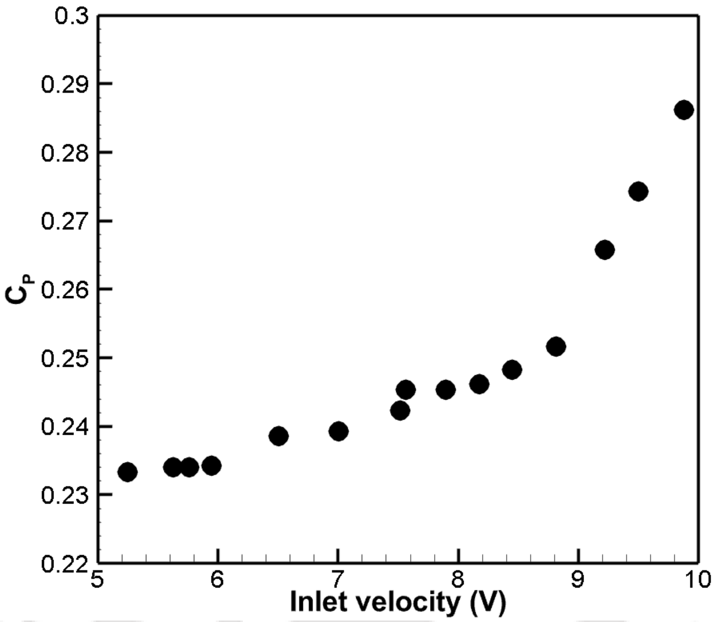

Figure 3.25: Variation of C_P with inlet velocity for NSGA-II

3.8 Summary

This chapter outlines the design of a Savonius rotor blade profile by two different OTs i.e. SSM and NSGA-II, combined with transient 2D CFD simulations. The obtained blade profile is then compared with the conventional semicircular profile at various *TSR* levels to assess its suitability for practical applications. The optimization process involves 25 iterations of the chosen algorithm to arrive at an optimal spline blade profile. The optimized blade profile can be obtained by defining the natural cubic spline using the following points: (-96, 0), (-75.63, -32.63), (4, 0), (-4, 0), (75.63, 32.63), and (96, 0). The C_{Pmax} for the optimal and semicircular profiles are found to be 0.283 and 0.23, respectively. It is noted that the performance of the optimal spline profile is better than the semicircular counterpart in the tested range of *TSR* = 0.6-1. In the simplex search technique, only one variable point is used to define a blade geometry. If more variable points are given to define the blade geometry, a better solution could be expected. Therefore, NSGA-II is applied with three intermediate points, *TSR* and *V* as design variables. It is observed that the C_{Pmax} in case of NSGA-II is 0.286 at a *V* = 9.88 m/s. While in *SSM*, the C_{Pmax} is 0.283 at *V* =7.3 m/s. Thus, it can be concluded that the procedure used in the present work can be used to optimize the blade profiles of a Savonius rotor using different optimization algorithms.

Chapter 4

Creation of a Novel Parabolic Blade Profile and Computational Study

Chapter Outline

4.1 Introductory Remark

Although the previously designed Savonius rotor blade profile by OTs have showcased an enhancement in the C_P, there is always a scope to evolve newer blade profiles. This chapter delves into the design of a new blade profile using a parabolic curve. This type of parabolic profile for the design of blades in a Savonius rotor has not been attempted till date. Thereby, a 2D *CFD* study is performed on the new parabolic blade profile using *ANSYS* Fluent software (ANSYS Inc, 2015). The torque and power coefficients (C_T and C_p) values are studied at different tip speed ratios (*TSRs*) and Reynolds numbers (*Re*). Based on all the above parameters, the performance of the parabolic profile is compared with that of a conventional semicircular profile under similar environment.

4.2 Parabolic Blade Profile Creation

The present parabola can be drawn by following the equation $x^2 = 4ay$ as shown in Figure 4.1. In the present study, only one parabola with focus (F = 0, 0) and the vertex point (O = 0, -2) is chosen arbitrarily to generate the blade profile. However, there may be an infinite number of parabolas that can be optimized by using optimization algorithm. The present work deals with unfolding the potential of a new blade profile for which an arbitrary parabola with section cut angle (θ) is chosen.

The standard parabolic equation with vertex (0, -2) and directrix length (a = 2) is given by the equation (4.1).

$$(x-h)^2 = 4a(y-k) \tag{4.1}$$

Thus, the present parabolic equation can be written as:

$$x^2 = 8y + 16 \tag{4.2}$$

Beside this, line AB can be expressed as

$$y = -\tan\theta \cdot x + l - 2 \tag{4.3}$$

where $l = 0.164D$.

Considering that points A and B meet both the eqns. (4.2) and (4.3), the arc AOB can be expressed as a function of θ, as given by eqn. (4.4).

$$x^2 = 8y + 16\left(\frac{-8\tan\theta - \sqrt{64\tan^2\theta + 1049.6}}{2} < x < \frac{-8\tan\theta + \sqrt{64\tan^2\theta + 1049.6}}{2}\right) \tag{4.4}$$

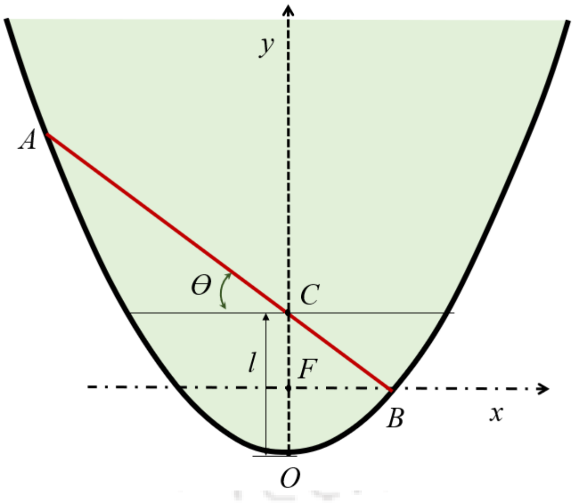

Figure 4.1: The section cut angle (θ) on the parabola

The geometry of the blade profile is generated on SOLIDWORKS. The θ is made by line *AB* with respect to the x-axis on the parabola. Line *AB* dissects the parabola to create an arc *AOB* that gives one-half of the blade profile. Line *AB* intersects the y-axis at point *C* about which θ can be varied and optimized. The length *OC* thus becomes the depth of cut (*l*) on the parabola, and this is 0.164*D* from point *O*. The θ is dependent on *l*, i.e., for each θ, there is a fixed value of *l* to get the required chord length (*L*) of the blade profile. The flow chart adopted to get the optimum profile is shown in Figure 4.2.

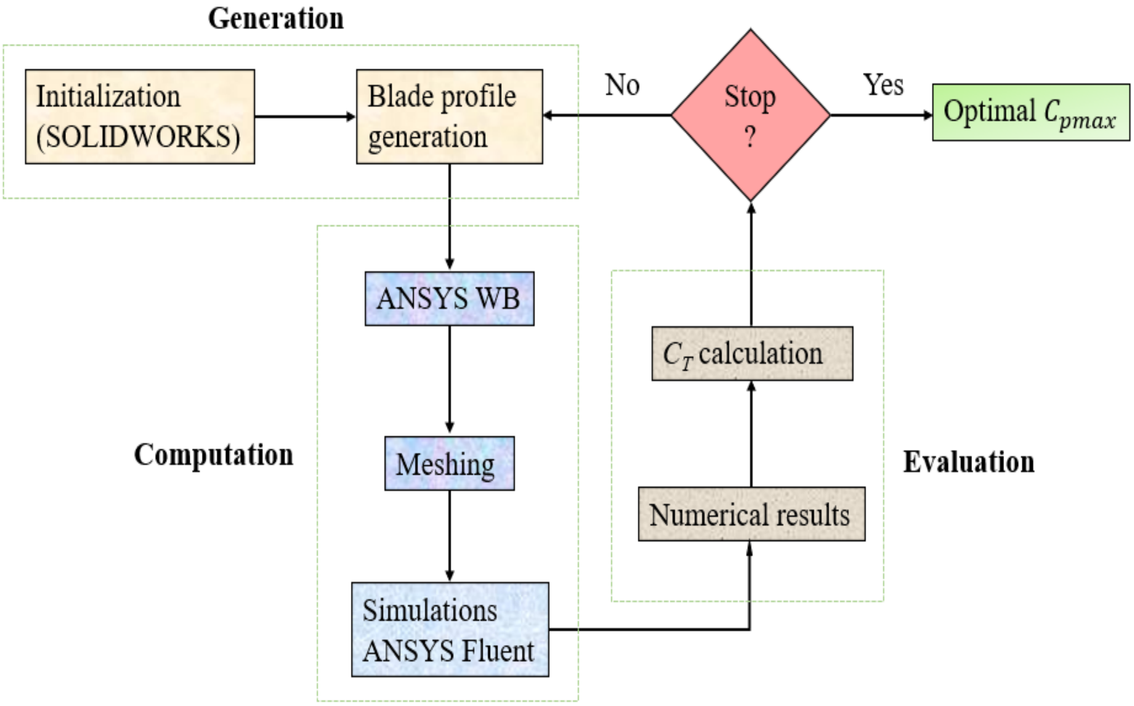

Figure 4.2: The flow chart adopted to get the optimum profile

4.3 Geometric Details

The diameter (*D*) and thickness (*t*) of the blade profile is taken as 200 and 2 mm, respectively. The diameter of the semicircular profile is kept similar to that of the parabolic profile (Figure 4.3). The *OR* is kept at 0.0 for both the profiles (Chan et al., 2018; Agrawal et al., 2019).

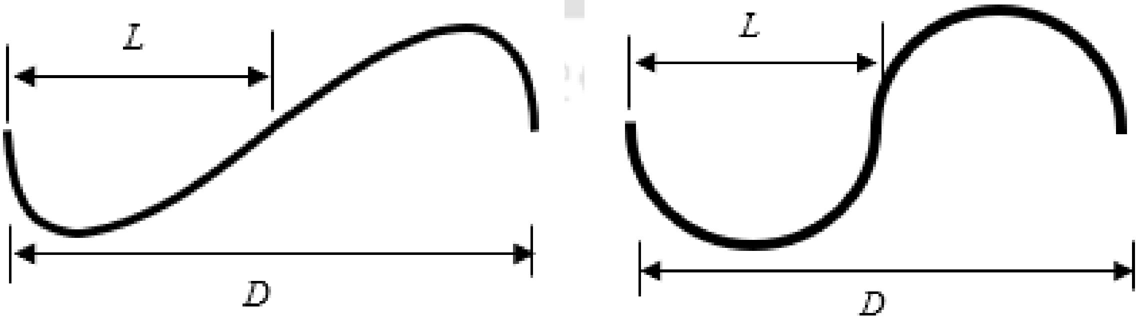

(a) Parabolic profile (b) Semicircular profile

Figure 4.3: Geometry of the test profiles.

4.4 Computational Methodologies

This section deals with the details of the computational domain, meshing, solver setup, grid and time independence tests followed by the validation of the 2D numerical model.

4.4.1 *Computational domain and* ***boundary conditions***

The computational domain (15*D*×22.5*D*) can be categorized as rotational and non-rotational zones. The rotational zone consists of rotor blades that coincide with the origin. The overall diameter of the rotor blade is *D*, and the corresponding rotational zone is 2*D* (Chan et al., 2018; Agrawal et al., 2019). While the non-rotational zone is surrounded by a rectangle (Figure 4.4).

For setting the boundary conditions, the upper and lower walls are equidistant from the center and are found to have symmetrical behavior. Both the walls are at a distance of 7.5*D* from the origin (Figure 4.4) and are named as symmetry (Chan et al., 2018). The vertical left edge (Inlet) is situated at 7.5*D* from the origin, the right vertical edge (Outlet) is situated at 15*D* from the origin as shown in Figure 4.4. The inlet velocity (*V*) of 7.3 m/s is provided in the positive x-axis direction with a maximum turbulence of 1% is given as the boundary condition. The 'pressure outlet' is taken as an output boundary condition with the same amount of turbulence intensity. In the solver setup, the air is taken as the working fluid, and hence the standard atmospheric conditions are provided (Chan et al., 2018; Agrawal et al., 2019).

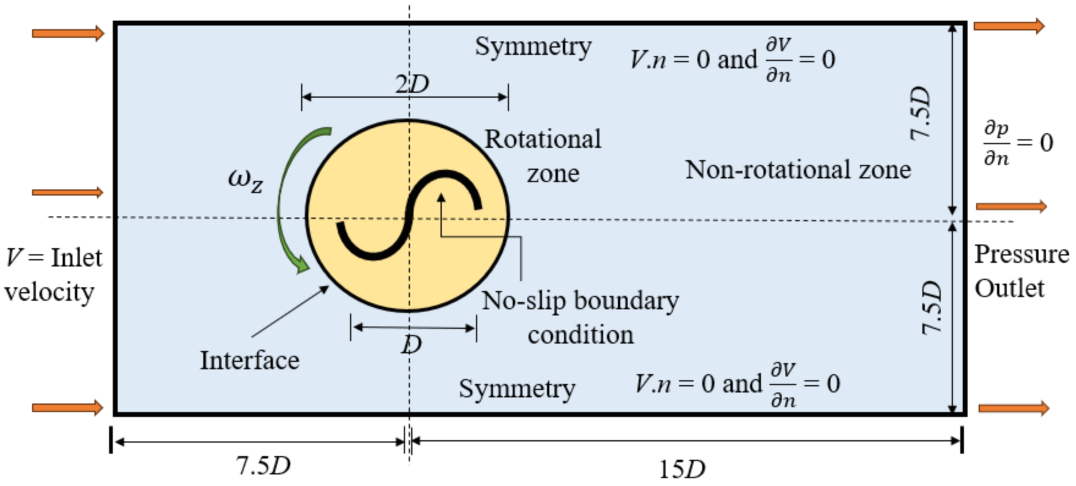

Figure 4.4: Domain and boundary conditions.

4.4.2 *Meshing of the domain*

The meshing of the domain is shown in Figure 4.5. The ANSYS Fluent 20.2 software (ANSYS Inc, 2015) meshing is used to discretize the computational domain. The domain is divided into small control volumes and discretized to solve the Reynolds averaged Navier-Stokes (*RANS*) equations. Due to subsonic flow, equal accuracy can be expected in both the structured and the non-structured meshes (Alakashi and Bambang, 2014). However, the unstructured mesh can be easily made in the case of a complex geometry. In addition, due to the faster generation of grids, the unstructured mesh with tri-elements is used to discretize the rotor domain (Chan et al., 2018; Agrawal et al., 2019), while the outer stator domain is discretized by quadrilateral elements (Shukla et al., 2022). The sliding mesh option is chosen at the 'Int' between the rotational and the non-rotational zones. With a first layer thickness from the wall of 0.05 mm and a growth rate of 1.2, the inflation layer is provided for increased precision around the blade profile perimeter. The maximum number of inflation layers is 10 and the growth rate is 1.2, which can be seen in Figure 4.5. In the numerical model, the value of the dimensionless wall distance $y+$ in the region of the cohesive sublayer is found to be less than unity (Roy and Ducoin, 2016; Shukla et al., 2022).

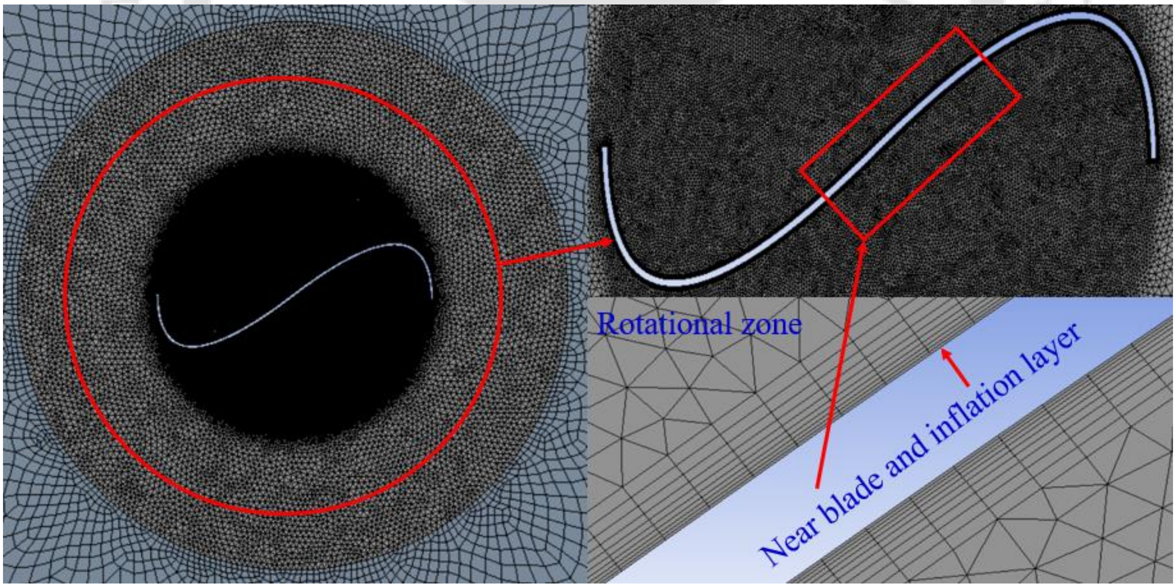

Figure 4.5: Meshing near the rotor

4.4.3 *Turbulence model and solver setup*

In the solver setup, the air is taken as the working fluid, and hence the standard atmospheric conditions are provided. As the flow around the rotor blade is turbulent, it is important to choose a turbulence model accordingly. Previous numerical studies with various turbulence models suggest the use of the SST k-ω turbulence model for its good predictive power (Song et al., 2015; Alom et al., 2021). The *SST* k-ω model is thus chosen to get the average properties of turbulence near the turbine wall region. This model incorporates the feature of calculating the average properties of the flow within and outside the boundary layer. The sliding mesh (reference frame motion) is chosen for all the numerical simulations. The time step size is found based on 1°/step rotation of the rotor blade at $TSR = 0.8$. The timestep size is calculated as $\frac{\pi}{180\omega}$ and found to be 0.0002988577 seconds and the total number of time steps is 1800 for 2D simulations.

Numerical simulations (upon reaching the dynamic steady state) are performed for 5 complete rotations of the rotor. Though the dynamic steady state is reached after the first rotation, still the last rotation is chosen for the study. A maximum of 20 iterations per time step with convergence criterion 10^{-4} (for stopping the solution) is chosen to stop the solution. The conservative and temporal terms are discretized using a second-order upwind scheme. The semi-implicit method for the pressure-linked equation is chosen for the pressure-velocity coupling to increase the stability of the solution.

4.4.4 *Grid and time independence test*

The mesh independence and the time step independence tests performed on the 2D study are shown in Figures 4.6 and 4.7. The number of grid elements varied from 71790 to 203372. While moving from grid elements 71790 to 120849, there is an increase of C_T by 7.1%. This C_T is not changing much (about 0.4%) while moving from grid elements 120849 to 203372. Thus, the number of grid elements of 120849 is chosen for the 2D simulation. Similarly, the time independence test is done to check the temporal stability.

It is seen that the higher the degree/step (1.5°/level and 2°/level), the lower is the average C_T (Table 4.1). This happens due to the flow being not captured properly near the rotor wall. While the step sizes of 0.5°/step and 1°/step are set to capture the flow correctly near the rotor wall, however, the step size of 1°/step is adopted to ease the computational effort (Alom et al., 2016).

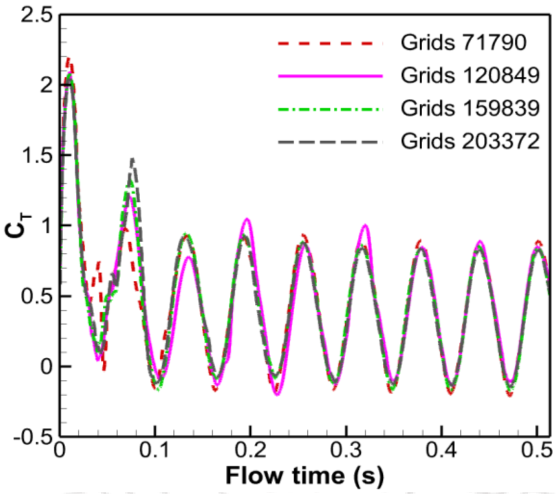

Figure 4.6: Grid independence test

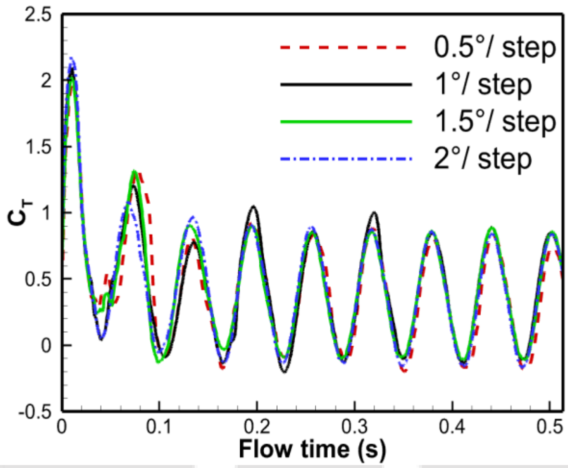

Figure 4.7: Time independence test

Table 4.1: Averaged C_T at different degrees of rotation

Rotation (^{o})	C_T
0.5°	0.3882
1°	0.3991
1.5°	0.3712
2°	0.35

4.4.5 *Computational model validation*

The results of the numerical simulation obtained in this study are validated with the reported work of Alom et al. (2016) as depicted in Figure 4.8. The present test model is selected in such a way that it has the same *AR* (= 1.0) as that of the reported numerical model. Reynold's number considered in the validation study is taken as 0.89 x 10^5 to replicate the published work (Alom et al., 2016). The numerical results are found to be consistent with published data (Figure 4.8). The maximum error between the present study and those of the previous study is 1.8%.

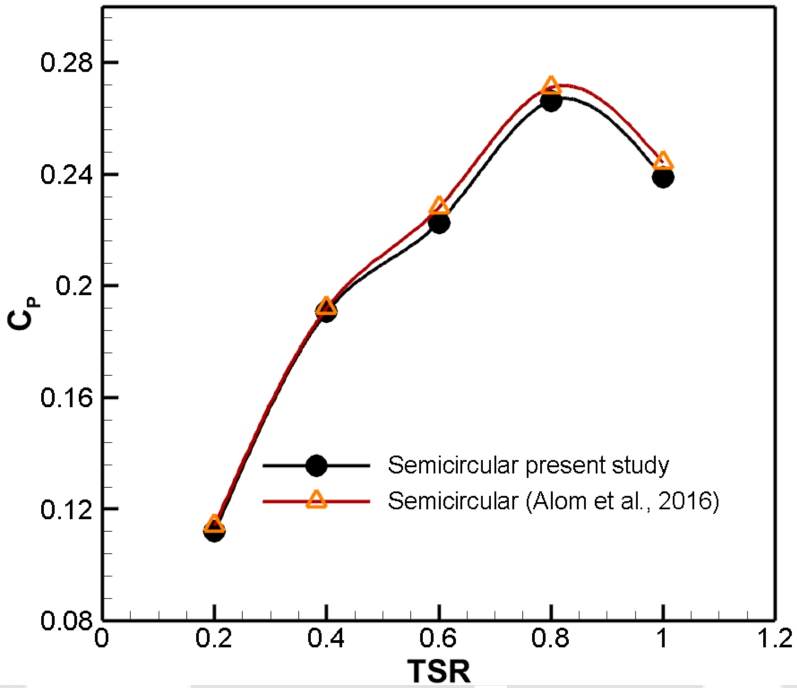

Figure 4.8: Variation of C_p with *TSR*.

4.5 Discussion of Computational Results

In this section, results of the new parabolic profile at different θ are reported. Results of the semicircular profile are also projected for a direct comparison. Thereafter, for the optimum profile, the effect of *Re* and *TSR* are studied. This is followed by velocity magnitude, total pressure magnitude, and turbulence intensity contours.

4.5.1 *Selection of the optimum parabolic blade profile*

A series of 2D unsteady numerical simulations are performed to understand the aerodynamics of a parabolic profile to arrive at the optimum profile by C_T and C_p analyses. Thus, eight different profiles are generated at different θ (ranges from 27.5° to 45°). The variation of C_T with respect to the angle of attack (α) of the parabolic profiles is shown in Figure 4.9. The *TSR* is kept 0.8 for the selection of optimum blade profile (Alom et al., 2016; Chan et al., 2018). The parabolic profile at θ=32.5° shows the maximum C_T as compared to other values of θ besides the semicircular profile. Therefore, a direct comparison (in terms of C_P) of the parabolic profile for various θ is shown in Figure 4.10. The C_P of the parabolic profile at θ

$=32.5^{\circ}$ is found to be the maximum amongst all. This parabolic profile with $\theta = 32.5^{\circ}$ is chosen for further analysis.

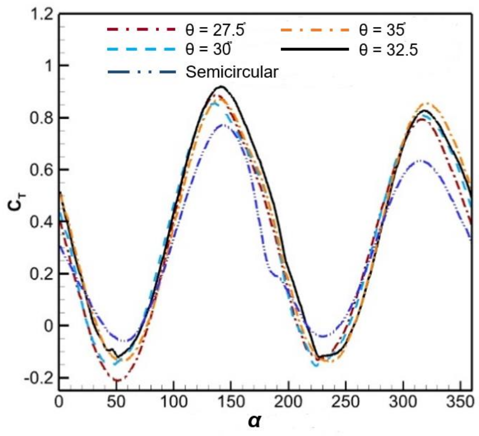

Figure 4.9: Variation of C_T with α

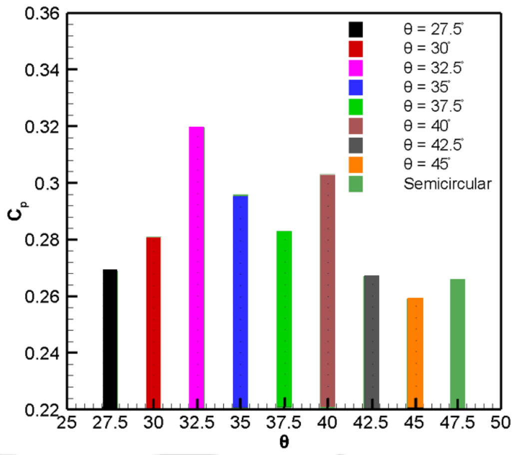

Figure 4.10: Variation of C_P with θ

4.5.2 *Effect of TSR*

The effect of *TSR* on the performance of the optimum parabolic profile ($\theta = 32.5^{\circ}$) is studied in terms of C_T and C_P at an inlet velocity of 6.7 m/s (Figures 4.11 and 4.12). The results of the semicircular profile are also shown for a direct comparison. The rotor speed (u) is found to be decreasing with the increase of load, and thereby C_T decreases with the increase of *TSR* (Figure 4.11). On the other hand, C_P increases up to TSR=0.8 and then decreases, indicating the optimum *TSR* to be 0.8. The parabolic profile shows a C_{Pmax} of 0.319 at $TSR = 0.8$, while the semicircular profile shows the C_{Pmax} of 0.266 at the same *TSR* (Figure 4.12). Thus, the parabolic profile provides an improvement of C_P by 20% over the semicircular profile. Hence, $TSR = 0.8$ is taken for further analysis.

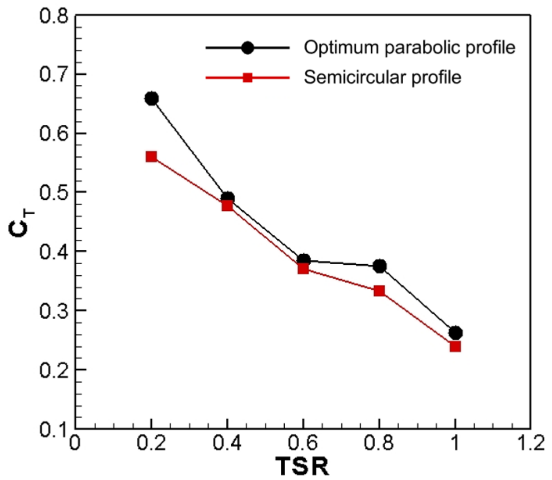

Figure 4.11: Variation of C_T with *TSR*

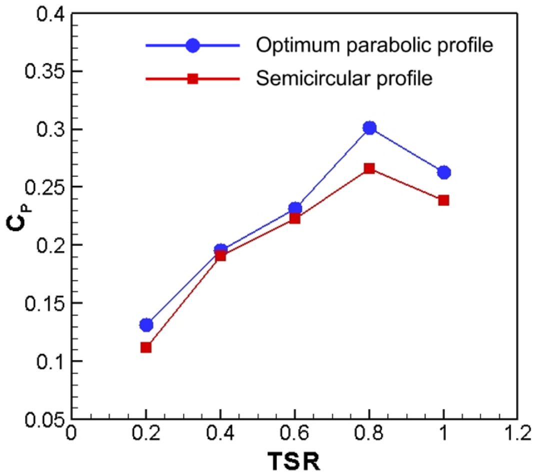

Figure 4.12: Variation of C_P with *TSR*

4.5.3 *Effect of Reynolds number* (*Re*)

The existing literature suggests that the C_P of a conventional Savonius rotor usually increases with rise in Re (Kamoji et al.,20013; Alom et al., 2018). In view of this, the Re study is carried out for both parabolic and semicircular profiles to determine the approximate optimal Re for practical applications. The simulations are conducted at $TSR = 0.80$. The C_T and C_P go on increasing up to an optimum value and then decreases as shown in Fig. 4.13. The average C_T of the semicircular blade profile is found to be 0.37 at $Re = 8.6 \times 10^4$; while the parabolic blade profile shows an average C_T of 0.4 at $Re = 10 \times 10^4$ as shown in Fig. 4.13(a). The parabolic profile shows C_{Tmax} of 1.11 and C_{Tmin} of -0.24 at $Re = 10 \times 10^4$. Moreover, the parabolic profile reveals a C_{Pmax} of 0.35 against the semicircular counterpart with a C_{Pmax} of 0.3 as shown in Fig. 4.13(b). It can also be inferred here that for each design there are different optimum Re. The results suggest that the parabolic blade profile reaches the optimum value of C_P at higher Re, while the semicircular profile reaches the optimum value comparatively at lower Re. The optimum C_P for the semicircular profile is at $Re = 8.6 \times 10^4$, while the parabolic profile shows an optimum C_P at $Re = 10 \times 10^4$. It can therefore be said that different blade profiles perform differently at the identical Re. It is evident that the optimum C_T and C_P are different for both the profiles.

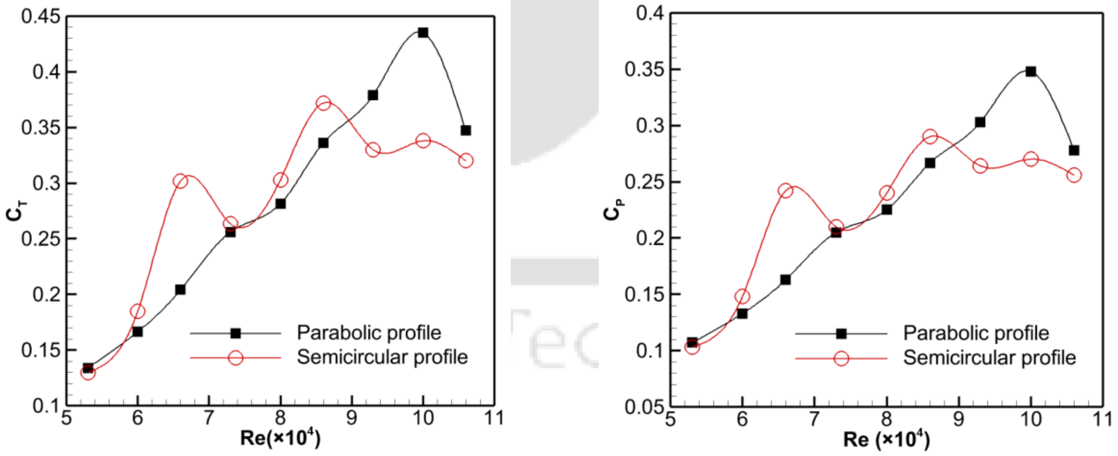

a) C_T vs Re

b) C_P vs Re

Figure 4.13: Performance characteristics curves (a) C_T vs Re, and (b) C_P vs Re

4.6 Contours Analysis

From the visualization of total pressure, and turbulent intensity contours, an attempt has been made to draw some meaningful inferences in this subsection.

4.6.1 *Total pressure contours*

The total pressure contours of the parabolic and semicircular profiles are shown in Figures 4.13 and 4.14. The total pressure of the advancing side of the parabolic profile ranges between 21 and 56 N/m^2, while the total pressure of the advancing side of the semicircular profile lies between 7 and 45 N/m^2. The low-pressure region forming the recirculation behind the advancing side of the parabolic profile is lower than the semicircular profile. Moreover, the high-pressure region on the convex side of the returning side of the parabolic profile is smaller than the semicircular profile thereby improving the net torque. As the semicircular profile is characterized by a higher curvature, the flow separation is likely to occur earlier than in the parabolic profile. For the parabolic profile, the adverse pressure gradient is much lower than the semicircular profile. The parabolic profile thus has a higher C_D and C_P.

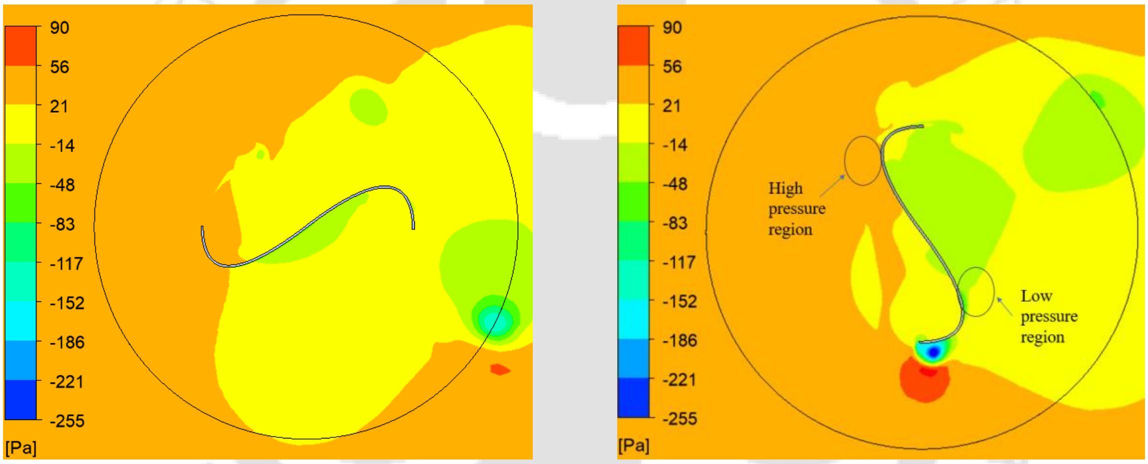

(a) $\alpha = 0^o$ (b) $\alpha = 90^o$

Figure 4.13: Total pressure contours of the parabolic profiles at $\alpha = 0^o$ and 90^o

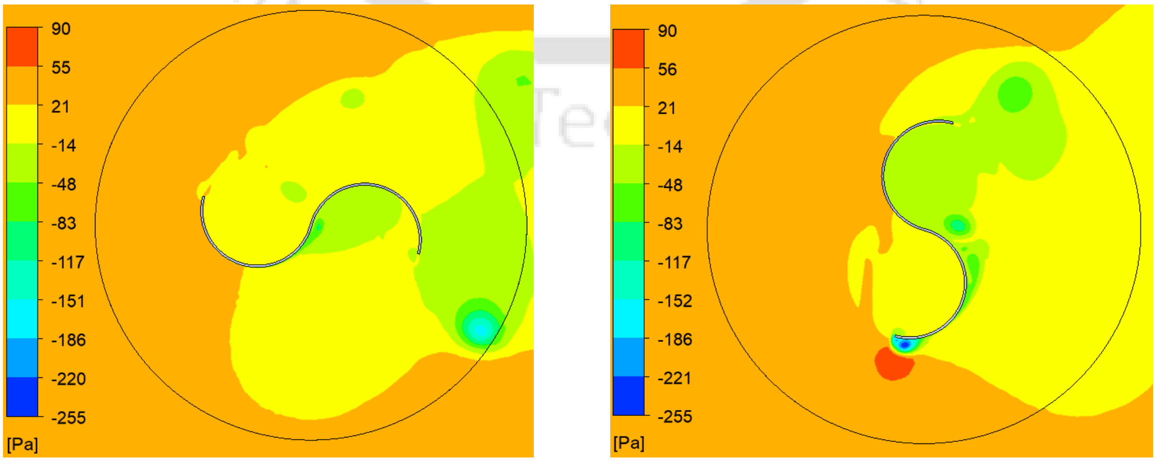

(a) $\alpha = 0^o$ (b) $\alpha = 90^o$

Figure 4.14: The total pressure contours of the semicircular profile at $\alpha = 0^o$ and 90^o

4.6.2 *Turbulence intensity contours*

Turbulence intensity is the property of turbulence that measures the degree of turbulence in the flow. The contours of turbulence intensity for the parabolic and semicircular profiles are shown in Figures 4.15 and 4.16. The turbulence intensity is found to be low near the blade region in the parabolic profile ranging from 0.03 to 0.12%, however, it is found to range from 0.06 to 0.18% for the semicircular profile. As the magnitude of intensity is much lower in the parabolic profile, the vortex formation downstream of the profile is reduced. Further, a smoother flow field behind the returning side of the parabolic profile is observed as compared to its semicircular counterpart. This causes a higher C_P for the parabolic profile.

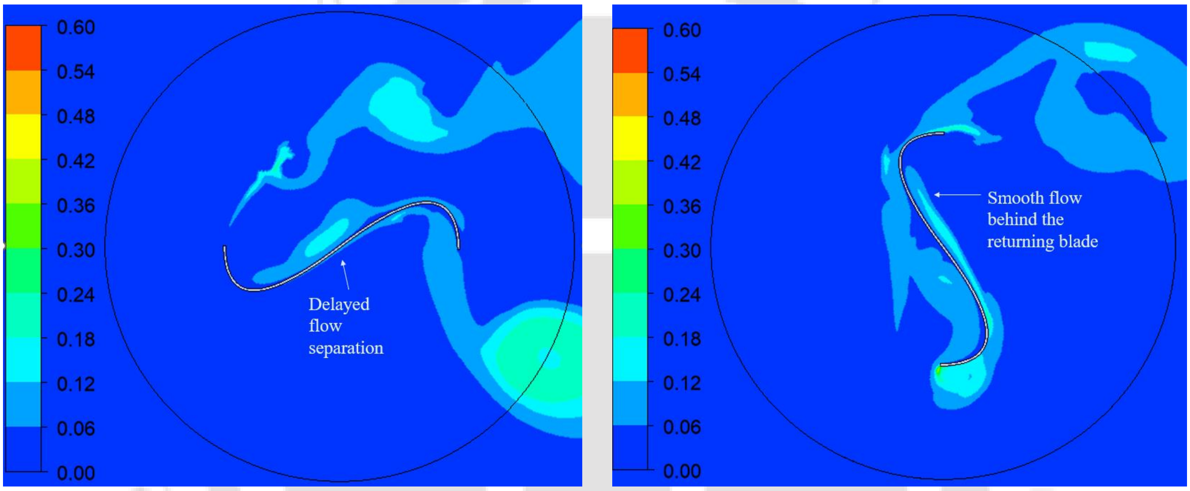

(a) $\alpha = 0^\circ$ (b) $\alpha = 90^\circ$

Figure 4.15: Turbulence intensity contours of the parabolic profile at $\alpha = 0^\circ$ and 90°

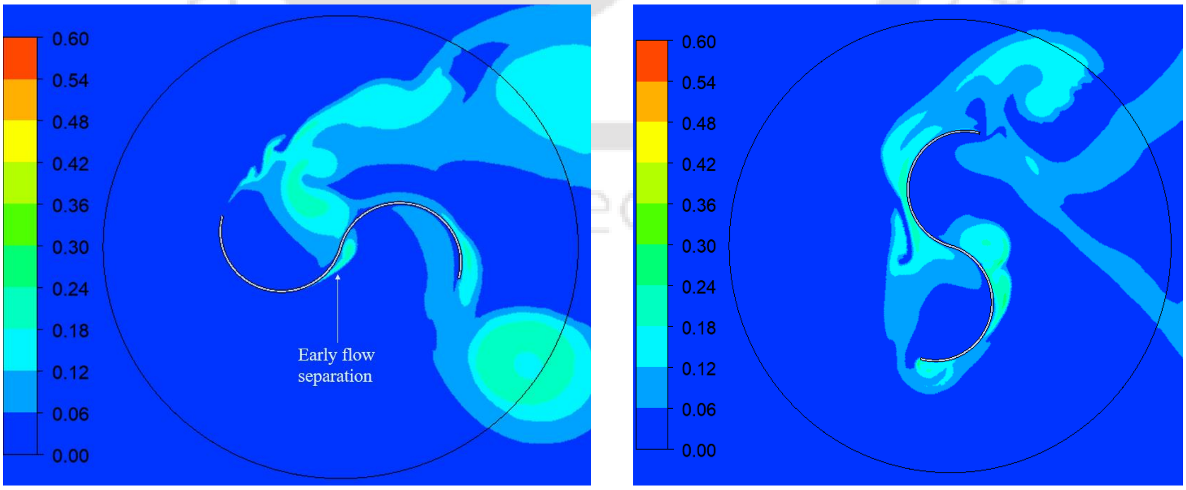

(a) $\alpha = 0^\circ$ (b) $\alpha = 90^\circ$

Figure 4.16: Turbulence intensity contours of the semicircular profile at $\alpha = 0^\circ$ and 90°

4.7 Summary

A series of 2D unsteady numerical simulations are carried out to develop a new parabolic blade profile at different θ using SST k-ω turbulence model. The results obtained in the present study show a maximum performance of the parabolic profile at θ = 32.5°. The parabolic blade profile obtained is then compared with the conventional semicircular counterpart. Moreover, the parabolic profile shows higher C_P values than the semicircular profile throughout the tested range of *TSR*. On the other hand, *TSR* = 0.8 has shown the potential to harness more power than the other *TSRs*. As the parabolic profile is characterized by a lower curvature, the flow separation on this profile is likely to get delayed as compared to its semicircular counterpart. This enhances the pressure recovery thereby reducing the negative torque and improving the performance of the rotor.

The effect of the *Re* study suggests that with the increase of *Re,* the C_p also increases. The newly developed parabolic profile is found to have a C_{pmax} of 0.35 at a Re = $10\text{x}10^4$, while for the semicircular profile, it is 0.3 at Re = $8.6\text{x}10^4$. Moreover, it is observed that the optimum *Re* is different for both tested blade profiles. It is seen that the parabolic blade profile reaches a C_{pmax} at higher *Re* as compared to the semicircular counterpart.

Chapter 5

Lift and Drag Analyses

Chapter Outline

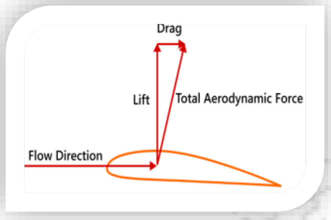

5.1 Introductory Remark

The ultimate intention of this study is to examine the aerodynamic force exerted on the novel parabolic blade profile of the rotor, specifically focusing on its amplitudes and points of application of C_D and C_L relative to the axis of rotation. The goal is to elucidate the factors contributing to the enhanced performance of this new parabolic-bladed design compared to the conventional semicircular-bladed design. The study determines the range of angle of attack (α) where both the amplitude and the points of application of C_D and C_L increase. The evaluation of C_D and C_L is conducted across a complete turbine rotation (α = 0–360°) at *TSR* of 0.8. In order to enhance the design of the Savonius rotor, it's essential to thoroughly investigate both the drag and lift characteristics, despite the rotor primarily functioning as a drag-based wind turbine. Hence this chapter deals with the aerodynamics of the developed blade profile. Figure 5.1 represents the forces acting on the Savonius blade profile.

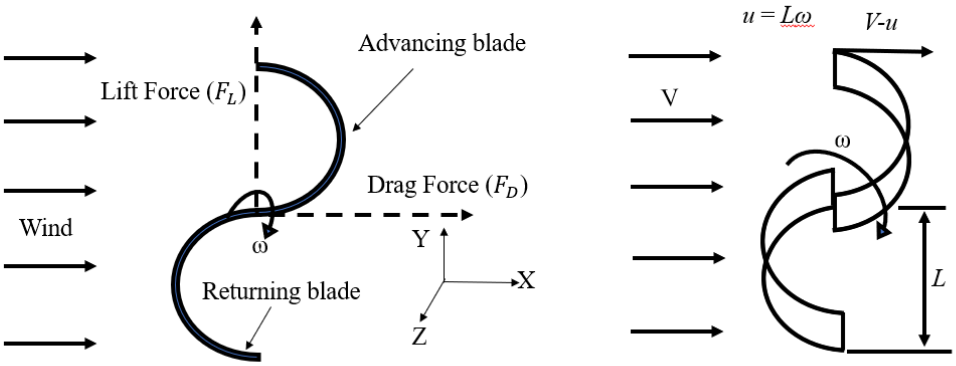

Figure 5.1: The forces acting on the Savonius blade profile

5.2 Geometric Details of the Tested Profiles

The semicircular blade profile with identical diameter (D = 200 mm) and thickness (t = 2 mm) as that of the parabolic profile and the blade profile developed through optimization technique are selected for the analysis. The schematic views of the tested blade profiles are shown in Figure 5.2. The *OR* for both profiles is consistently maintained at 0.0 (Chan et al., 2018).

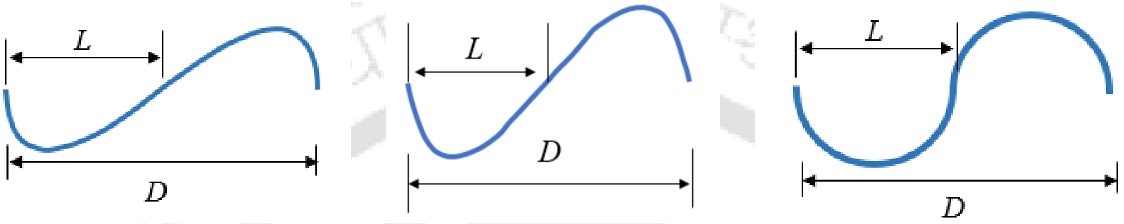

(a) Parabolic profile (b) Optimized profile (c) Semicircular profile

Figure 5.2: 2D view of the tested blade profiles

5.3 Computational Model Validation

The SST k-ω turbulence model is adopted to conduct the 2D unsteady simulations for the current study at an inlet velocity of 7.3 m/s. The consequences of present 2D unsteady simulations are compared with existing data of Roy and Ducoin (2016). They performed the simulation at $R_e = 1.23\text{x}10^5$ for the conventional semicircular profile as shown in Figure 5.3 and Figure 5.4. The investigation is accomplished at TSR = 0.6 as well to validate the results of Roy and Ducoin (2016). The average C_D for the entire rotor replacement is found to be almost identical. The C_{Davg} is found to be 1.19 in the present investigation.

The showcase of instantaneous C_L values for a complete revolution is shown in Figure 5.4. It is observed that the semicircular profile used in the present study shows the $C_{L\text{avg}}$ of 1.06 as compared to the $C_{L\text{avg}}$ of 0.85 as reported by Roy and Ducoin. Thus, the optimized profile shows a little over prediction because of 2D simulations, and this could be overcome if 3D simulations are conducted.

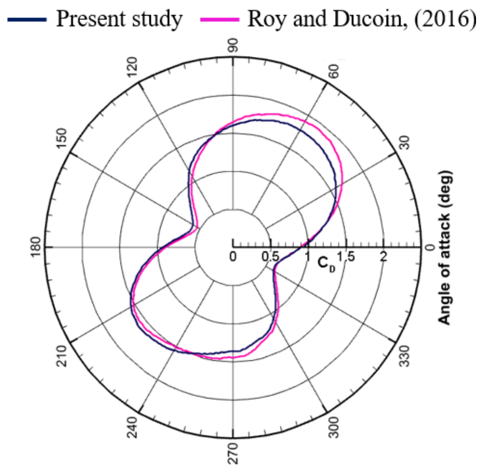

Figure 5.3: C_D of the semicircular profile

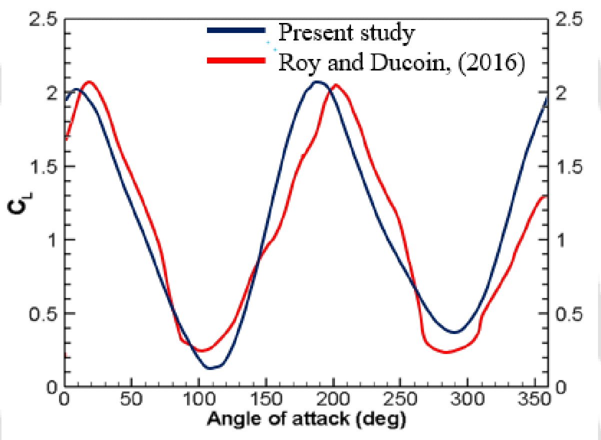

Figure 5.4: C_L of the semicircular profile

5.4 Analysis of the Optimized Spline Profile

The 2D unsteady simulations are performed for an optimized spline blade profile and for a conventional semicircular blade profile. Simulations are accomplished for optimized profile and semicircular profile under similar circumstances. Figures 5.5 and 5.6 show a deviation of C_D and C_L, respectively for both the profiles. The C_{Dmax} for the optimized profile is found to be 1.91 at $\alpha = 54°$ and the C_{Dmin} of the same profile is 0.45 at $\alpha = 147°$. While the semicircular profile shows C_{Dmax} of 1.78 at $\alpha = 60°$, and the C_{Dmin} of 0.60 at $\alpha = 154°$ and 334°. Thus, the optimized profile shows an increment in C_{Dmax} of around 7.3%. On the other hand, the C_{Lmax} of the optimized spline profile is found to be 2.11 at $\alpha = 53°$, while the C_{Lmax} of semicircular profile is seen to be 2.13, demonstrating the inferiority of the optimized spline profile. The optimized profile thus has demonstrated its improved performance in terms of C_{Dmax} as compared to the conventional semicircular profile.

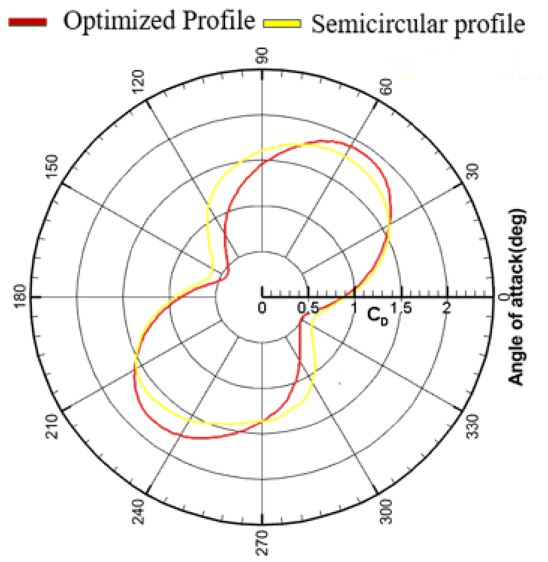

Figure 5.5: C_D of the optimized spline and semicircular profile at *TSR* = 0.8

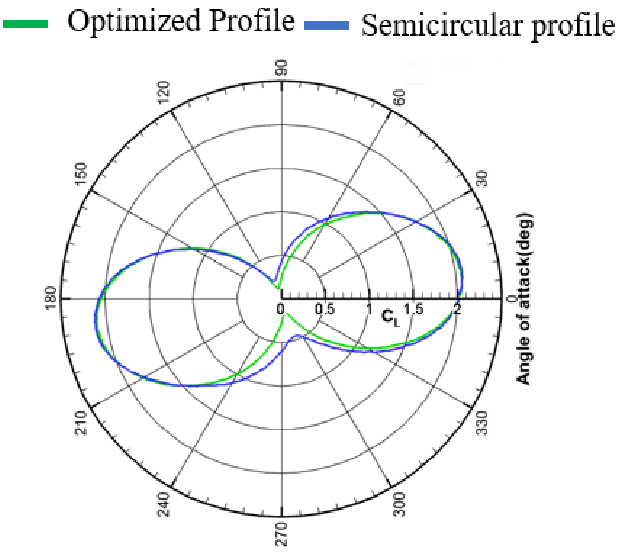

Figure 5.6: C_L of the optimized spline and semicircular profile at *TSR* = 0.8

5.5 Analysis of the Parabolic Profile

A notable improvement in the C_D values is observed throughout the entire rotational cycle of the new parabolic design. This aerodynamic profile has the similarity to aircraft wings which therefore gives the primary advantage of this new parabolic design over the semicircular design. In the parabolic design, the C_D increases up to $\alpha = 45°$ and then decreases to a minimum at α = 150° followed by an increment up to α = 220°. While the C_L increases up to $\alpha = 20°$, and then decreases to a minimum at α = 120°, followed by an increase up to α = 200°. Conversely, for the semicircular design, the C_D increases to a maximum at $\alpha = 50°$, followed by a decrease till it reaches a minimum at $\alpha = 150°$ (refer Figure 5.7). At these angles, the higher curvature of the parabolic design significantly increases the pressure gradient on the suction side. This leads to a vertical orientation of the normal pressure and consequently an increase in lift. Hence, the suction side of the advancing blade acts as the primary surface for the lift generation of parabolic design. The Savonius rotors with other types of blade profiles have shown similar observations (Irabu and Roy, 2011; Roy and Ducoin, 2016). For the parabolic profile, the C_{Dmax} is found to be 2.34 at $\alpha = 45^{o}$ and C_{Dmin} of 0.45 at $\alpha = 90^{o}$; while for the semicircular profile, the C_{Dmax} is found to be 1.98 at $\alpha = 182^{o}$ and C_{Dmin} of 0.3 at $\alpha = 150^{o}$ and 270°. Thus, the parabolic profile shows an increment of C_{Dmax} by 18.18% against the semicircular profile. On the other hand, the C_{Lmax} for the parabolic and semicircular profiles are found to be 2.45 (at $\alpha = 18^{o}$) and 2.13 (at $\alpha = 13^{o}$)

respectively as shown in Figure 5.8. This analysis demonstrates an improved performance of the parabolic profile against the semicircular profile in terms of C_D and C_L.

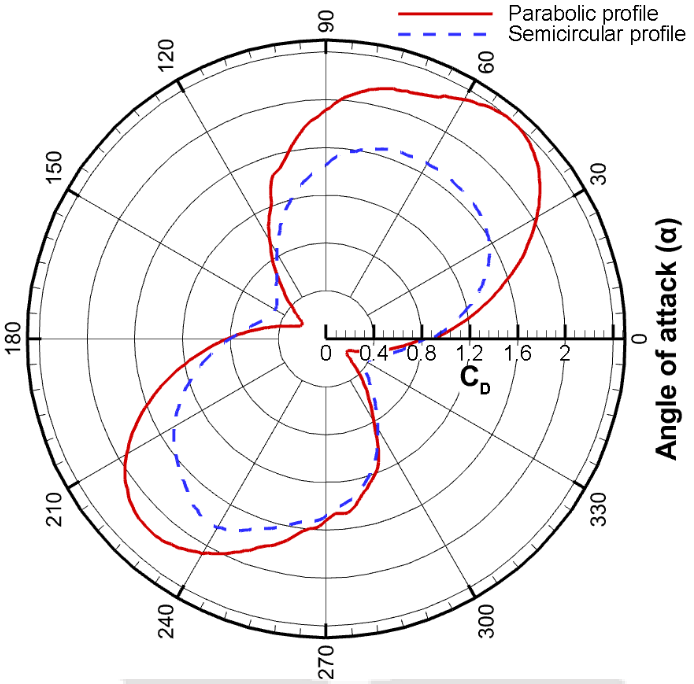

Figure 5.7: C_D of the parabolic and semicircular profile

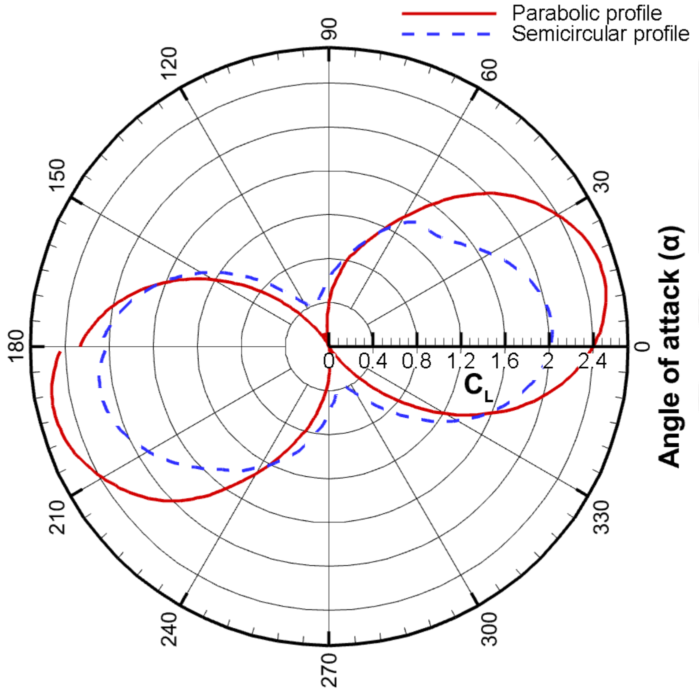

Figure 5.8: C_L of the parabolic and semicircular profile

This happens due to fact that the parabolic profile comprises of an almost straight trailing edge (TE) and a leading edge (LE) having more curvature compared to the semicircular profile, mainly induces variations in pressure drag. During the initial quarter of the rotational cycle ($\alpha < 40^o$), the advancing blade of the parabolic profile experiences a higher magnitude of pressure drag compared to the semicircular profile. Additionally, the TE of the blades contributes positively by enhancing the rotor's moment. Moreover, between $\alpha = 220^o - 260^o$, the wind flow impacting on the advancing blade is more concentrated towards the LE due to the increased curvature of the parabolic profile.

5.5.1 Influence of *Re* on aerodynamic coefficients

As the Savonius rotors are drag-based devices, the study of aerodynamic coefficients (C_D, C_L) of the blade profile is crucial. In this section, an attempt has been made to examine the C_D and C_L exerted on the novel parabolic blade profile. Results are also generated for the semicircular blade profile for a direct comparison. The evaluation of C_D and C_L is conducted across a complete turbine rotation (α = 0–360°) at *TSR* of 0.8. The analyses of C_D and C_L determine the range of α where the amplitude provides the understanding of gaining the optimum C_P.

5.5.1.1 Drag coefficient (C_D)

The geometry of novel parabolic profile is characterized by a nearly straight trailing edge (TE) and a leading edge (LE) with a greater curvature than the semicircular profile, and this primarily induces a variation in pressure drag. During the initial quarter of the rotational cycle ($\alpha < 40°$), the advancing side of the parabolic profile experiences a higher magnitude of pressure drag compared to the semicircular-bladed profile. Similar findings of Savonius rotors with other types of blade profiles have also been observed in the past (Irabu and Roy, 2011; Roy and Ducoin, 2016). Additionally, the straight TE of the parabolic blade profile contributes positively by enhancing the rotor's moment.

Figure 5.9 presents the polar representation of C_D for both the profiles over the tested range of *Re*. The polar representations show the actual variation of C_D over a complete 360°rotation of the rotor with an increment of 1°. For a given *Re*, the C_D increases with respect to its angular position and reaches a maximum at around $\alpha = 40^\circ$-55° in the first quarter of rotation. Likewise, the C_D decreases to a minimum value in the second quarter at around $\alpha = 150^\circ$-155°. At about $\alpha = 50^\circ$ and 220°, the wind incident on the advancing blade profile is more concentrated towards the LE due to parabolic profile's increasing curvature. Similar behaviour is seen in the third and fourth quarters of the complete rotation. This pattern is observed for all the tested range of *Re*. The $C_{D\ max}$ and $C_{D\ min}$ obtained at various *Re* is depicted in Table 5.1. It is observed that with an increase in *Re*, there is an increase in C_D values, and it reaches a peak value (optimum) for the parabolic blade profile and then it starts decreasing beyond an inversion point. It can be noted that the C_{Dmax} and $C_{D\ min}$ obtained is lower for both the profiles at the lower *Re* (Fig. 5.9a and 5.9b). The C_{Dmax} and $C_{D\ min}$ increase with the increase of *Re* for both the blade profiles and reach the optimum value at different *Re*. It can therefore be inferred that the optimum *Re* value to produce the C_{Dmax} is different for both the profiles. The semicircular profile has showcased the maximum performance at $Re = 6.6 \times 10^4$ as shown in Fig. 5.9c. However, the parabolic profile shows an improved performance in terms of C_D (Fig. 5.9d through 5.9i) in the tested range of *Re* except $Re = 6.6 \times 10^4$. Thus, it is noted that the semicircular profile performs better at the lower *Re*. As the C_{Dmax} obtained corresponding to the optimum *Re* is found to be different. The complete data of C_D in the tested range of *Re* are shown in Table 5.1.

Table 5.1: Variation of C_D with *Re*

Re ($\times 10^4$)	*V* (m/s)	Parabolic profile		Semicircular profile	
		C_{Dmax}	C_{Dmin}	C_{Dmax}	C_{Dmin}
5.3	4.0	0.80	0.07	0.72	0.24
6.0	4.5	1.01	0.08	0.88	0.26
6.6	5.0	1.23	0.14	1.60	0.37
7.3	5.5	1.59	0.14	1.32	0.38
8.0	6.0	1.78	0.18	1.60	0.43
8.6	6.5	2.11	0.21	1.86	0.50
9.3	7.0	2.39	0.20	1.82	0.39
10.0	7.5	2.70	0.25	1.75	0.41
10.6	8.0	2.01	0.25	1.86	0.41

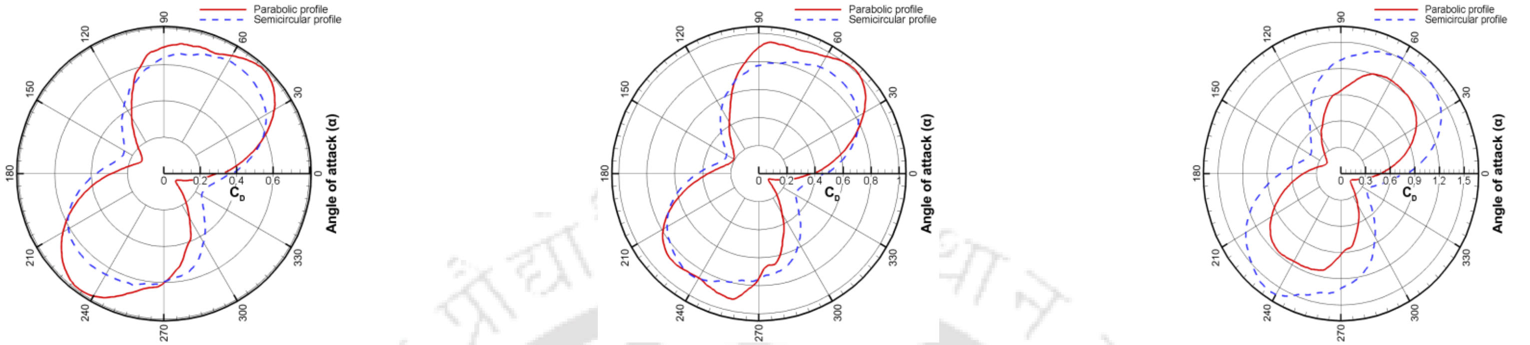

(a) $Re = 5.3\times 10^4$ (V = 4 m/s) (b) $Re = 6 \times 10^4$ (V = 4.5 m/s) (c) $Re = 6.6 \times 10^4$ (V = 5 m/s)

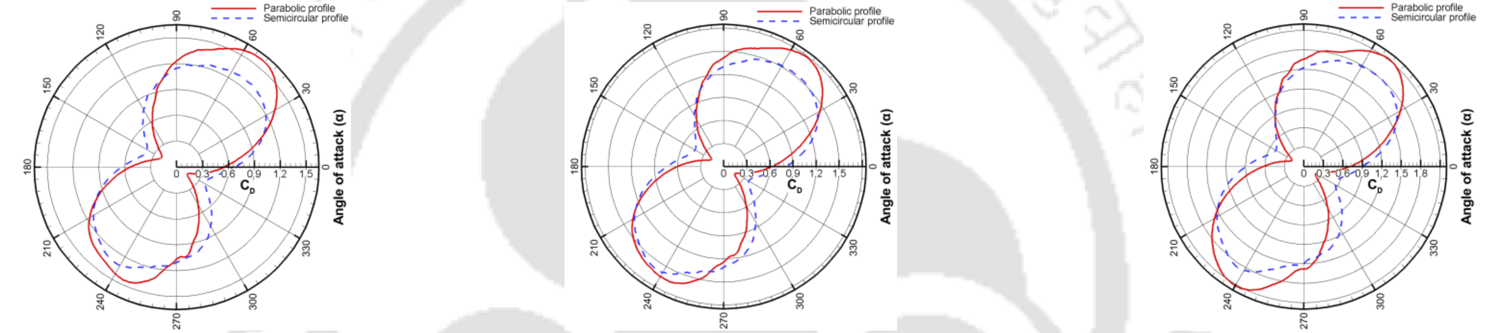

(d) $Re = 7.3 \times 10^4$ (V = 5.5 m/s) (e) $Re = 8.0 \times 10^4$ (V = 6 m/s) (f) $Re = 8.6 \times 10^4$ (V = 6.5 m/s)

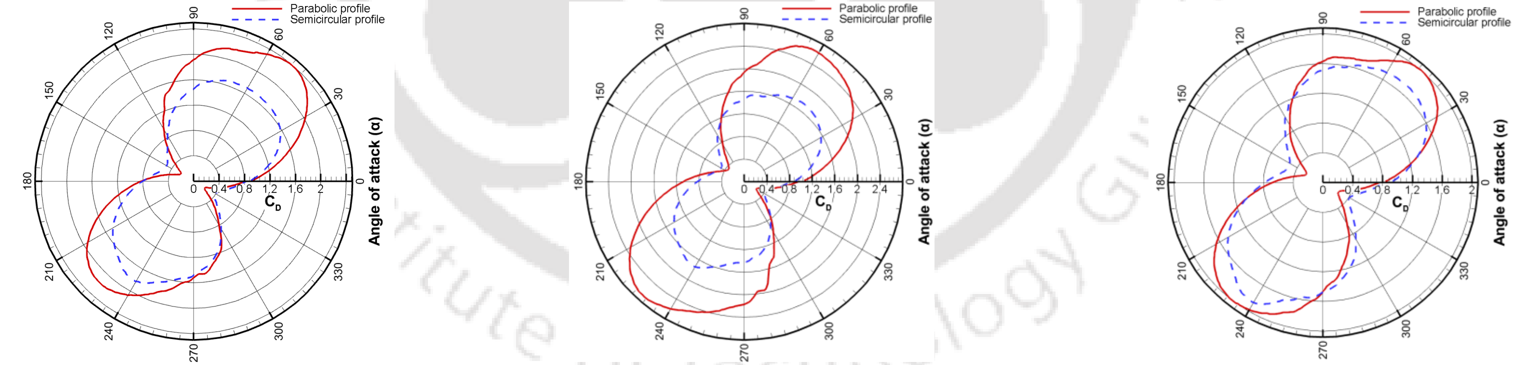

(g) $Re = 9.3 \times 10^4$ (V = 7 m/s) (h) $Re = 10 \times 10^4$ (V = 7.5 m/s) (i) $Re = 10.6 \times 10^4$ (V = 8 m/s)

Figure 5.9: Comparison of C_D at various Re

5.5.1.2 Lift coefficient (C_L)

A notable enhancement in the C_L values is observed throughout the entire rotational cycle of the novel parabolic blade profile. This profile is like that of an aircraft wing and therefore has the primary advantage over the semicircular profile. In the parabolic profile, the C_L increases up to $\alpha = 25°$ (first quarter of the blade rotation), and then decreases to a minimum in the range of $\alpha = 110°$ - $120°$ (second quarter of the blade rotation), followed by an increase till $\alpha = 200°$ (third quarter of the blade rotation). Conversely, for the semicircular profile, the C_L increases to a maximum in the range of $\alpha = 10°$ - $15°$, followed by a decrease till it reaches a minimum at $\alpha = 100°$. A similar pattern is observed for both the profiles in the tested range of *Re*. It can therefore be said that the semicircular profile reaches a maximum C_L at a relatively lower α, and this allows the rotor to rotate earlier than its parabolic counterpart. This is because of the higher curvature of the parabolic profile that significantly increases the pressure gradient on the suction side. This leads to a vertical orientation of the normal pressure and consequently an increase in the lift. Hence, the suction side of the advancing blade acts as the primary surface for the lift generation of the parabolic profile. The Savonius rotor with other types of blade profiles have shown similar observations (Irabu and Roy. 2011; Roy and Ducoin. 2016).

Figure 5.10 depicts the polar variation of C_L over one complete rotation of the rotor. It can be observed that there is not much change in C_L for both the profiles (Figs. 5.10a and 5.10b). However, with a slight increase in *Re*, the C_L of the semicircular profile increases and attains an optimum value at $Re = 8.6 \times 10^4$ (Fig. 5.10c). Apart from this, C_L of the semicircular profile is found to be prominent at lower *Re* as compared to its parabolic counterpart. At $Re = 8.6 \times 10^4$, the C_{Lmax} of semicircular profile is obtained and is found to be 2.25 at $\alpha = 13^{\circ}$and 185° and the C_{Lmin} of 0.45 is attained at $\alpha = 106^{\circ}$. Beyond this *Re*, the $C_{L\ max}$ observed is significantly higher in case of the parabolic profile (Fig. 5.10d-5.10i). While the parabolic profile at $Re = 10\times 10^4$ has demonstrated a C_{Lmax} of 2.87 at $\alpha = 16°$ and a C_{Lmin} of 0.00009 as compared to its semicircular counterpart (Fig. 5.10h). The plots of the C_L also suggest that the optimum *Re* is different for the two test profiles. Table 5.2 shows the variation of C_L with *Re* for the parabolic and semicircular blade profiles. published data is shown in Table 5.3. The $C_{D\ max}$ of the parabolic blade profile is compared with the published data of other blade profiles to get an understanding of the optimum *Re*. At $Re = 1.0\times10^5$, the novel parabolic blade profile has showcased a C_{Dmax} of 2.73 and a C_{Lmax} of 2.87. The other blade profiles such as Modified Bach, Benesh (Alom et al., 2018) elliptical (Alom and Saha, 2019) have shown almost similar optimum *Re* to get the C_{Dmax}.

Table 5.2: Variation of C_L with *Re*

Re ($\times 10^4$)	*V* (m/s)	Parabolic profile		Semicircular profile	
		C_{Lmax}	C_{Lmin}	C_{Lmax}	C_{Lmin}
5.3	4.0	0.89	0.0004	0.84	0.18
6.0	4.5	1.08	0.001	1.09	0.22
6.6	5.0	1.4	0.009	1.89	0.35
7.3	5.5	1.64	0.002	1.61	0.32
8.0	6.0	1.85	0.006	1.89	0.35
8.6	6.5	2.23	0.001	2.25	0.45
9.3	7.0	2.57	0.001	2.12	0.38
10.0	7.5	2.87	0.006	2.23	0.38
10.6	8.0	2.26	0.006	2.15	0.37

On the other hand, a direct comparison of the present aerodynamic coefficients with the previously reported studies is depicted in Table 5.3.

Table 5.3: Comparison of present aerodynamic coefficients with the published data

Investigators	Year	Blade Profile	Methods	*Re*	C_{Dmax}	C_{Lmax}
Irabu and Roy	2011	Semicircular	Experimental	0.64×10^5	1.56	0.6
Jaohandy et al.	2013	Semicircular	Numerical	1.31×10^5	2.20	1.72
Alom et al.	2018	Modified Bach	Numerical	0.89×10^5	2.31	1.97
Alom et al.	2018	Benesh	Numerical	0.89×10^5	1.98	2.25
Alom and Saha	2019	Elliptical	Numerical	0.89×10^5	2.43	2.05
Present Study	2024	Parabolic	Numerical	1.00×10^5	2.73	2.87

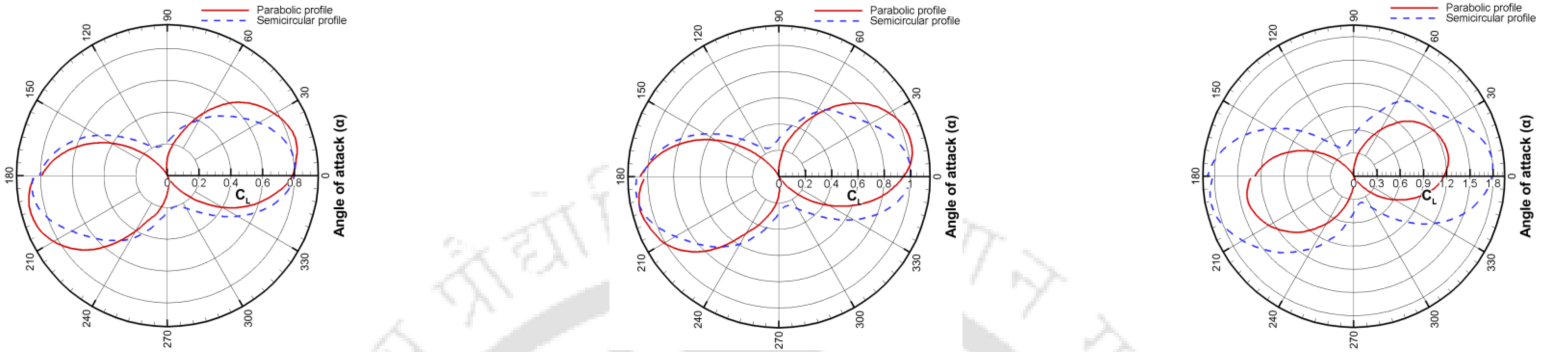

(a) $Re = 5.3\times 10^4$ ($V = 4$ m/s) (b) $Re = 6 \times 10^4$ ($V = 4.5$ m/s) (c) $Re = 6.6 \times 10^4$ ($V = 5$ m/s)

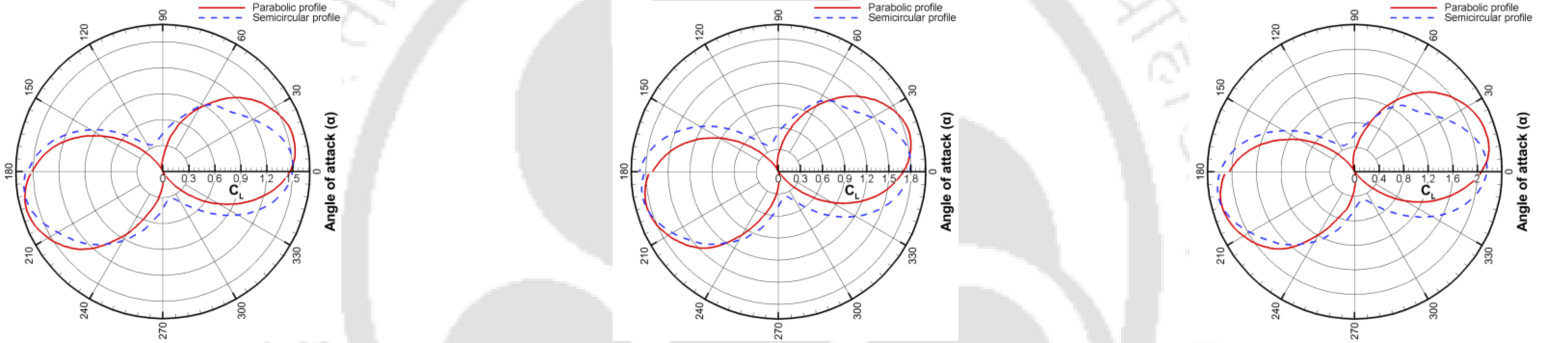

(d) $Re = 7.3 \times 10^4$ ($V = 5.5$ m/s) (e) $Re = 8.0 \times 10^4$ ($V = 6$ m/s) (f) $Re = 8.6 \times 10^4$ ($V = 6.5$ m/s)

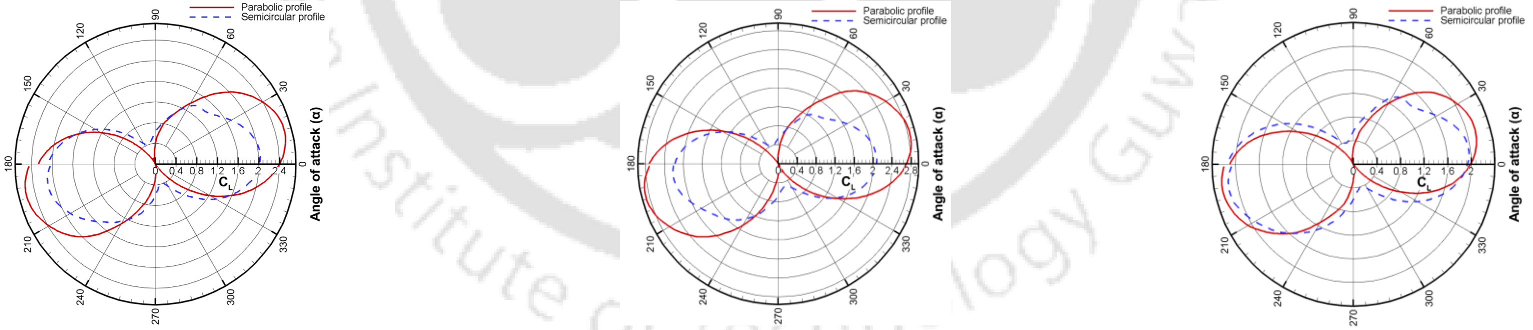

(g) $Re = 9.3 \times 10^4$ ($V = 7$ m/s) (h) $Re = 10 \times 10^4$ ($V = 7.5$ m/s) (i) $Re = 10.6 \times 10^4$ ($V = 8$ m/s)

Figure 5.10: Comparison of C_L at various Re

5.6 Summary

The Savonius rotor, a type of VAWT, is mainly driven by the drag force acting on the blade. This type of turbine is very effective in small-scale power production in remote and inaccessible areas. In the present study, the aerodynamic coefficients (C_D and C_L) of an optimized blade profile developed through the simplex search method is studied. In this regard, 2D unsteady simulations are accomplished for the optimized profile using the SST k-ω turbulence model. For the sake of comparison, 2D unsteady simulations of the conventional semicircular profile are also carried out under identical conditions. From the study, the C_{Dmax} of the optimized profile is found to be 1.91, while for the semicircular profile it is found to be 1.78. This shows an increment of 7.3% for the optimized profile. Moreover, both show similar C_L values and the C_{Lavg} is found to be 1.07.

The influence of Re suggests that the C_D and C_L values are found to be greater in case of the parabolic profile than the semicircular profile. The parabolic profile shows the C_{Dmax} of 2.7 at $Re = 10\times10^4$; whereas the semicircular profile shows the C_{Dmax} of 1.86 at $\mathrm{Re} = 8.6 \times 10^4$. The C_{Davg} for the parabolic and the semicircular profiles is found to be 1.47 and 0.99, respectively. The parabolic profile shows an improvement of C_{Davg} by 49% as compared to its semicircular counterpart. The C_{Lavg} for the parabolic and semicircular profiles is found to be 1.41 and 1.25, respectively. The parabolic profile thus shows an improvement of C_{Lavg} by 12.8%.

Chapter 6

Wind Tunnel Tests

Chapter Outline

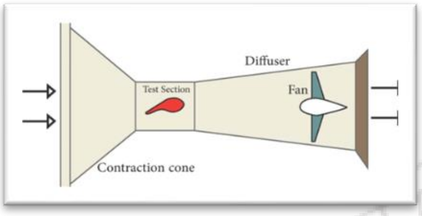

6.1 Introductory Remark

The comprehensive findings of the numerical investigation are mentioned in chapter 4, the parabolic profile with θ of 32.5° proved promising for Savonius rotor blade design. The present chapter deals with wind tunnel experiments on the rotor with parabolic blades to determine its C_P and static torque. In this connection, several two-bladed rotors have been fabricated and tested in the range of *AR*. The road map of the study starting from the blade design to the wind tunnel tests is outlined in Figure 6.1.

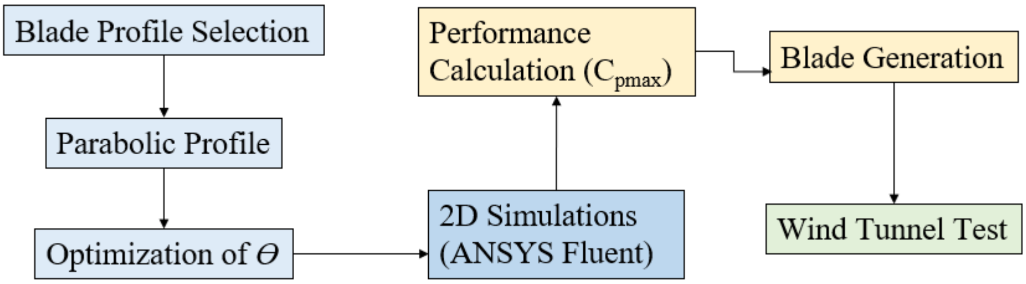

Figure 6.1: The outline of the study

6.2 Description of the Parabolic Blade Design

The blade profile's geometry is created analytically, where the θ is defined by line AB concerning the x-axis on a parabolic curve as shown in Figure 6.2. Line AB divides the parabola, forming an arc AOB. The point C, where line AB meets the y-axis, serves as a pivotal point for adjusting and optimizing the angle θ, representing AOB as one half of the blade profile as discussed in chapter 4.

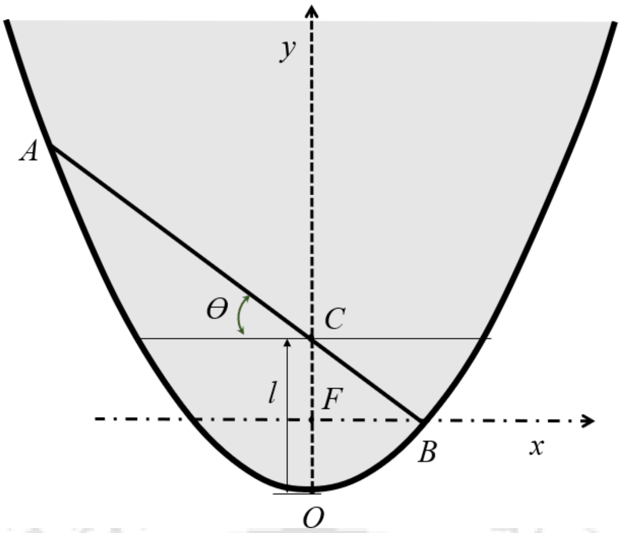

Figure 6.2: The angle (θ) at which the section is cut on the parabola

Geometric details of the tested blades

The top views of the tested blades with their geometric details are shown in Figure 6.3. The overlap between the semicircular and parabolic blades is consistently maintained at 15% of the blade chord length, as previously described (Kalluvia and Sreejith 2018). In each scenario, the overall diameter (D) of the two-bladed rotor is fixed at 230 mm (Roy and Saha, 2015). Additionally, the blades are affixed to a central shaft with a diameter of 12 mm.

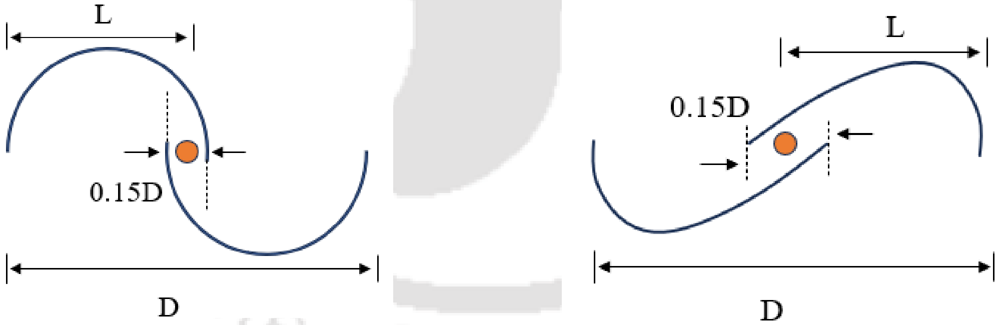

(a) Semicircular (b) Parabolic

Figure 6.3: Specifications of the blade profiles under test

6.3 Experimental setup

The newly designed rotors with parabolic blades were tested in a low-speed wind tunnel of the open test section type as shown in Figure 6.4. This wind tunnel developed by Grinspan et al. (2003, 2004) has been widely utilized by researchers in subsequent studies (Saha and Rajkumar 2006; Saha et al. 2008; Roy and Saha 2015; Alom and Saha 2018; Patel et al.

2023). The tunnel comprises (a) a fan at the beginning to initiate airflow, (b) an inlet section directing the incoming air, (c) a diffuser section to decelerate and stabilize the airflow, (d) a settling chamber equipped with coarse and fine screens as well as a honeycomb structure to create a smooth flow, (e) a nozzle accelerating the airflow, and (f) an open test section housing the tested object and various instruments. The airflow in the tunnel is generated by an axial fan powered by a 0.5 HP motor. A voltage regulator controls the fan, allowing adjustment of the airspeed within the range of 0–10 m/s. The open test section is located at the wind tunnel nozzle's exit, which has a square cross-section of 500 mm × 500 mm. The turbine models are positioned 250 mm away from the wind tunnel exit.

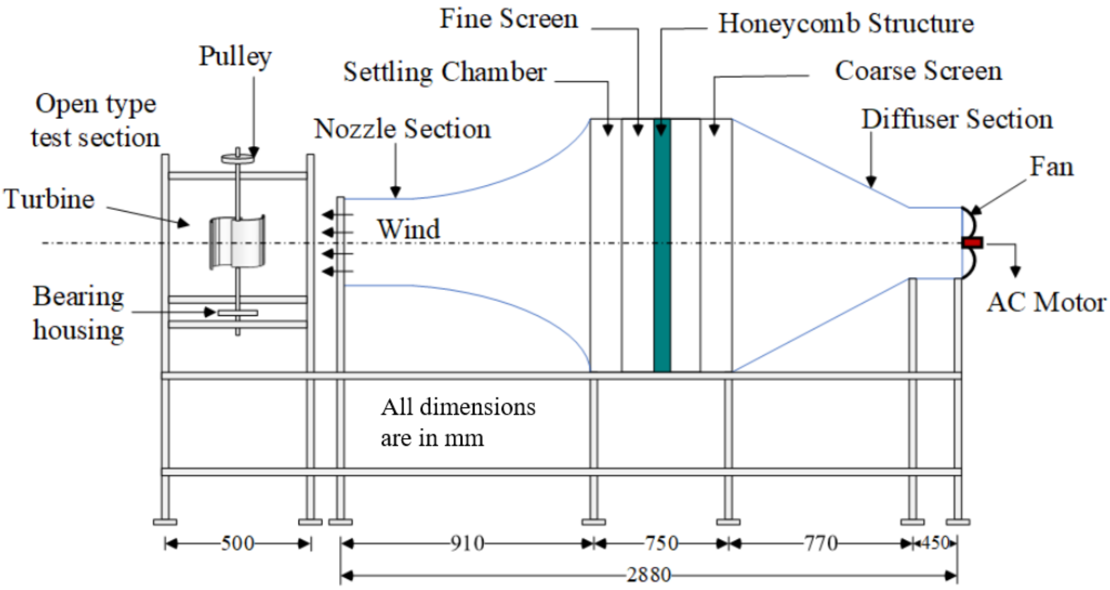

Figure 6.4: A diagram illustrating an open-section wind tunnel

The test section is constructed using mild steel angles measuring 50mm×50mm×4 mm, while the peripheral components of the wind tunnel are made from galvanized iron (GI) sheet with a thickness of 1.6mm. Inside the test section, there are two bearing houses placed at different heights to allow sufficient room for the rotation of the turbine blade. These bearing houses contain an aluminum shaft with a diameter of 12mm and are equipped with two nylon material bushes. The turbine is attached to the shaft using nuts and bolts, positioned at the shaft's center, allowing it to rotate in tandem with the turbine blades. Additionally, the test section features a mass balance holder to which two spring mass balances are affixed. The difference in the readings of these mass balances provides an accurate measurement of the load applied to the turbine.

6.3.1 Fabrication of the turbine blades

The rotors consisting of parabolic (θ =32.5°) and semicircular blades used in this study are manufactured using 0.5 mm thick (GI sheets). In each case, the *AR* of the blades is varied from 0.6 to 1.1. The material used for the fabrication of the blade is strong enough to withstand the wind flow ranging from 0 to 10 m/s. The various blades manufactured are shown in Figure 6.5.


(a) Parabolic blades (b) Semicircular blades

Figure 6.5: Fabricated blades of the test rotors

6.3.2 Measurement procedure

The wind speed is measured using a digital anemometer (Figure 6.6), that operates within a range of 0-20 m/s and provides an accuracy of ±2%. This device detects the wind velocity by recognizing changes in a fluid's physical properties or the fluid's impact on a mechanical device submerged in it.

Figure 6.6: The Anemometer

The voltmeter is supplied with input voltage ranging from 150-220 V, and the corresponding speed is measured using a digital anemometer (Table 6.1). It is important to note that the wind speed remains relatively consistent within the 250×250 mm^2 area around the center. However, there is an increase in speed towards the corners, attributed to the influence of the nozzle section. Hence, considering this variation, the average wind speed is calculated from multiple positions.

Table 6.1: Wind speed measured at various voltage inputs

Fan input voltage (volts)	Wind speed (m/s)
150	3.5
160	4.3
170	5.4
180	6.2
190	7.1
200	7.5
210	8
220	8.5

The torque measurement is accomplished by imposing a load on the rotor through spring balances. A spool is connected to the rotor's shaft, and a rope passes around it, connecting to two mass balances. The rotational speed of the shaft is controlled by applying load through the spring balances to achieve the desired speed. As the shaft starts rotating, one part of the spring balance becomes taut while the other remains slack, as depicted in Figure 6.7. The disparity in their readings indicates the operational load on the shaft. To measure the rotor's rotational speed, a digital tachometer with a range of 0-50000 *RPM* and an accuracy of ±1.0% is employed.

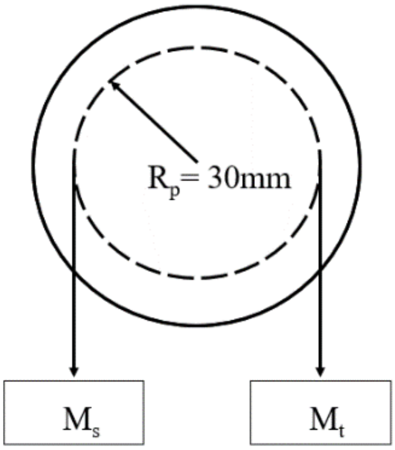

Figure 6.7: The tight and slack side of rope

To attain the desired rotational speed, the load on the shaft is adjusted, and measurements from the mass balance are recorded (M_t and M_s). The output torque (T_o) is then calculated as follows:

$$\text{Output Torque } (To) = (Mt - Ms) \times \mathrm{g} \times Rp \tag{6.1}$$

where M_t and M_s are mass on tight and slack sides, g is the gravitational acceleration and R_p is the radius of the pulley.

The total input torque to the system is calculated as:

$$\text{Input Torque } (Ti) = 0.5\rho A V^2 L \tag{6.2}$$

Here, ρ represents the air density, A denotes the frontal area (calculated as $D\times H$), V stands for the inlet air velocity, and R represents the radius of the turbine blade

Using the equations, the torque coefficient (C_T) is calculated as:

$$C_T = T_O/T_i = ((M_t - M_s) \times g \times R_p)/0.5\rho A V^2 L \tag{6.3}$$

After calculating (C_T), the power coefficient (C_p) is calculated as:

$$C_P = C_T \times TSR \tag{6.4}$$

6.4 Discussion of Wind Tunnel Tests

This section deals with the error analysis followed by the effect of *AR*, dynamic and static performance analysis, and the blockage effect.

6.4.1 *Effect of aspect ratio (AR)*

The aspect ratio ($AR = H/D$) is an important geometric parameter of a Savonius rotor. The literature reveals that with an increase in *AR* the moment and the inertia of the rotor get decreased, but angular acceleration increases. A higher *AR* rotor blade is desired at higher wind speeds. Thus, the variation of *AR* (0.6-1.1) study is done in this section to get the optimum *AR* in terms of C_{Pmax} the wind tunnel experiment shows that the parabolic blade outperformed the conventional semicircular blade throughout the range of *AR* (Figure 6.8). Moreover, the C_P goes on decreasing while moving from $AR = 0.9$. Thus, the optimum $AR = 0.9$ is chosen for further progression of the present study.

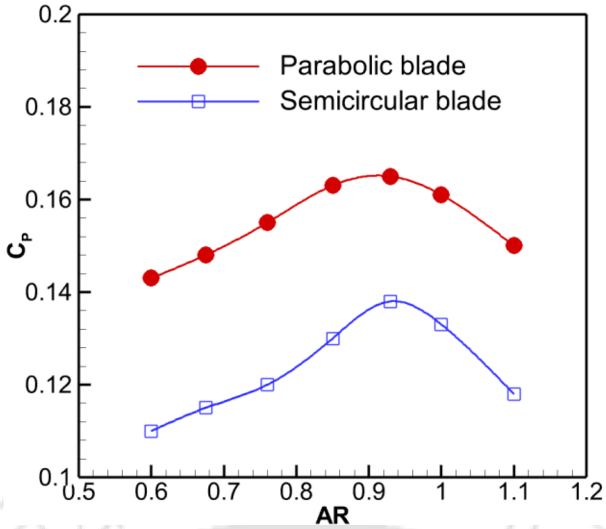

Figure 6.8: Changes in C_P concerning different *AR*

6.4.2 *Error analysis*

In each experiment, it is not possible to get the exact value of the readings every time. The readings keep on changing when they are taken repetitively. Thus, the mean value is calculated to get the result. It is therefore necessary to make an error analysis in such a way that the fluctuations can be understood to get the accuracy of the experimental results. For this, the standard deviation as given by eqn. 6.5 (Holman 2004; Roy and Saha 2015) is used.

The uncertainties in the experiment can be estimated using the sequential perturbation technique (Moffat 1982; Kline 1985), revealing values of 4.5%, 4.8%, and 2.9% for C_P, C_T, and *T* respectively.

$$\sigma = \sqrt{\frac{1}{J}\sum_{i=1}^{J}(x_i - m)^2} \times 100\% \qquad (6.5)$$

In the given equations, σ represents the standard deviation, *J* indicates the number of data points, *m* represents the mean value, and *x* denotes the measured value. Several data points are gathered for a particular load and shaft speed. The error analysis was conducted for both the parabolic-bladed and semicircular-bladed rotors at an inlet air speed of 7 m/s. According to the analysis, the percentage deviation for the parabolic-bladed rotor was determined to be 4.5% (Figure 6.9), whereas for the semicircular-bladed rotor, it was approximately 4% (Figure 6.10).

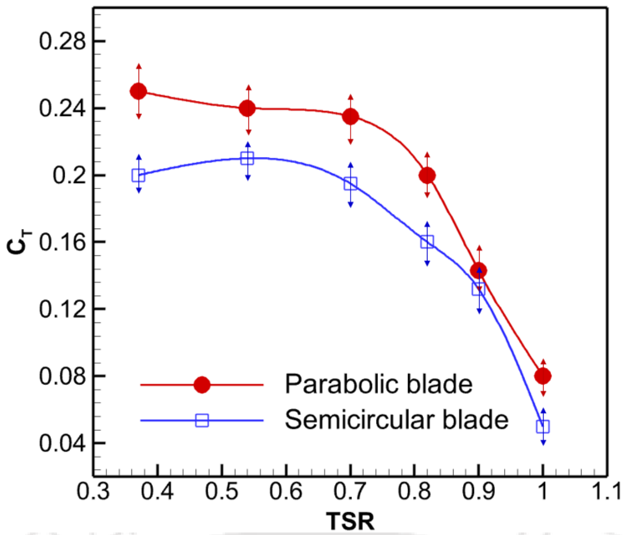

Figure 6.9: Standard deviation of C_T at various *TSRs*

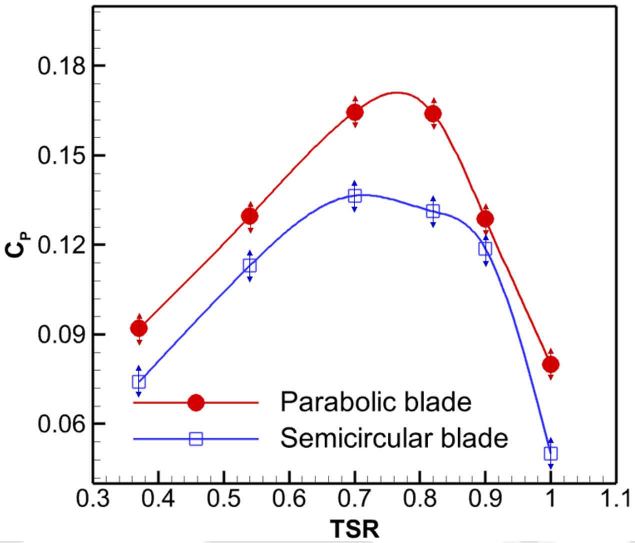

Figure 6.10: Standard deviation of C_P at various *TSRs*

6.4.3 Dynamic Performance analysis

The dynamic performance assessment involves evaluating the C_T and C_P of the parabolic-bladed rotor. For a direct comparison, the dynamic performance of the semicircular-bladed rotor has also been assessed. Wind tunnel tests were conducted at an air speed of 7 m/s. Figure 6.11 illustrates how C_T and C_P vary with TSR for the tested rotors. The parabolic-bladed rotor (*AR*=0.9) achieves C_{Pmax} of 0.165 at *TSR* = 0.7, while the semicircular-bladed rotor at the same *AR* exhibits a C_{Pmax} of 0.138 at *TSR* = 0.69. This indicates a notable 19.56% performance improvement of the parabolic-bladed rotor over its semicircular counterpart. This enhancement is attributed to the accelerated flow in the overlap region, generating an additional force on the concave side of the returning blade.

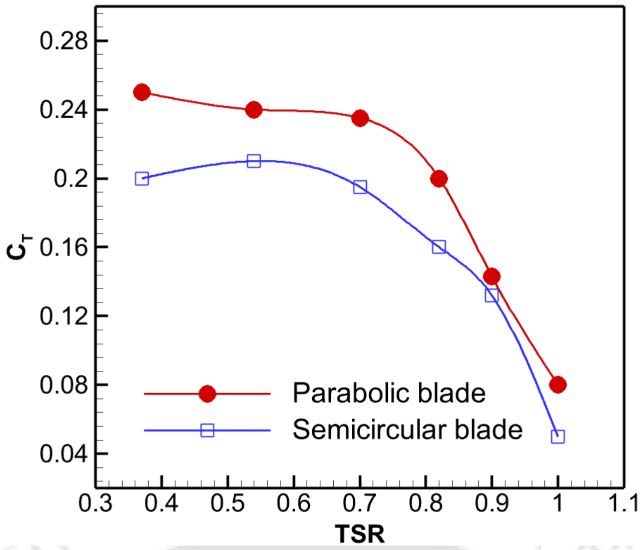

(a) C_T vs *TSR*

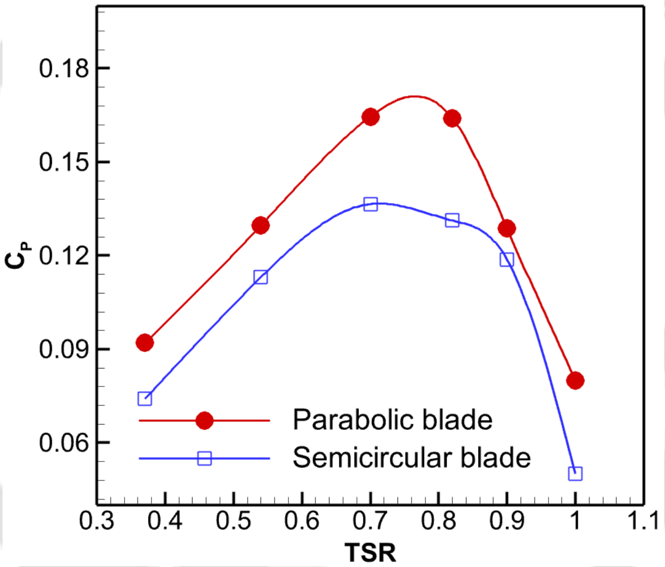

(b) C_P vs *TSR*

Figure 6.11: Performance coefficients obtained by wind tunnel tests

It is evident that the C_T value decreases with increasing *TSR* due to gradual loads on the turbine shaft reducing rotational speed. Conversely, the C_P rises with higher *TSR* values and reaches a peak beyond which it decreases. The superior performance of the parabolic-bladed rotor is due to its straight blade trailing edge and a higher radius of curvature at the leading edge compared to the semicircular-bladed rotor. This results in higher pressure drag. The parabolic-bladed rotor having a straight trailing edge on the returning blade guides the flow whereby the rotor's moment increases. Additionally, the straight leading edge delays the flow separation, enhancing the pressure recovery. This reduces the negative torque, and increases the rotor C_P.

6.4.4 *Static performance analysis*

Static torque (C_{Ts}) is a measure of the rotor's starting capability without causing angular rotation. Figure 6.12 displays the variation of C_{Ts} at different angles of attack (α). The α represents the angle between the chord of the advancing blade and the wind flow direction. The starting capabilities of both the parabolic and semicircular-bladed rotors were assessed at V = 7 m/s. The parabolic design exhibited superior C_{Ts} across the entire range of α. For the semicircular-bladed rotor, lower C_{Ts} were observed between α = 125°-180° and α = 290°-350° due to negative pressure on the returning blade, hindering its self-starting. However, the self-rotation occurred between α = 30°-60° and 210°-240°, representing its optimal starting range. At α = 30° and 160°, the semicircular-bladed rotor exhibited C_{Ts} of 0.27 and -0.16, respectively. In contrast, the parabolic-bladed rotor displayed higher C_{Ts} within the α range, demonstrating its enhanced self-starting ability. At α = 220° and 162°, the parabolic-bladed rotor achieved maximum and minimum C_{Ts} of 0.35 and -0.133, respectively, indicating a 29.6% increase in its maximum C_{Ts} compared to the semicircular design.

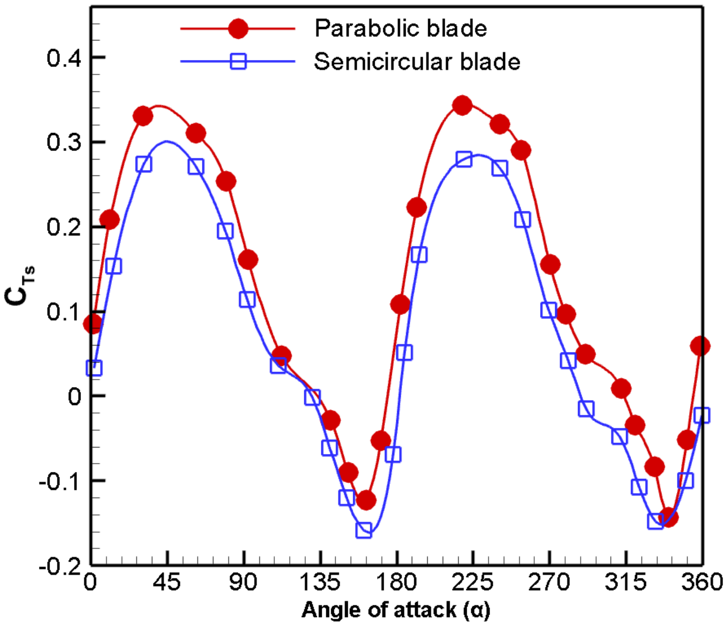

Figure 6.12: Fluctuation of static C_{Ts} at various α

6.5 Blockage effect

In experimental studies, accounting for the blockage effect is vital, as emphasized in previous research (Abraham et al. 2012; Plourde et al. 2012). The blockage correction factor (f) relies on the type of wind tunnel test section and the blockage ratio (BR). The BR is the ratio of the turbine blade area to the test section area. Traditionally, the blockage correction has extensively been investigated for closed test sections (Biswas et al. 2007; Chen and Liou

2011; Akwa et al. 2012). However, the relationships established for the closed test sections do not apply to those of open test sections (Roy and Saha 2015). To bridge this gap, Roy and Saha (2014) introduced a new relationship for the blockage correction specifically tailored to wind tunnel experiments of Savonius rotors in open test sections. This correction factor (*f*) is crucial for adjusting the measured parameters such as wind velocity (*V*), applied mechanical load (F) on the turbine, and rotational speed (*N*). These variables are expressed by the following equations (Roy and Saha, 2014; Alom and Saha 2018).

$$V^* = V(1 - \frac{1}{5}f) \tag{6.10}$$

$$F^* = F(1 - f) \tag{6.11}$$

$$N^* = N(1 - f) \tag{6.12}$$

In these equations, *V**, *F**, and *N** denote the blockage-corrected values. The blockage correction factor (*f*) is determined by the *TSR* and *BR*. By applying these equations, a suitable blockage correction factor (*f*) ranging from 4% to 9% was applied, corresponding to various *TSR* and *BR* values of 21.16% (Roy and Saha, 2014). After applying the blockage correction, the C_{Pmax} values for the parabolic- and semicircular-bladed rotors were determined to be 0.161 and 0.134, respectively (Figures 6.13 and 6.14).

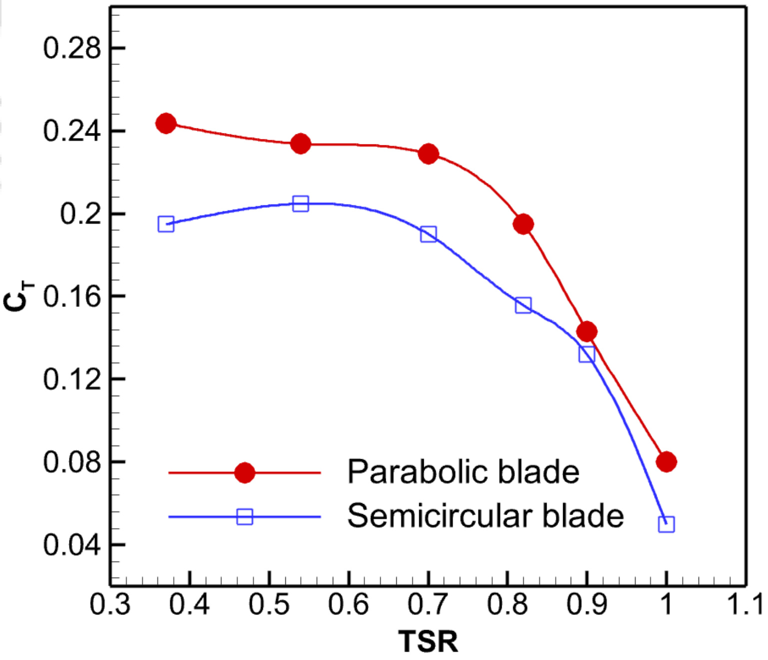

Figure 6.13: Blockage corrected C_T with *TSR*

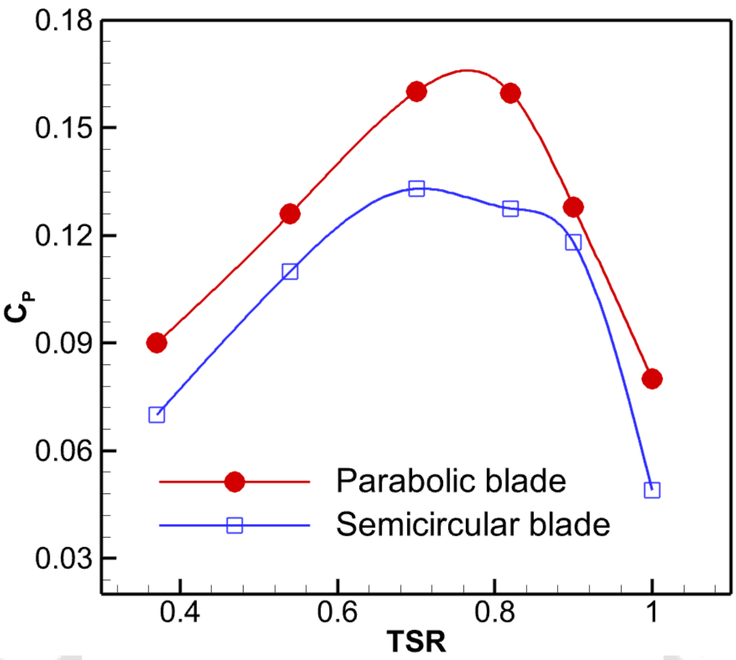

Figure 6.14: Blockage corrected C_P with *TSR*

6.6 Summary

The performance analysis of a newly developed parabolic-bladed rotor was conducted focusing on its C_{Pmax} at various *AR and TSR*. To have a direct comparison, a semicircular-bladed rotor was also tested under identical condition. It was observed that specifically at *AR* = 0.9, *TSR* of 0.67, and *V*= 7 m/s, the parabolic-bladed rotor exhibited a C_{Pmax} of 0.165, while the semicircular-bladed rotor showed a C_{Pmax} of 0.138. This indicates a 19.56% improvement in C_P for the parabolic-bladed rotor over the semicircular counterpart.

Additionally, the study delved into the static torque performance of the parabolic-bladed rotor. The parabolic-bladed rotor exhibited higher C_{Ts} values and superior self-starting capabilities, ranging from 0.35 to -0.133, at α = 220° and 162°. The semicircular-bladed rotor, on the other hand, displayed C_{Ts} values ranging from 0.27 to -0.16. Thus, the parabolic-bladed rotor demonstrated a 29.6% enhancement in C_{Ts} values.

With the blockage correction, the parabolic-bladed rotor achieved a C_P of 0.161, surpassing the semicircular-bladed rotor's C_P of 0.134. The physical attributes of the newly developed parabolic-bladed rotor featuring a straight trailing edge and a higher radius of curvature at the leading edge contributes to the increased pressure drag. Notably, this higher-pressure drag was more pronounced on the advancing side of the parabolic-bladed rotor compared to the semicircular rotor.

Chapter 7

Conclusions and Future Scope

Chapter Outline

7.1 Contribution of the Present Work

The Savonius rotor, a type of drag-based vertical axis wind turbine, presents a promising solution for small-scale, cost-effective off-grid energy production, particularly in confined spaces and low wind speed regions where traditional turbines may suffer. The current study aims to enhance the aerodynamic efficiency of the Savonius rotor by developing two novel blade designs using optimization and analytical approaches. To begin with, a natural cubic spline blade profile is used to generate a new blade profile using the optimization algorithms. Subsequently, another new parabolic blade profile is developed by an analytical approach. For both the cases, using SST k-ω turbulence model, 2D unsteady simulations are carried out to find out their performance characteristics. Finally, the wind tunnel experiments are conducted with the parabolic-blade rotor.

7.2 Key Findings

The key findings of the present investigations are summarized in the subsequent sections.

7.2.1 *Optimization and 2D unsteady simulations – spline blade profile*

- ✓ The optimal blade profile generated through SSM can easily be obtained by entering the natural cubic spline by points (-96, 0), (-75.63, -32.63), (4, 0) and (-4, 0) (75.63, 32.63) and (96, 0). Here, only one variable point is used to define a blade geometry.
- ✓ In *SSM*, the C_{Pmax} of the optimized spline and semicircular profiles is found to be 0.283 and 0.23, respectively. The optimal profile shows its improved performance in the range of *TSR* =0.6–1.
- ✓ In case of *NSGA-II*, three intermediate points are applied keeping *TSR* and *V* as other two design variables.

- ✓ In *NSGA-II*, the $C_{P\,max}$ is found to be 0.286 at a $V = 9.88$ m/s. While in *SSM*, the $C_{P\,max}$ is 0.283 at $V = 7.3$ m/s.
- ✓ The C_{Dmax} of the optimized spline profile is found to be 1.91, while for the semicircular profile it is found to be 1.78. This shows an increment of 7.3% for the optimized spline profile. Moreover, both show similar C_L values and the C_{Lavg} is found to be 1.07.
- ✓ The velocity magnitude and the total pressure obtained are found to be higher in the vicinity of advancing side of optimized spline profile, while the turbulence intensity is found to be lesser as compared to the semicircular profile.

7.2.2 *2D unsteady simulations – parabolic blade profile*

- ✓ The results obtained show an optimum performance of the parabolic blade profile at $\theta = 32.5^{o}$.
- ✓ The optimum parabolic profile shows a peak C_P of 0.319 at *TSR* = 0.8 at velocity of 6.7 m/s, whereas the semicircular profile shows a peak C_P of 0.2663 at the same *TSR* and velocity. There is an improvement of C_{Pmax} by around 20% in the 2-bladed parabolic profile in comparison to the semicircular profile.
- ✓ As the parabolic profile is characterized by a lower curvature, the flow separation on this profile is likely to get delayed as compared to its semicircular counterpart. This enhances the pressure recovery thereby reducing the negative torque and improving the performance of the rotor.
- ✓ The increase in *Re* leads to higher C_T and C_P for both the test profiles. Each profile reaches an optimum performance at different *Re*. The parabolic profile shows improved C_P against the semicircular counterpart at higher *Re* ($>7.3\times 10^4$). The novel parabolic profile reaches a C_{Pmax} of 0.35 whereas the semicircular profile achieves a C_{Pmax} of 0.30.
- ✓ At higher *Re*, the parabolic blade profile reaches optimum value of C_P, while the semicircular profile reaches an optimum value comparatively at a lower *Re*. The C_{Pmax} of the parabolic profile is obtained at $Re = 10 \times 10^4$, while the C_{Pmax} of the semicircular profile is obtained at $Re = 8.6 \times 10^4$. As compared to the semicircular profile, the parabolic profile shows an improvement of C_{Pmax} by 16.6%.
- ✓ The C_D and C_L values are found to be greater in the case of the parabolic profile than the semicircular profile. The parabolic profile shows the $C_{D\,max}$ of 2.7 at $Re = 10 \times 10^4$; whereas the semicircular profile shows the C_{Dmax} of 1.86 at $Re = 8.6 \times 10^4$.

7.2.3 *Wind tunnel tests*

- ✓ The parabolic-bladed rotor (*AR* = 0.9, *TSR* of 0.67, and *V*=7 m/s) exhibits a C_{Pmax} of 0.165, while the semicircular-bladed rotor shows a C_{Pmax} of 0.138. This indicates a 19.56% improvement in C_P for the parabolic-bladed rotor over the semicircular counterpart.
- ✓ At α = 220° and 162°, the parabolic-bladed rotor exhibits a higher C_{Ts} and shows a superior self-starting capability (0.35 to -0.133). The semicircular-bladed rotor, on the other hand, displays C_{Ts} values ranging from 0.27 to -0.16. Thus, the parabolic-bladed rotor demonstrated a 29.6% enhancement in C_{Ts} values.
- ✓ With the blockage correction, the parabolic-bladed rotor achieved a C_P of 0.161, surpassing the semicircular-bladed rotor's C_P of 0.134.

7.3 Application Potential

The parabolic-bladed Savonius rotors may find their applications in compact spaces, facilitating multiple rotor configurations. When paired with an energy storage system, these rotors prove advantageous atop buildings, communication towers, or in hilly terrain for decentralized small-scale electricity generation. Additionally, they may find utility in water pumping for the irrigation purposes.

7.4 Scope for Future Work

- ✓ Soft computing viz: ANN, Neuro fuzzy, and others could be implemented to obtain different spline blade profile.
- ✓ The present parabolic blade is obtained without applying optimization or soft-computing techniques. Thus, there is a possibility of generating further optimized parabolic blades.
- ✓ The present parabola considers the standard parabolic equation with vertex (0, -2) and directrix length (a = 2). Thus, there could be N number of parabolas which could be taken up for further investigations.
- ✓ In order to enhance the performance of the parabolic rotor, future research could be explored by incorporating end plates, augmented techniques, or multi-staging.
- ✓ Light weight blade materials can also be used for the rotor design to improve the self-starting capability of the parabolic-bladed rotor.
- ✓ A prototype could be developed to power the streetlights of highways and railway tracks, where wind speed is found to be around 5-10 m/s.

References

Abraham, J. P., Plourde, B. D., Mowry, G. S., Minkowycz, W. J., and Sparrow, E. M., 2012. Summary of Savonius wind turbine development and future applications for small-scale power generation. Journal of Renewable and Sustainable Energy, 4, pp. 042703-1-042703-21.

Agrawal, A., Kansagara, D. D., Sharma, D., Saha, U. K., 2019. Savonius wind turbine blade profile optimization by coupling CFD simulations with simplex search technique. In: American Society of Mechanical Engineers, Gas Turbine India Conference, Vol. 83532, pp. V002T06A007. India (December 2019).

Akwa, J. V., Alves Da Silva Junior, G., and Petry, A. P., 2012. Discussion on the verification of the overlap ratio influence on performance coefficients of a Savonius wind rotor using computational fluid dynamics. Renewable Energy, 38, pp. 141–149.

Akwa, J. V., Vielmo, H. A., and Petry, A. P., 2012. A review on the performance of Savonius wind turbines. Renewable Sustainable Energy Reviews, 16, pp. 3054–3064.

Alexander, A. J., and Holownia, B. P., 1978. Wind tunnel tests on a Savonius rotor. Journal of Industrial Aerodynamics, 3, pp. 343–351.

Alaimo, A., Esposito, A., Milazzo, A., Orlando, C., and Trentacosti, F., 2013. Slotted blades Savonius wind turbine analysis by CFD. Energies, 6, pp. 6335-6351

Alakashi, A. M., and Basuno, I. B., 2014. Comparison between structured and unstructured grid generation on two dimensional flows based on Finite Volume Method (FVM). International Journal of Mining, Metallurgy & Mechanical Engineering (IJMMME), vol. 2, Issue 2, pp. 97–103.

Aldoss T., and Najjar, Y., 1985. Further development of the swinging-blade Savonius rotor. Wind Engineering. 9, pp. 165–170.

Alom, N., and Saha, U. K., 2018. Evolution and progress in the development of Savonius wind turbine rotor blade profiles and shapes. ASME Journal of Solar Energy Engineering 141(3):030801.

Alom, N., and Saha, U. K., 2018. Performance evaluation of vent-augmented elliptical-bladed Savonius rotors by numerical simulation and wind tunnel experiments. Energy 152:277–90.

Alom, N., Kolaprathi, S. C., Gadde, S. C., and Saha, U. K., 2016. Aerodynamic design optimization of elliptical-bladed Savonius-style wind turbine by numerical simulations. Paper No. OMAE2016-55095, ASME 35th International Conference on Ocean, Offshore and Arctic Engineering, June 19–24, Busan, South Korea.

Alom, N., Borah, B., and Saha, U.K., 2018, "An insight into the drag and lift characteristics of modified Bach and Benesh profiles of Savonius rotor," Energy Procedia, 144, pp. 50-56.

Alom, N., Kolaparthi, S. C., Gadde, S. C., and Saha, U. K., 2016, "Aerodynamic design optimization of elliptical-bladed Savonius-style wind turbine by numerical simulations," Paper No. OMAE2016-55095, ASME 35th International Conference on Ocean, Offshore and Arctic Engineering, June 19-24, Busan, South Korea.

Alom, N., Das, R., and Saha, U. K., 2019. Optimization of aerodynamic parameters of an elliptical-bladed Savonius wind rotor using multi-objective genetic algorithm, Paper No. GTIndia2019-2346, ASME Gas Turbine India Conference, December 05–06, Chennai, India.

Alom, N., and Saha, U. K., 2017. Arriving at the optimum overlap ratio for an elliptical-bladed Savonius rotor. Paper No. GT2017-64137, ASME 2017 Turbo Expo, June 26–30, Charlotte, North Carolina, USA.

Alom, N. and Saha, U. K., 2019. Examining the aerodynamic drag and lift characteristics of a newly developed elliptical-bladed Savonius rotor. ASME Journal of Energy Resources Technology, 141(5), p.051201.

Altan, B. D., and Atilgan, M., 2010. The use of a curtain design to increase the performance level of a Savonius wind rotors. Renewable Energy, 35, pp. 821–829.

Altan, B. D., and Atilgan, M., 2008. An experimental and numerical study on the improvement of the performance of Savonius wind rotor. Energy Conversion and Management, 49, pp. 3425–3432.

Amano, R. S., 2017. Review of wind turbine research in 21st century. ASME Journal of Solar Energy Engineering, 139(5), pp. 50801.

ANSYS Inc, 2009. ANSYS Fluent Theory Guide 12.0.

ANSYS Inc, 2015. ANSYS Fluent Theory Guide 12.0.

Banerjee, A., Roy, S., Mukherjee, P., and Saha, U. K., 2014. Unsteady flow analysis around an elliptic-bladed Savonius-style wind turbine. Paper No. GTINDIA2014-8141, ASME 2014 Gas Turbine India Conference, December 15-17, New Delhi, India.

Bach, G., 1931. Untersuchungen uber Savonius-Rotoren und verwandte Stromungsmaschinen. Forsch. Geb. Ingenieurwes. 2(6), pp. 218–231.

Benesh, A. H., 1988. Wind turbine system using a vertical axis Savonius type rotor. in U.S. patent US5494407 A (November 15). Benesh, A. H., 1989. Wind turbine system using a Savonius type rotor. U.S. patent 4838757 (July 10).

Benesh, A. H., 1992. The Benesh wind turbine. in Eleventh ASME Wind Energy Symposium.

Blackwell, B. F., Sheldahl, R. E., and Feltz, L. V., 1977. Wind tunnel performance data for two- and three-bucket Savonius rotors, Sandia Laboratories Report: SAND 76-0131, pp. 1-105.

Chauvin, A. and Benghrib, D., 1989. Drag and lift coefficients evolution of a Savonius rotor. Experiments in Fluids; 8(1-2), pp. 118-20.

Chan, C. M., Bai, H. L., and He, D. Q., 2018. Blade shape optimization of the Savonius wind turbine using a genetic algorithm. Applied Energy, 213, pp. 148–157.

Chong, W. T., Pan, K. C., Poh, S. C., Fazlizan, A., Oon, C. S., Badarudin, A., and Nik-ghazali, N., 2013. Performance investigation of a power augmented vertical axis wind turbine for urban high-rise application. Renewable Energy, 51, pp. 388–397.

Council, Global Wind Energy. "GWEC global wind report 2019." *Global wind energy council: Bonn, Germany* (2017).

D'Alessandro, V., Montelpare, S., Ricci, R., and Secchiaroli, A., 2010. Unsteady aerodynamics of a Savonius wind rotor: A new computational approach for the simulation of energy performance. Energy, 35, pp. 3349–3363.

Damak, A., Driss, Z., and Abid, M. S., 2013. Experimental investigation of helical Savonius rotor with a twist of 1800 Renewable Energy, 52, pp. 136–142.

Damak, A., Driss, Z., and Abid, M. S., 2018, "Optimization of the helical Savonius rotor through wind tunnel experiments," Journal of Wind Engineering & Industrial Aerodynamics, 174 (December 2017), pp. 80–93.

Driss, Z., Mlayeh, O., Driss, D., Maaloul, M., and Abid, M. S., 2014. Numerical simulation and experimental validation of the turbulent flow around a small incurved Savonius wind rotor. Energy, 74, pp. 506–517.

Dobrev, I., and Massouh, F., 2011. CFD and PIV investigation of unsteady flow through Savonius wind turbine. Energy Procedia, 6, pp. 711–720.

Ducoin, A., Shadloo, M. S., and Roy, S., 2017. Direct numerical simulation of flow instabilities over Savonius style wind turbine blades. Renewable Energy, 105, pp. 374–385.

El-Askary, W. A., Nasef, M. H., Abdel-hamid, A. A., and Gad, H. E., 2015. Harvesting wind energy for improving performance of Savonius rotor. Journal of Wind Engineering & Industrial Aerodynamics, 139, pp. 8–15.

Emmanuel, B., and Jun, W., 2011. Numerical study of a six-bladed Savonius wind turbine. ASME Journal of Solar Energy Engineering, 133, pp. 44503.

Faizal, M, Ahmed, M. R., and Lee, Y. H. 2010. On utilizing the orbital motion in water waves to drive a Savonius rotor. Renewable Energy, 35, pp.164–169

Frikha, S., Driss, Z., Ayadi, E., Masmoudi, Z., and Abid, M. S., 2016. Numerical and experimental characterization of multi-stage Savonius rotors. Energy 114, pp. 382–404.

Fujisawa, N., 1996. Velocity measurements and numerical calculations of flow fields in and around Savonius rotors. Journal of Wind Engineering & Industrial Aerodynamics ,59, pp. 39–50.

Fujisawa, N., 1992. On the torque mechanism of Savonius rotors. Journal of Wind Engineering & Industrial Aerodynamics, 40, pp. 277–292.

Fujisawa, N., and Gotoh, F., 1994. Experimental study on the aerodynamic performance of a Savonius rotor. ASME Journal Solar Energy Engineering, 116, pp. 148–152.

Fujisawa, N., Ishimatsu, K., and Kage, K., 1995. A comparative study of Navier-Stokes calculations and experiments for the Savonius rotor. ASME Journal Solar Energy Engineering 117, pp. 344.

Gareth, C., and Mishra, R., 2011. Computational flow field analysis of a Vertical Axis Wind Turbine. In: International Conference on Renewable Energies and Power Quality (ICREPQ'11), April 13-15, Las Palmas de Gran Canaria, Spain.

Golecha, K., Eldho, T. I., and Prabhu, S. V., 2011. Influence of the deflector plate on the performance of modified Savonius water turbine. Appled Energy, 88, pp. 3207–3217.

Grinspan, A. S., 2002. Development of a low-speed wind tunnel and testing of Savonius wind turbine rotor with twisted blades. M. Tech Thesis, Department of Mechanical Engineering, IIT Guwahati, India.

Grinspan, A. S., Saha, U. K., and Mahanta, P., 2004. Experimental investigation of twisted bladed savonius wind turbine rotor. RERIC International Energy Journal, 5, pp. 1–9

Gupta, A. K., 2015. Efficient wind energy conversion: Evolution to modern design. ASME Journal of Energy Resourse Technology, 137, pp. 51201.

Gupta, R., Biswas, A., and Sharma, K. K., 2008. Comparative study of a three-bucket Savonius rotor with a combined three-bucket Savonius-three-bladed Darrieus rotor. Renewable Energy, 33, pp. 1974–1981.

Gerardo, G., and Molfino, R., 2014.From Savonius to Bronzinus: a comparison among vertical wind turbines. Energy Procedia, 50, pp. 10–18. Global Wind Energy Outlook 2016, GWEC.

Hayashi, T., Li, Y., and Hara, Y., 2005. Wind tunnel tests on a different phase three-stage Savonius rotor. JSME International Journal, Ser. B 48, pp. 9–16.

Howell, R., Qin, N., Edwards, J., and Durrani, N., 2010. Wind tunnel and numerical study of a small vertical axis wind turbine. Renewable Energy, 35, pp. 412–422.

Holman, J. P., 2004. Experimental Methods for Engineers. Tata McGraw Hill, New Delhi, India.

Huda, M. D., Selim, M. A., Sadrul, Islam, A. K. M., and Islam, M. Q., 1992. The performance of an S-shaped Savonius rotor with a deflecting plate. RERIC International Energy Journal. 14(1), pp. 25-32

Hu, Y., Tong, Z., and Wang, S., 2009. A new type of VAWT and blade optimization. Int. Technol. Innov. Conf. 2009 (ITIC 2009), pp. 14–14.

Irabu, K., and Roy, J. N., 2011. Study of direct force measurement and characteristics on blades of Savonius rotor at static state. Experimental Thermal and Fluid Science, 35, pp. 653–659

Irabu, K., and Roy, J. N., 2007. Characteristics of wind power on Savonius rotor using a guidebox tunnel. Experimental Thermal and Fluid Science, 32, pp. 580–586.

Jian, C., Kumbernuss, J., Linhua, Z., Lin, L., and Hongxing, Y., 2012. Influence of phase-shift and overlap ratio on Savonius wind turbine's performance. ASME Journal of Solar Energy Engineering, 134, pp. 11016.

Jaohindy, P., McTavish, S., Garde, F. and Bastide, A., 2013. An analysis of the transient forces acting on Savonius rotors with different aspect ratios. Renewable Energy, 55, pp. 286- 295.

Jeon, K. S., Jeong, J. I., Pan, J. K., and Ryu, K. W., 2015. Effects of end plates with various shapes and sizes on helical Savonius wind turbines. Renewable Energy, 79, pp. 167-176.

Kacprzak, K., Liskiewicz, G., and Sobczak, K., 2013. Numerical investigation of conventional and modified Savonius wind turbines. Renewable Energy, 60, pp. 578–585.

Kamoji, M. A., Kedare, S. B., and Prabhu, S. V., 2009. Performance tests on helical Savonius rotors. Renewable Energy, 34, pp. 521–529.

Khan, J. R., Bashar, M. M., Rahman, M., Bashar, M. M., Rahman, M., and Khan, J., 2013. Computational studies on the flow field of various shapes-bladed vertical axis Savonius turbine in static condition. Paper No. IMECE2013-65081, ASME International Mechanical Engineering Congress and Exposition, November 5-9, San Diego, CA, USA

Kianifar, A., Anbarsooz, M., and Javadi, M., 2010. Blade curve influences on performance of Savonius rotors: Experimental and numerical, Paper No. FEDSM-ICNMM2010-30919, ASME 3rd Joint US-European Fluids Engineering Summer Meeting, August 1-5, Montreal, Canada.

Kline, S. J., 1985. The purposes of uncertainty analysis. ASME Journal of Fluids Engineering, 107(2), pp. 153-160.

Le, T-Q, Lee, K-S., Park, J-S., and Ko, J-H. 2014. Flow-driven rotor simulation of vertical axis tidal turbines: A comparison of helical and straight blades, International Journal of Naval Architecture and Ocean Engineering, 6:257-268.

Lee, S., 1997. Unsteady aerodynamic force prediction on a square cylinder using k-ε turbulence models. Journal of Wind Engineering & Industrial Aerodynamics, 68, pp. 79– 90.

Menet, J. L., 2004. A double-step Savonius rotor for local production of electricity: A design study. Renewable Energy, 29, pp. 1843–1862.

Menter, F. R., 1994. Two-equation eddy-viscosity turbulence models for engineering applications, AIAA Journal, Vol. 32, No. 8, pp. 1598–1605.

Modi, V., and Fernando, M., 1989. On the performance of the Savonius wind turbine. Journal of Wind Engineering & Industrial Aerodynamics, 111, pp. 71–81.

Modi, V. J., and Fernando, M. S. U. K., 1993. Unsteady aerodynamics and wake of the Savonius wind turbine: A numerical study. Journal of Wind Engineering & Industrial Aerodynamics, 46–47, pp. 811–816.

Modi, V. J., Roth, N. J., and Fernando, M. S. U. K., 1984. Optimum-configuration studies and prototype design of a wind-energy-operated irrigation system. Journal of Wind Engineering & Industrial Aerodynamics, 16, pp. 85–96.

Mohamed, M. H., Janiga, G., Pap, E., and Thévenin, D., 2011. Optimal blade shape of a modified Savonius turbine using an obstacle shielding the returning blade. Energy Conversion and Management, 52, pp. 236–242.

Mohamed, M. H., Janiga, G., Pap, E., and Thévenin, D., 2010. Optimization of Savonius turbines using an obstacle shielding the returning blade. Renewable Energy, 35, 2618-2626.

Manwell, J. F., Mcgowan, J. G., and Rogers, A. L., 2009. Wind energy explained: Theory, design and application. UK: John Wiley & Sons Limited.

Mari, M., Venturini, M., and Beyene, A., 2017. A novel geometry for vertical axis wind turbines based on the Savonius concept. ASME Journal of Energy Resources Technology, 139(6), pp. 1–9.

Mojola, O. O., 1985. On the aerodynamic design of the Savonius windmill rotor. Journal of Wind Engineering & Industrial Aerodynamics, 21, pp. 223–231.

Mohammadi, M., Lakestani, M., and Mohamed, M. H., 2018. Intelligent parameter optimization of Savonius rotor using Artificial Neural Network and Genetic Algorithm. Energy, 143, pp. 56-68.

Moffat, R. J., 1982. Contributions to the theory of single-sample uncertainty analysis. ASME Journal of Fluids Engineering, 104, pp. 250-258.

Morcos, S. M., Khalafallah, M. G., and Heikel, H. A., 1981. The effect of shielding on the aerodynamic performance of Savonius wind turbines. in: Proceedings of the 16th Intersoc. Energy Convers. Eng. Conf., Atlanta, GA, August 9-14, 2037-2040.

Müller, G., Jentsch, M. F., and Stoddart, E., 2009. Vertical axis resistance type wind turbines for use in buildings. Renewable Energy, 34(5), pp. 1407–1412.

Nasef, M. H., El-Askary, W. A., AbdEL-hamid, A. A., and Gad, H. E., 2013. Evaluation of Savonius rotor performance: Static and dynamic studies. Journal of Wind Engineering & Industrial Aerodynamics, 123, pp. 1–11.

Newman, 1974. Measurements on Savonius rotor with variable gap. in Proceeding of Sherbrook University Symposium on Wind Energy, Sherbrook Canada.

Neto, J. X. V., Junior, E. J. G., Moreno, S. R., Ayala, H. V. H., Mariani, V. C., and Coelho, L. S., 2018. Wind turbine blade geometry design based on multi-objective optimization using metaheuristics. Energy, 162, pp. 645-658.

Ogawa, T., 1984. Theoretical study on the flow about Savonius rotor. ASME Journal of Fluids Engineering, 106, pp. 85–91.

Ogawa, T., Yoshida, H., and Yokota, Y., 1989. Development of rotational speed control systems for a Savonius-type wind turbine. ASME Journal of Fluids Engineering, 111, pp. 53-58.

Plourde, B., Abraham, J., Mowry, G., and Minkowycz, W., 2012. Simulations of three dimensional vertical-axis turbines for communications applications. Wind Engineering, 36, pp. 443–454.

Prabhukhot, P. R., and Prabhukhot, A. R., 2017. Computer analysis of S822 aerofoil section for blades of small wind turbines at low wind speed. ASME Journal of Solar Energy Engineering, Vol. 139 (5), p. 051008-1.

Rahai, H., and Hefazi, H., 2005. Development of optimum design configuration and performance for vertical axis wind turbine. Feasibility Analysis and Final EISG Report (California Energy Commission).

Rathod U. H., Kulkarni V., Saha U. K., 2023. Evolving a bio-inspired blade shape of the drag-based vertical-axis wind rotor derived from orange sea-pen (*Ptilosarcus Gurneyi*). ASME Journal of Solar Energy Engineering, 145(3), pp. 031007.

Rathod, U.H., Kulkarni, V. and Saha, U.K., 2022. On the application of machine learning in savonius wind turbine technology: an estimation of turbine performance using artificial neural network and genetic expression programming. Journal of Energy Resources Technology, *144*(6), p.061301.

Rajkumar, M. J., and Saha, U. K., 2006. Valve-aided twisted Savonius rotor. Wind Engineering, 30, pp. 243–254.

Rajkumar, M. J., 2004. Experimental investigation and flow simulation of Savonius rotor. M. Tech. Thesis, Department of Mechanical Engineering, IIT Guwahati, India.

Raimi, D., Zhu, Y., Newell, R.G. and Prest, B.C., 2024. Global energy outlook 2024: Peaks or Plateaus.

Ramadan, A., Yousef, K., Said, M., and Mohamed, M. H., 2018. Shape optimization and experimental validation of a drag vertical axis wind turbine. Energy,151, pp. 839-853.

Reupke, P., and Probert, S. D., 1991. Slatted-blade Savonius wind-rotors. Applied Energy, 40, pp. 65–75.

Ricci, R., Romagnoli, R., Montelpare, S., and Vitali, D., 2016. Experimental study on a Savonius wind rotor for street lighting systems. Applied Energy, 161, pp. 143–152.

Roy, S., and Ducoin, A., 2016. Unsteady analysis on the instantaneous forces and moment arms acting on a novel Savonius-style wind turbine. Energy Conversion Management, 121, pp. 281–296.

Roy, S., 2014. Aerodynamic performance evaluation of a novel Savonius-style wind turbine through unsteady simulations and wind tunnel experiments. PhD thesis, Department of Mechanical Engineering, IIT Guwahati, India

Roy, S., Mukherjee, P., and Saha, U. K., 2014. Aerodynamic performance evaluation of novel Savonius-style wind turbine under oriented jet. Paper No. GTINDIA2014-8152, ASME 2014 Gas Turbine India Conference, December 15-17, New Delhi, India.

Roy, S., and Saha, U. K., 2015. Wind tunnel experiments of a newly developed two-bladed Savonius-style wind turbine. Applied Energy, 137, pp. 117–125.

Roy, S., and Saha, U. K., 2014. An adapted blockage factor correlation approach in wind tunnel experiments of a Savonius-style wind turbine. Energy Conversion Management, 86, pp. 418–427.

Roy, S., and Saha, U. K., 2013. Review of experimental investigations into the design, performance and optimization of the Savonius rotor. Proc. Inst. Mech. Eng. Part A Journal of Power and Energy, 227, pp. 528–542.

Roy, S., and Saha, U. K., 2013. Computational study to assess the influence of overlap ratio on static torque characteristics of a vertical axis wind turbine. Procedia Engineering, 51, pp. 694–702.

Roy, S., and Saha, U. K., 2013. Investigation on the effect of aspect ratio into the performance of Savonius rotor. Paper No. GTINDIA2013-3729, ASME Gas Turbine India Conference, December 5-6, Bangalore, India.

Roy, S., and Saha, U. K., 2013. Numerical investigation to assess an optimal blade profile for the drag based vertical axis wind turbine. Paper No. IMECE2013-64001, ASME International Mechanical Engineering Congress & Exposition, November 15-21, 2013, San Diego, CA, USA.

Ross, I., and Altman, A., 2011. Wind tunnel blockage corrections: Review and application to Savonius vertical-axis wind turbines. Journal of Wind Engineering & Industrial Aerodynamics, 99(5), pp. 523–538.

Sargolzaei, J., and Kianifar, A., 2010. Neuro–fuzzy modeling tools for estimation of torque in Savonius rotor wind turbine. Advances in Engineering Software, 41, pp. 619–626.

Saha, U. K., and Rajkumar, M. J., 2006. On the performance analysis of Savonius rotor with twisted blades. Renewable Energy, 31, pp. 1776–1788.

Saha, U. K., Thotla, S., and Maity, D., 2008. Optimum design configuration of Savonius rotor through wind tunnel experiments. Journal of Wind Engineering & Industrial Aerodynamics, 96, pp. 1359–1375.

Savonius, S. J., 1930. The S-rotor and its applications. Mechanical Engineering 1931;53(5):333-38

Sharma, S., and Sharma, R. K., 2017. CFD investigation to quantify the effect of layered multiple miniature blades on the performance of Savonius rotor. Energy Conversion and Management, 144, pp. 275–285.

Sharma, S., and Sharma, R. K., 2016. Performance improvement of Savonius rotor using multiple quarter blades - A CFD investigation. Energy Conversion and Management, 127, pp. 43–54.

Shaughnessy, B. M., and Probert, S. D., 1992. Partially-blocked Savonius rotor. Applied Energy, 43, pp. 239–249.

Sheldahl, R. E., Feltz, L. V., and Blackwell, B. F., 1978. Wind tunnel performance data for twoand three-bucket Savonius rotors. Energy, 2, pp. 160–164.

Shikha, Bhatti, T. S., and Kothari, D. P., 2003. Wind energy conversion systems as a distributed source of generation. ASCE Journal of Energy Engineering. 129, pp. 69–80.

Shahzad, A., Asim, T., Mishra, R., and Paris, A., 2013. Performance of a Vertical Axis Wind Turbine under Accelerating and Decelerating Flows, Procedia CIRP, 11, pp. 311 – 316.

Singh, R. K., and Ahmed, M. R., 2013. Blade design and performance testing of a small wind turbine rotor for low wind speed applications. Renewable Energy, 50, pp. 812-819.

Song, C., Zheng, Y., Zhao, Z., Zhang, Y., Li, C., and Jiang, H., 2015. Investigation of meshing strategies and turbulence models of computational fluid dynamics simulations of vertical axis wind turbines. Journal of Renewable and Sustainable Energy, 7, pp. 0–19.

Song, L., Yang, Z.-X., Deng, R.-T., and Yang, X.-G., 2013. Performance and structure optimization for a new type of vertical axis wind turbine, in: Proceedings of the IEEE2013 International Conference on Advanced Mechatronic Systems. pp. 687–692.

Simonds, M. H., and Bodek, A., 1964. Performance test of a Savonius rotor (Brace Research Institute. McGill University, Quebec, Canada.

Sahim, K., Santoso, D., and Radentan, A., 2013. Performance of combined water turbine with semi elliptic section of the Savonius rotor. Hindawi Publishing Corporation International Journal of Rotating Machinery Volume 2013, Article ID 985943, 5 pages

Sivasegaram, S., and Sivapalan, S., 1983. Augmentation of power in slow-running verticalaxis wind rotors using multiple vanes. Wind Engineering, Vol. 7, No. 1, pp. 12–19.

Talukdar, P.K., Alom, N., Rathod, U.H. and Kulkarni, V., 2022. Alternative blade profile based on Savonius concept for effective wind energy harvesting. *ASME Journal of Energy Resources Technology*, *144*(4), p.041304.

Tartuferi, M., Alessandro, V. D., Montelpare, S., and Ricci, R., 2015. Enhancement of Savonius wind rotor aerodynamic performance: a computational study of new blade shapes and curtain systems. Energy, 79, pp. 371–384.

Tian, W., Mao, Z., An, X., Zhang, B., and Wen, H., 2017. Numerical study of energy recovery from the wakes of moving vehicles on highways by using a vertical axis wind turbine. Energy, 141, pp. 715–728.

Thotla, S., 2006. Optimum design configuration of Savonius rotor through wind tunnel testing. M. Tech. Thesis, Department of Mechanical Engineering, IIT Guwahati, India.

Ushiyama, I., Nagai, H., and Mino, M., 1982. The optimum design configurations of Savonius wind turbines. In: Proceedings of the 17th intersociety energy conversion engineering conference (IECEC ‘82), Los Angeles, California, August 8–12, Vol. 4, pp. 2096–2101.

Ushiyama, I., and Nagai, H., 1988. Optimum design configurations and performance of Savonius rotors. Wind Engineering, 12(1), pp. 59–75.

White, F. M., 2011. Fluid mechanics. New York, USA: McGraw-Hills. WWEA 2019. World wind energy association.

Wong, K. H., Chong, W. T., Sukiman, N. L., Poh, S. C., Shiah, Y-C., and Wang, C-T., 2017. Performance enhancements on vertical axis wind turbines using flow augmentation systems: A review. Renewable and Sustainable Energy Reviews, 73, pp. 904–21.

Xu, G and Sankar, L. N., 2000. Computational study of horizontal axis wind turbines. ASME Journal of Solar Energy Engineering, 122, pp. 35-39.

Zhao, Z., Zheng, Y., Xu, X., Liu, W., and Hu, G., 2009. Research on the Improvement of the Performance of Savonius Rotor Based on Numerical Study. in: Proceedings of the International Conference on Sustainable Power Generation and supply. pp. 1–6.

Zhang, B., Song, B., Mao, Z., and Tian, W., 2017. A novel wake energy reuse method to optimize the layout for Savonius-type vertical axis wind turbines. Energy, 121, pp. 341–355.

Zhou, T., and Rempfer, D., 2013. Numerical study of detailed flow field and performance of Savonius wind turbines. Renewable Energy, 51, pp. 373–381.

Zhou, Q., Xu, Z., Cheng, S., Huang, Y., and Xiao, J., 2018. Innovative Savonius rotors evolved by genetic algorithm based on 2D-DCT encoding. Soft Computing.

Appendix

The transient simulations in this study are conducted using ANSYS Fluent, a solver based on *FVM*. The mathematical formulation of these equations is provided in the following equations (A.1-A.10):

Continuity equation

$$\frac{\partial \rho}{\partial t} + \frac{\partial(\rho u)}{\partial x} + \frac{\partial(\rho v)}{\partial y} = 0 \tag{A.1}$$

Momentum equations

$$\rho\frac{Du}{Dt} = \rho g - \frac{\partial p}{\partial x} + \mu\left(\frac{\partial^2 u}{\partial x^2} + \frac{\partial^2 u}{\partial y^2}\right) \tag{A.2}$$

$$\rho\frac{Dv}{Dt} = \rho g - \frac{\partial p}{\partial y} + \mu\left(\frac{\partial^2 v}{\partial x^2} + \frac{\partial^2 v}{\partial y^2}\right) \tag{A.3}$$

Considering that the flow around the rotor is fully turbulent and thereby invoking the Reynolds decomposition, the aforementioned equations become

$$\frac{\partial \bar{u}}{\partial x} + \frac{\partial \bar{v}}{\partial y} = 0 \tag{A.4}$$

$$\rho\left(\frac{\partial \bar{u}}{\partial t} + \bar{u}\frac{\partial \bar{u}}{\partial x} + \bar{v}\frac{\partial \bar{u}}{\partial y}\right) = \rho g - \frac{\partial \bar{p}}{\partial x} + \mu\Delta\bar{u} - \rho\left(\frac{\partial \overline{u'u'}}{\partial x} + \frac{\partial \overline{u'v'}}{\partial y}\right) \tag{A.5}$$

$$\rho\left(\frac{\partial \bar{v}}{\partial t} + \bar{u}\frac{\partial \bar{v}}{\partial x} + \bar{v}\frac{\partial \bar{v}}{\partial y}\right) = \rho g - \frac{\partial \bar{p}}{\partial y} + \mu\Delta\bar{v} - \rho\left(\frac{\partial \overline{u'v'}}{\partial x} + \frac{\partial \overline{v'v'}}{\partial y}\right) \tag{A.6}$$

To calculate the turbulent viscosity terms in the *RANS* equations, the shear stress transport (SST) *k-ω* turbulence model is employed. The SST *k-ω* turbulence model combines the strengths of the *k-ε* model for free stream flows, and the *k-ω* model for boundary layer flows, ensuring accurate prediction of flow separation with adverse pressure gradients. The transport equations for turbulent kinetic energy '*k*' and specific dissipation rate '*ω*' are used to obtain their values in eqns.3.11 and 3.12:

$$\rho\left(\frac{\partial(k)}{\partial t}+\frac{\partial(k u_i)}{\partial x_i}\right)=\frac{\partial}{\partial x_j}\left(\Gamma_k\frac{\partial k}{\partial x_j}\right)+\tilde{G}_k-Y_k+S_k \tag{A.7}$$

$$\rho\left(\frac{\partial(\omega)}{\partial t}+\frac{\partial(\omega u_i)}{\partial x_i}\right)=\frac{\partial}{\partial x_j}\left(\Gamma_\omega\frac{\partial \omega}{\partial x_j}\right)+\tilde{G}_\omega-Y_\omega+S_\omega \tag{A.8}$$

In these equations, $\tilde{G}_k$ denotes the generation of turbulence kinetic energy due to mean velocity gradients. $\tilde{G}_\omega$ denotes the generation of ω. Γ_k and Γ_ω indicate the effective diffusivity of k and ω, respectively. S_ω denotes the dissipation of k due to turbulence that is user-defined source terms. The effective diffusivities for the k-ω model are determined by eqns. 3.13 and 3.14:

$$\Gamma_k = \mu + \frac{\mu_t}{\sigma_k} \tag{A.9}$$

$$\Gamma_\omega = \mu + \frac{\mu_t}{\sigma_\omega} \tag{A.10}$$

where, σ_k and σ_ω are the turbulent Prandtl numbers for k and ω respectively. μ_t is the turbulent viscosity.

Publications

Journals

1. Mohan, M. and Saha, U.K., 2024. Wind tunnel tests of a two-bladed Savonius wind rotor with novel parabolic blades. *Wind Engineering*, p.0309524X241239983.

2. Mohan M, Talukdar P.K., and Saha U.K, 2024. Influence of Reynolds number on aerodynamic and power coefficients of a novel parabolic-bladed Savonius wind rotor. *ASME Journal of Energy Resources Technology.* Vol. 146, Issue 11, p. 111801 (11 pages).

3. Mohan M, and Saha U.K., 2024. Evolving a novel blade shape of a Savonius wind rotor using an optimization technique coupled with numerical simulations and wind tunnel tests. *ASME Journal of Energy Resources Technology*, Vol. 146, Issue 4, p. 041301 (11 pages).

4. Mohan M, Alom, N, and Saha U.K., 2023. Role of optimization and soft-computing techniques in the design and development of futuristic Savonius wind turbine blades: A review. *Wind Engineering,* Vol. 47, Issue 3, pp. 722 – 744.

5. Mohan M, and Saha U.K., 2023. Computational study of a newly developed parabolic blade profile of a Savonius wind rotor. *Journal of the Brazilian Society of Mechanical Sciences and Engineering*, Vo. 45, Article No. 548 (12 pages).

Conferences

6. Mohan, M., Sharma, D., and Saha, U.K., 2023. Optimization strategies on the aerodynamic design of a Savonius wind rotor blade profile. Paper no. 143, 6th *National Conference on Multidisciplinary Design, Analysis and Optimization* (NCMDAO 2023), December 6 – 8, IIT Guwahati, India.

7. Mohan M, Kansagara DD, Sharma D, and Saha U.K., 2021. Estimating the aerodynamic coefficients of a Savonius rotor blade profile developed through simplex search method. Paper No. GTIndia2021-75990, *ASME 2021 Gas Turbine India Conference*, December 02 – 03, 2021 (Virtual Conference, Online).

8. Mohan M, and Saha U.K., 2021. Overlap ratio as the design variable for maximizing the efficiency of a Savonius wind rotor: An optimization approach. Paper No. IMECE2021-69930, *ASME 2021 International Mechanical Engineering Congress and Exposition*, November 01 – 04, 2021 (Virtual Conference, Online).